

## INFORMATION TO USERS

This manuscript has been reproduced from the microfilm master. UMI films the text directly from the original or copy submitted. Thus, some thesis and dissertation copies are in typewriter face, while others may be from any type of computer printer.

**The quality of this reproduction is dependent upon the quality of the copy submitted.** Broken or indistinct print, colored or poor quality illustrations and photographs, print bleedthrough, substandard margins, and improper alignment can adversely affect reproduction.

In the unlikely event that the author did not send UMI a complete manuscript and there are missing pages, these will be noted. Also, if unauthorized copyright material had to be removed, a note will indicate the deletion.

Oversize materials (e.g., maps, drawings, charts) are reproduced by sectioning the original, beginning at the upper left-hand corner and continuing from left to right in equal sections with small overlaps.

ProQuest Information and Learning  
300 North Zeeb Road, Ann Arbor, MI 48106-1346 USA  
800-521-0600

**UMI**<sup>®</sup>



University of Alberta

Improving photon energy fluence measurement with an a-Si EPID

By

Charles James Kirkby



A thesis submitted to the Faculty of Graduate Studies and Research in partial  
fulfilment of the requirements for the degree of Doctor of Philosophy

in

Medical Physics

Department of Physics

Edmonton, Alberta  
Fall, 2005



Library and  
Archives Canada

Bibliothèque et  
Archives Canada

Published Heritage  
Branch

Direction du  
Patrimoine de l'édition

0-494-08666-1

395 Wellington Street  
Ottawa ON K1A 0N4  
Canada

395, rue Wellington  
Ottawa ON K1A 0N4  
Canada

*Your file* *Votre référence*

*ISBN:*

*Our file* *Notre référence*

*ISBN:*

**NOTICE:**

The author has granted a non-exclusive license allowing Library and Archives Canada to reproduce, publish, archive, preserve, conserve, communicate to the public by telecommunication or on the Internet, loan, distribute and sell theses worldwide, for commercial or non-commercial purposes, in microform, paper, electronic and/or any other formats.

The author retains copyright ownership and moral rights in this thesis. Neither the thesis nor substantial extracts from it may be printed or otherwise reproduced without the author's permission.

**AVIS:**

L'auteur a accordé une licence non exclusive permettant à la Bibliothèque et Archives Canada de reproduire, publier, archiver, sauvegarder, conserver, transmettre au public par télécommunication ou par l'Internet, prêter, distribuer et vendre des thèses partout dans le monde, à des fins commerciales ou autres, sur support microforme, papier, électronique et/ou autres formats.

L'auteur conserve la propriété du droit d'auteur et des droits moraux qui protègent cette thèse. Ni la thèse ni des extraits substantiels de celle-ci ne doivent être imprimés ou autrement reproduits sans son autorisation.

---

In compliance with the Canadian Privacy Act some supporting forms may have been removed from this thesis.

Conformément à la loi canadienne sur la protection de la vie privée, quelques formulaires secondaires ont été enlevés de cette thèse.

While these forms may be included in the document page count, their removal does not represent any loss of content from the thesis.

Bien que ces formulaires aient inclus dans la pagination, il n'y aura aucun contenu manquant.

Canada

*To my wife, Fiona*

## Abstract

The present work comprises a study of the physics that underlies the image formation process of a commercial a-Si EPID, the Varian aS500, with particular emphasis on its adaptation for two-dimensional megavoltage dosimetry. Specifically, the work focuses on blur kernel elucidation and dosimetric calibration.

A comprehensive model of the aS500 was developed for Monte Carlo simulations, allowing detector-specific response data to be calculated for direct comparison with corresponding experimental results. Additional, unrelated Monte Carlo work that led to the development of single event spectra for five therapeutic radionuclides is also described.

In this work, we present a comprehensive blur kernel for the aS500 EPID. Monte Carlo techniques were used to derive a dose kernel and an optical kernel, which were combined into an overall blur kernel for 6 and 15 MV photon beams. Experimental measurements of the line spread function verified the kernel shape. Kernel performance was gauged by comparing EPID image profiles (pre- and post-deconvolution) with in-air profiles measured with a diamond detector. Quantitative comparisons demonstrate the relative importance of the optical kernel. Empirical and semi-empirical kernels are shown to closely approach the performance of the comprehensive kernel. A follow-up investigation developed a diamond detector blur kernel and showed that deconvolution of the volume averaging effects for this detector had little influence on results, except for very small fields.

This work also investigated dose calibration curve variability with beam quality for the aS500 EPID. An over-response of the aS500 to low energy ( $< 1$  MeV) photons was found to be the main cause of this variability. When a 6 MV beam is hardened by steel shot attenuators, the EPID response can be as much as 8% lower than that for an open field. A Monte Carlo study suggested that this difference is due to spectral effects, and that it could be reduced by the addition of an external copper plate. Experimental results confirm that a copper plate  $\sim 0.7$  cm thick placed 15 cm above the EPID can reduce calibration curve differences to  $< 4\%$ , but at the expense of reduced contrast-to-noise ratio and modulation transfer.

## Acknowledgements

I would like to take this opportunity to thank all those who played a part in the work that led to the completion of this thesis. The amount of support that I have received over the years this work took to accomplish has been nothing short of outstanding.

In particular I would like to thank Dr. Ron Sloboda. He has been a model supervisor and mentor. His guidance, advice, and support have been invaluable over the course of this work and through my graduate career. I consider it a privilege to have been his student.

I would also like to give particular thanks to the members of my supervisory committee, Dr. B. Gino Fallone and Dr. Don Robinson. Dr. Fallone has been the driving force behind the medical physics graduate program which has offered me and many others the opportunity to study this field at a world class institution. He and Dr. Robinson have provided a great deal of valuable insight and guidance into the work contained in this thesis.

In addition, I would like to thank the other members of my examination committee, Dr. Richard Sydora, and Dr. Rufus Scrimger, and my external reviewer, Dr. Jeffrey Siebers. Dr. Siebers' review of this thesis made it a much stronger body of scientific work.

All of the staff and students at the Cross Cancer Institute deserve thanks as well for their support. I can't possibly thank everyone by name, but there are several people in particular who deserve special mention. I would like to thank Dr. Brad Warkentin and Dr. Stephen Steciw for the many long discussions on this work as well as for their continuing friendship. I thank Dr. Alasdair Syme, in particular for his efforts with the microdosimetry aspects of this work. I would also like to thank Dr. Satyapal Rathee for his advice and assistance. I also thank the gentlemen in the machine shop, Gary Morrison and Ken Henning for their assistance with the copper plates and mould room staff for their assistance with the compensators. I would also like to thank Varian Medical Systems, for the assistance and information they have provided with respect to the aS500 EPID. I cannot forget to mention my friends – those who have shared lunches and cubicles with me over the years, worked through all the different graduate courses, and provided a welcoming and fun environment in which to conduct this research. This includes my friends outside of the medical physics program as well, Jeff de Jong, the people of the University of Alberta's Campus Security Services, the Feynman Football team, and many others.

Finally I would like to thank my family. I can't begin to mention the sacrifices they have made to assist me with this work. I thank my wife Fiona, who has been in my corner the whole time, supporting me, and loving me. It is to her that I dedicate this work. And I close by thanking my parents who have offered nothing but encouragement from day one.



# Table of Contents

<b>CHAPTER 1: INTRODUCTION</b>	<b>1</b>
1.1 OVERVIEW	1
1.2 RADIATION THERAPY AND CANCER	1
1.3 PORTAL IMAGING AND DOSIMETRY IN RADIOTHERAPY	5
1.4 ELECTRONIC PORTAL IMAGING DEVICES	7
1.5 THE MONTE CARLO METHOD	10
1.6 OVERVIEW OF THE THESIS	13
1.7 REFERENCES	18
<b>CHAPTER 2: THE VARIAN aS500 EPID</b>	<b>22</b>
2.1 INTRODUCTION	22
2.2 DESCRIPTION OF THE VARIAN aS500 EPID	22
2.2.1 Overview of the EPID	22
2.2.2 EPID Primary Components	24
2.2.3 Image Acquisition	26
2.2.4 Image Calibration	28
2.3 COMPREHENSIVE MODEL OF THE EPID	29
2.3.1 Assumptions in the Radiation Transport Model	30
2.3.2 The Optical Model	32
2.4 SUMMARY	33
2.5 REFERENCES	40
<b>CHAPTER 3: MONTE CARLO METHOD AND SIMULATION CODES</b>	<b>42</b>
3.1 INTRODUCTION TO THE MONTE CARLO METHOD	42
3.2 OVERVIEW AND BENCHMARKING OF EGSNRC	44
3.2.1 Introduction to EGSnrc	44
3.2.2 Benchmarking	48
3.3 SINGLE CELL BETA DOSIMETRY	52
3.3.1 Introduction	52
3.3.2 Monte Carlo Simulations	53
3.3.3 Results and Discussion	57
3.4 OVERVIEW OF DETECT2000	59
3.4.1 Introduction to DETECT2000	59
3.4.2 Benchmarking DETECT2000	61
3.5 SUMMARY	63
3.6 REFERENCES	72

<b>CHAPTER 4: COMPREHENSIVE MONTE CARLO CALCULATION OF THE POINT SPREAD FUNCTION FOR A COMMERCIAL a-Si EPID</b>	<b>75</b>
4.1 INTRODUCTION	75
4.2 THEORY AND METHODS	77
4.2.1 Point Spread Function	77
4.2.2 EGSnrc Simulations	78
4.2.3 DETECT2000 Simulations	80
4.2.2 Combining the Kernels	81
4.2.5 Experimental Measurement of the Line Spread Function	82
4.2.6 Other PSF's	84
4.2.7 Fluence Recovery	86
4.2.8 Kernel Performance Evaluation	88
4.2.9 Diamond Detector Response Function and Fluence Recovery	90
4.3 RESULTS AND DISCUSSION	92
4.3.1 Dose Deposition Kernel	92
4.3.1.1 Depth Dose in Scintillation Screen	92
4.3.1.2 Pencil Beam Response in Scintillation Screen	93
4.3.2 Optical Spreading Kernel	93
4.3.3 Overall Blur Kernel	94
4.3.4 Comparison with Experimental LSF	95
4.3.5 Energy Fluence Recovery	96
4.3.6 Other PSF's	99
4.3.7 Diamond Detector Response Function and Fluence Recovery	100
4.4 SUMMARY AND CONCLUSIONS	102
4.5 REFERENCES	128

<b>CHAPTER 5: CONSEQUENCES OF THE SPECTRAL RESPONSE OF AN a-Si EPID AND IMPLICATIONS FOR DOSIMETRIC CALIBRATIONS</b>	<b>131</b>
5.1 INTRODUCTION	131
5.2 METHODS	133
5.2.1 Monte Carlo Investigations	133
5.2.1.1 Energy Spectrum Variation	134
5.2.1.2 EPID Energy Response	135
5.2.1.3 Simulated Calibration Curve	136
5.2.2 Experimental Measurements	137
5.2.2.1 EPID and Ion Chamber Measurements	138
5.2.2.2 Beam and Detector Configurations	139
5.2.2.3 Imaging Performance	141
5.2.3 Calibration Curve Differences	142
5.3 RESULTS	143
5.3.1 Monte Carlo Investigations	143
5.3.1.1 Energy Spectrum Variation	143
5.3.1.2 EPID Energy Response	144
5.3.1.3 Simulated Calibration Curve	146

5.3.2	Experimental Measurements	148
5.3.2.1	Calibration Curve	148
5.3.2.2	Imaging Performance	150
5.4	DISCUSSION	151
5.5	CONCLUSION	155
5.6	REFERENCES	172
<b>CHAPTER 6: SUMMARY AND FUTURE DIRECTIONS</b>		<b>174</b>
6.1	SUMMARY	174
6.2	FUTURE DIRECTIONS	176
6.3	REFERENCES	179

## List of Tables

Table 2.1	The relative weights of the elements used in the FR4 model mixture.	34
Table 2.2	The parameters used in DETECT2000 to model the optical photon transport. Kodak <sup>17</sup> provided a scatter MFP between 10 and 25 $\mu\text{m}$ and an absorption MFP of greater than 10 cm. For comparison, Kausch et al. <sup>12</sup> used a scatter MFP of 25 $\mu\text{m}$ , an absorption MFP of 4 cm, and an index of refraction of 2.4 in a different transport code, and did not model the optical filter.	34
Table 3.1	A summary of Monte Carlo thin foil dose estimates for a 1 MeV incident photon beam compared to corresponding analytical predictions, for a variety of materials and foil thicknesses. In general, discrepancies are 1% or less where the assumptions inherent in the analytical method are strongest.	65
Table 3.2	Values of $\langle z_f \rangle$ calculated for a sphere of radius 5 $\mu\text{m}$ using the Monte Carlo codes EGSnrc, OREC, and PENELOPE. Agreement between EGSnrc and OREC is very good at 1 MeV, but shows a 7.4 % discrepancy at 0.1 MeV. PENELOPE also shows reasonably good agreement with EGSnrc.	65
Table 3.3	The number of optical photons passing three scoring planes for a simple benchmarking problem (Fig 3.5) detected by DETECT2000, compared to the analytical expression of Eq. 3.16. $10^6$ photons were simulated. Predictably, the relative difference between the Monte Carlo results and the theory increases as the number of particles detected decreases.	66
Table 4.1	Parameter values determined empirically for the triple exponential form of the PSF.	105
Table 4.2	A summary of the percentage of $\chi$ scores $< 1.0$ (in last two columns) corresponding to the different kernels and parameters investigated in this work. The acceptance criteria were defined as a distance to agreement of 0.0784 cm and a dose difference of 2% of the central axis value. Values marked with an asterisk used a smaller dose difference of 1%.	105
Table 5.1	The relative difference (expressed as a percentage of the 1.125 MeV energy bin value) between the EPID energy response and the IIC energy response for the energy bins $< 1$ MeV. The differences decrease with increasing Cu plate thickness and are smaller with the Cu plate in the elevated configuration compared to the contact configuration.	157
Table 5.2	The $f_{50}$ values reported by the PIPSPRO software package. The values as calculated appear to be reasonably constant with increasing Cu thickness.	157

## List of Figures

Figure 1.1	A schematic illustration of the various planes of interest in portal dosimetry.	16
Figure 1.2	The time to solution for the Monte Carlo method as compared to analytic or deterministic approaches. As the complexity of the problem increases, Monte Carlo offers a more efficient means to solve a given problem.	17
Figure 2.1	A cross section view of the aS500 EPID (not to scale). This view shows the relative locations of the various components of the detector. The image detection stack in the center consists of the materials indicated as well as numerous support structures (such as foam, epoxy, and paper.) The additional buildup material shown is typically solid water, and is added to the detector to enhance buildup for dosimetry applications.	35
Figure 2.2	A schematic diagram of a typical pixel and how it is connected to the readout electronics. Optical photons absorbed by the amorphous silicon move electrons into the conduction band, from where an externally applied reverse bias voltage causes the charges to migrate towards the n- and p-doped layers above and below, effectively making the device behave like a capacitor. <sup>7</sup> During periods of no irradiation the gate drivers open up the TFTs on a row by row basis allowing the external charge preamplifiers to collect the charge. An image frame consists of a readout of all rows.	36
Figure 2.3	A sample dark field image. Approximately 60 frames were acquired with the beam off. This image reflects non-uniformities in the detector array (due to the manufacturing process and possible damage) and variations in electrometer offsets.	37
Figure 2.4	A sample flood field image. Approximately 30 frames were acquired with the EPID deployed at 140 cm SDD [6 MV, 300 MU/min, IMRT scan mode]. The image reflects radiation field inhomogeneity, individual pixel sensitivities and electrometer gains.	38
Figure 2.5	A sample image of a $10 \times 10 \text{ cm}^2$ field (defined at the imaging plane) with the EPID deployed at 140 cm SDD [6 MV, 300 MU/min, IMRT scan mode]. The correction scheme defined by Eq. 2.1 has been applied.	39
Figure 3.1	The geometries used in the single cell beta dosimetry investigation. In the first geometry a beta-emitting radionuclide is part of an antibody that binds to the surface of a spherical cell. In the second geometry we consider the case of a cell immersed in a bath of radioactivity. Sample electron tracks are shown for each case.	67

Figure 3.2	Beta emission spectra (a) and CSDA spectra (b) for the radionuclides used in this study. $I(T)$ denotes the relative intensity of beta emissions of kinetic energy $T$ . $C(T)$ denotes the relative intensity of electrons with energy $T$ at any point in the medium. The spectra have not been normalised.	68
Figure 3.3	Single event spectra for low energy electrons in the surface bound (a) and in the free radioactivity (b) geometries. Below 50 keV the spectra show a peak at a value of $z$ corresponding to the initial energy of the electrons. The low energy spectra change rapidly with energy.	69
Figure 3.4	Single event spectra for high energy electrons in the surface bound (a) and free radioactivity (b) geometries. The spectra change more slowly at these energies. The free radioactivity geometry results show a shift towards higher $z$ values relative to the corresponding surface bound case due to larger mean path lengths through the target.	70
Figure 3.5	A point source of optical photons inside a $40 \times 40 \times 40 \text{ cm}^3$ cube. The dominant interaction in the medium is absorption. Photons are scored as they cross a plane at a distance $z$ above the source.	71
Figure 4.1	The principal components of the EPID detector stack. Additional supporting structures and substrate materials such as glass, foam, paper and fiberglass are also present. The pencil beam is incident on the top surface of the buildup layer. The phosphor is divided into 10 equal layers defined by discrete values of $z$ .	106
Figure 4.2	Geometry considered for the optical component of signal spreading. Optical photons are produced with an isotropic distribution in the scintillation screen (s) at point $P(x',y',z)$ , and travel through the screen and through the optical filter (f) until they strike the photodiode surface (d) at a point $P_d(x,y,d_d)$ . Two possible optical photon paths are illustrated.	107
Figure 4.3	The apparatus used to measure the LSF. A $2 \times 5 \text{ cm}^2$ field is projected onto a $380 \text{ }\mu\text{m}$ slit to form the slit image at an angle of $1.7^\circ$ (a). Subsequently the lead blocks are laterally translated $\sim 2 \text{ cm}$ on the translation stage such that the field does not pass directly through the slit to form an offset image (b).	108
Figure 4.4	Relative dose deposited along the CAX in the EPID scintillation screen. The dose deposited in a $0.0784 \text{ cm}$ diameter radial bin for each of the ten layers is normalized to the layer having maximum dose. The figure illustrates the presence of dose buildup and fall-off within the screen in response to an incident pencil beam of photon radiation.	109

Figure 4.5	The relative dose in the full thickness of phosphor as a function of near radial distance (0-2.5 cm) (a) and far radial distance (0-30 cm) (b) from the point of incidence of a 10 $\mu\text{m}$ wide pencil beam. Both the 6 and 15 MV beam responses have been normalized to unity in the central scoring bin.	110
Figure 4.6	The total number of optical photons scored on the exit surface of the optical filter as a function of the depth of the point of emission within the scintillation screen. $1.5 \times 10^7$ photons were initiated at each emission point.	111
Figure 4.7	The relative optical fluence reaching the photodiode plane as a function of radial distance, for four different emission depths. This set of four curves is a sample of the ten produced in this study. A distinct shoulder emerges on the curves for emission depths closest to the detection plane due to an increasing contribution from non-scattered optical photons.	112
Figure 4.8	$\langle \text{PSF}^{\text{opt}} \rangle$ for 6 MV (a) and 15 MV (a) beams. Single exponential fits to the data with attenuation coefficients $\lambda = 49.3$ and $49.5 \text{ cm}^{-1}$ , respectively, are also shown.	113
Figure 4.9	$\text{PSF}^{\text{overall}}(r)$ calculated for 6 and 15 MV beams, normalized to the central bin, shown in the near range (0-2.5 cm) (a) and far range (0-30 cm) (b). $\langle \text{PSF}^{\text{rad}}(r) \rangle$ is also shown at 6 MV to illustrate the change in the kernel due to optical spreading. The 15 MV kernel is broader inside a 5 cm radius due to increased lateral electron transport at the higher energy. The tails display similar behavior, running nearly parallel beyond 10 cm.  In (c) 6 MV results are shown for different thicknesses of solid water backscatter to gauge the relative contributions of backscatter and optical spreading. $\langle \text{PSF}^{\text{rad}}(r) \rangle$ is also shown in (d) to directly illustrate the influence of the solid water backscatter thickness on the dose deposition kernel. For the 0.0 cm case, the rear panel of the detector was also removed.	114- 115
Figure 4.10	The images used for the LSF measurement at 6 MV. The original slit image (a), the off set image (b) as well as the final image (c) resulting from subtracting the pixel values of image (b) from image (a). The images have been magnified by a factor of 2.5 to give a better view of the slit region.	116
Figure 4.11	The images used for the LSF measurement at 15 MV. The original slit image (a), the off set image (b) as well as the final image (c) resulting from subtracting the pixel values of image (b) from image (a). The images have been magnified by a factor of 2.5 to give a better view of the slit region.	117

Figure 4.12	A comparison of our 6 MV (a) and 15 MV (b) LSF experimental data with the LSF calculated from our simulated PSF. A windowed average fit of the data points (spanning 20 points) is shown for each case as well. The data and simulation agree well as they fall through over two orders of magnitude across a distance of 15 pixels.	118
Figure 4.13	Cross-plane (a) and in-plane (b) profiles for a 6 MV $10 \times 10$ cm <sup>2</sup> field after deconvolution with $\text{PSF}^{\text{overall}}$ , plotted along with flood field restored image and diamond detector profiles.	119- 120
	In (c) the deconvolution had been performed with $\langle \text{PSF}^{\text{rad}} \rangle$ in the cross-plane geometry. Differences due to the incorporation of the optical kernel are highlighted in (d), which focuses on the penumbra region where deconvolution has been performed both with (solid line) and without (dotted line) the optical kernel.	
Figure 4.14	Magnitudes of the $\chi$ scores corresponding to the image profiles in Fig. 4.12, cross-plane (a), and in-plane (b). Distinct peaks are seen in the high gradient regions both before and after deconvolution. The most substantial decrease is seen in the regions outside of the field.	121
Figure 4.15	Histograms comparing the $\chi$ scores of the flood field restored and deconvolved image profiles in Fig. 4.12, cross-plane (a and b), and in-plane (c and d). The dashed line on each histogram indicates a $\chi$ score of 1.0 – below which the difference is considered acceptable. Deconvolution increased the percentage of acceptable points from 49.0 % (a) to 92.0 % (b) cross-plane, and from 43.4 % (c) to 89.9 % (d) in-plane. The distributions indicate that after deconvolution the scores are more heavily weighted towards the low end (most acceptable – least discrepancy). Due to the high gradient regions at the edges of the field and the volume averaging inherent in the diamond detector measurement, some high $\chi$ scores cannot be avoided.	122
Figure 4.16	A $10 \times 10$ cm <sup>2</sup> 45° physically wedged field at 6 MV. Deconvolution improves the profile measurement outside of the field. Improvements inside the field are not apparent.	123
Figure 4.17	Comparison of different approaches to kernel calculation for the 6 MV beam. The solid line is the result derived from our comprehensive Monte Carlo model. The dotted line is a triple exponential function, obtained by fitting the comprehensive kernel, which could also be determined empirically. The open circles depict the result from our thin stack model, which differs in the tail region.	124



Figure 4.18	The blur kernels ( $LSF_{DD}(x)$ ) for the diamond detector. The FWHM is approximately 0.27 cm and 0.29 cm for the 6 and 15 MV beams, respectively. Error bars derive from the statistical uncertainties in the edge response function data.	125
Figure 4.19	A cross-plane profile for a 6 MV $10 \times 10$ cm <sup>2</sup> field corresponding to that shown in Fig. 4.13 (a). Here the diamond detector profile has been deconvolved using $LSF_{DD}(x)$ . The resulting diamond fluence is visibly sharper, but the fraction of $\chi$ scores $\leq 1$ is not increased significantly.	126- 127
	Cross-plane profiles for a 6 MV $2 \times 2$ cm <sup>2</sup> field, with the diamond detector profile deconvolved (b) and for comparison, before deconvolution (c). The fraction of $\chi$ scores $\leq 1$ noticeably improves after deconvolution of the diamond profile for this smaller field.	
Figure 5.1	The relative spectral distribution of photons (normalized to unit area) detected at a plane corresponding to an EPID setup at SDD = 105 cm for increasing steel shot thickness (a). The relative changes between the distributions are reduced with 1.0 cm of Cu placed 15 cm above the detection plane (b).	158
Figure 5.2	The relative dose to the EPID phosphor in the conventional setup with 0.5 cm of solid water on its surface, compared to the IIC response. The curves are normalized to one at 1.125 MeV. Above 1 MeV we note that the EPID response is quite similar to the IIC curve (mean difference of 9 %). Below 1 MeV there is a sharp rise in the EPID response due to a transition of dominant interaction processes in the EPID (photo-electric effect dominant), which gives rise to the discrepancy between open and attenuated beam dose calibration curves.	159
Figure 5.3	Mass energy-absorption coefficients plotted as a function of photon energy for Gd <sub>2</sub> O <sub>2</sub> S (GOS) and air. Air has a reasonably uniform coefficient from 0.1 MeV to 20 MeV. GOS however, has a distinct rise below $\sim 0.5$ MeV. The total attenuation coefficient for Cu has also been plotted to indicate the relative proportion of photons of a given energy that would interact in a Cu plate placed upstream from the phosphor.	160
Figure 5.4	The EPID dose response as a function of photon energy for different thicknesses of Cu plate placed in contact with the surface of the EPID. There is a more substantial reduction in the region below 1 MeV relative to the region above 1 MeV.	161
Figure 5.5	The EPID dose response as a function of photon energy for a 0.75 cm Cu plate in the contact and elevated configurations. Linear fits to the copper plate data above 1 MeV are shown in gray. In the region below 1 MeV, the elevated configuration comes closer to the approximately linear trend observable above 1 MeV than does the contact configuration.	162

Figure 5.6	The ratio of the phosphor dose with the EPID in the elevated configuration to that in the contact configuration for the energy bin centered at 0.375 MeV and a Cu plate thickness of 0.5 cm. Based on this data, an elevation of 15 cm was chosen for subsequent investigations.	163
Figure 5.7	Monte Carlo simulated calibration curves for a 105 cm SDD attenuated beam scenario. Shown are curves for the conventional setup and for the contact and elevated configurations including a 0.75 cm Cu plate. Results have been normalized to the open field (no compensator) case. The lowest relative doses and ion chamber response correspond to the thickest compensator (4.5 cm steel shot).	164
Figure 5.8	The maximum difference between an assumed ideal (linear) EPID calibration curve and simulated calibration curves for a beam attenuated by varying thicknesses of steel shot. The error bars derive from uncertainties in the fit coefficients obtained in the regression analysis.	165
Figure 5.9	Experimental calibration curves where the attenuated beam measurements were made at 105 cm SDD (a) and 140 cm SDD (b) respectively. Maximum differences between the attenuated beam data and the open field trend lines (extrapolated in the 140 cm SDD case) are 8.2% and 7.7% respectively.	166
Figure 5.10	Calibration curves modified by the addition of 9.45 mm of Cu in the contact (a) and elevated (b) configurations. The maximum deviation was reduced from 8.2% in the conventional setup to 6.4 % in the contact and 3.2 % in the elevated configurations.	167
Figure 5.11	The maximum discrepancy between the measured EPID response for an open field and an attenuated field at 105 cm SDD as Cu thickness is increased in both the contact and elevated configurations. The error bars derive from uncertainties in the fit coefficients.	168
Figure 5.12	Calibration curves for the 6 MV beam hardened by a stack of solid water. A similar difference in the curves as for the steel shot was observed, the maximum difference here being 6.5%. Adding $0.630 \pm 0.04$ cm of Cu in the elevated configuration reduced the maximum difference to 3.7%.	169
Figure 5.13	The relative contrast-to-noise ratio (CNR) as a function of external Cu plate thickness. CNR is reduced substantially in both configurations, but the drop is greatest for the elevated plate case. This is possibly due to a reduction in contrast otherwise present with more scattered photons from the Cu reaching the phosphor in the contact configuration.	170
Figure 5.14	Ratio of $MTF^{Cu}$ to $MTF^{SW}$ for the conventional configuration vs. Cu thickness measured using the QC-3V phantom for the contact (a) and elevated (b) configurations.	171

## List of Symbols

A	Atomic mass (in g/mol)
c	Speed of light in vacuum
C	Calibration factor
Cu	Copper
D	Dose
$\dot{D}$	Dose rate
$(dT/\rho dx)_A$	Restricted collisional stopping power
$e^-$	Electron
E	Total energy in MeV
$f_1(z)$	Single event spectrum
$f_{50}$	Frequency at which MTF = 0.5
G	Estimator
I	Mean ionization energy (also used for current in chapter 1)
$I(x,y)$	Image
$k_1$	First elastic scattering moment
$k_{FFmean}$	Mean value of flood field pixel values
$K_C^{cav}$	Cavity collision kerma
l	Distance from point source
$m_0c^2$	Rest mass for an electron (0.511 MeV)
n	Number of dimensions
N	Number of histories in a Monte Carlo simulation
$N_A$	Avagadro's number ( $6.022 \times 10^{23}$ )
$n_e$	Electron density
p	Probability density
pc	Electron momentum · speed of light
r	Radial co-ordinate (also random variable in Ch.3)
$r(E_i)$	EPID response to monochromatic beam
$r_0$	Classical radius of the electron
$R_{EPID}$	Overall EPID dose response
$\mathfrak{R}_{EPID}$	Relative EPID pixel value
$\mathfrak{R}_{IC}$	Relative ion chamber reading
t	Path length
T	Kinetic energy in MeV
U	Random vector
$w_{zi}$	Optical weighting factor
z	Specific energy
$z_i$	Discrete depth co-ordinate
$\langle z_f \rangle$	Frequency-mean specific energy
Z	Atomic Number
$\beta$	Electron velocity in light speed units
$\chi$	Acceptance test parameter
$\delta$	Density effect parameter

$\gamma$	Acceptance test parameter
$\Gamma$	Arbitrary quantity
$\Delta$	Kinetic energy of delta rays escaping foil
$\Delta d_{\max}$	Maximum acceptable dose distance-to-agreement
$\Delta D_{\max}$	Maximum acceptable dose difference at a point
$\Phi$	Fluence (particles/cm <sup>2</sup> )
$\phi(E_i)$	Fluence of incident photons of energy $E_i$
$\lambda$	Exponential decay parameter (also used as absorption coefficient)
$\mu$	Interaction coefficient
$\left(\frac{\mu_{\text{EN}}}{\rho}\right)_{E_i}^{\text{air}}$	mass energy-absorption coefficient for air at energy $E_i$
$\theta$	Scattering angle
$\rho$	Density
$\sigma$	Standard deviation
$\psi$	Energy fluence

## List of Abbreviations

2D	Two dimensional
3D	Three dimensional
AE	Array threshold electron energy for PEGS4 data generation
AP	Array threshold photon energy for PEGS4 data generation
a-Si	Amorphous silicon
a-Si:H	Hydrogenated amorphous silicon
CAX	Central beam axis
CNR	Contrast-to-noise ratio
CR	Computed radiography
CSDA	Continuous slowing down approximation
CT	Computed tomography
DF	Dark field
DRR	Digitally reconstructed radiograph
DQE	Detective quantum efficiency
ECUT	Electron cut-off energy
EGS	Electron gamma shower
EPID	Electronic portal imaging device
FF	Flood field
FT	Fourier transform
FT <sup>-1</sup>	Inverse Fourier transform
FWHM	Full width half maximum
GeV	Giga electron volts
Gy	Gray
IIC	Ideal ion chamber
ICRU	International Commission on Radiation Units and Measurement
IMRT	Intensity modulated radiotherapy
keV	Kilo electron volts
kV	Kilovoltage
Linac	Linear accelerator
LSF	Line Spread Function
MeV	Mega electron volts
MFP	Mean free path
MLC	Multi-leaf collimator
MRI	Magnet Resonance Imaging
MTF	Modulation transfer function
MU	Monitor unit
MV	Megavoltage
PCUT	Photon cut-off energy
PEGS4	Preprocessor for EGS4 (and EGSnrc)
PET	Positron emission tomography
PSF	Point spread function
PV	Pixel value
POI	Region of interest
SDD	Source-to-detector distance

SLAC	Stanford linear accelerator center
SWMTF	Square wave modulation transfer function
TPS	Treatment planning system
TFT	Thin film transistor
TLD	Thermoluminescent dosimeter
TV	Television
V	Voltage

# Chapter 1: Introduction

## 1.1 OVERVIEW

The main goal of this study was to take an existing electronic portal imaging device (EPID), specifically the Varian aS500, and, through a rigorous study of the physics that underlie its operation, improve its operational performance for dosimetry applications. Originally developed as an imaging tool for the verification of patient positioning during a course of radiation therapy, the detection characteristics of this device also make it attractive for quantitative radiation measurement. Such measurement would allow for the role of the EPID to be extended to operations like intensity modulated radiotherapy (IMRT) field verification, compensator thickness verification, and patient transmission dosimetry. The work presented herein determines some key characteristics of this commercially available device that need to be understood in the context of dose measurement. Further, it quantitatively establishes the consequences of these characteristics, and suggests approaches to operational improvement. In this introductory chapter we ground the work in the context of radiation therapy as a modality for cancer treatment, introduce the EPID as a flat panel imager, and motivate the research to be presented.

## 1.2 RADIATION THERAPY AND CANCER

Approximately 145 500 Canadians are estimated to have developed cancer in 2004.<sup>1</sup> Cancer itself is actually a group of diseases in which abnormal cells proliferate

in an uncontrolled manner. As the cells divide, they can form an abnormal lump or mass known as a tumour. Cancerous tumours can invade and destroy healthy tissue and even spread to other parts of the body, a state known as metastasis.<sup>2</sup> The tumour then competes with healthy tissues for the body's resources, which can lead to undesirable symptoms and eventually even death.

Over one-half of those individuals diagnosed with cancer will receive radiation therapy (or radiotherapy) as a treatment. The general principle behind this therapy is that ionising radiation (such as gamma rays, beta particles, x-rays, etc.) can be used to either kill or damage localised proliferating cancer cells while sparing a higher proportion of healthy cells. The body then naturally eliminates the dead cells and the progress of the disease is halted. In advanced disease, radiation therapy can also be used for palliation, slowing the proliferation of tumour cells and reducing undesirable symptoms and pain.<sup>2</sup>

After a patient has been diagnosed with cancer amenable to management with radiotherapy, the information from various imaging modalities such as computed tomography (CT) and magnetic resonance imaging (MRI) can be used to identify a treatment volume to which a specified dose of radiation can be applied. Basically two techniques are used to deliver the radiation: (i) external beam therapy where the radiation comes from an external source, such as a linear accelerator (linac) or radioisotope machine (i.e. Co-60 unit), and (ii) brachytherapy where small radiation sources are placed in contact with, or in proximity to the treatment volume (often



implanted either temporarily or permanently within the patient). The criteria for deciding which modality is best suited to treating a particular form of cancer are based on the stage of the disease, its known response to treatment with a particular modality, and the technology and resources which are available in the clinic.

Tumour control probability can be maximised and normal tissue complication probability minimised when the radiation is delivered in a manner that yields a tumouricidal dose to the tumour volume, while minimising the dose to the surrounding tissues and proximal critical structures. In other words, the goal of radiation therapy is to get enough radiation into the tumour to effect a cure, and as little as possible into the rest of the body. In external beam therapy (of primary interest in this work), curative or radical treatments are fractionated (split up over a period of ~ 6 weeks) so that irradiated healthy tissues have an opportunity to recover.<sup>3</sup> To disperse the dose delivered to healthy tissue, the patient is typically irradiated from multiple directions. As such, the maximum absorbed dose accumulates only in the treatment volume where the radiation beams overlap.

Innovations such as conformal therapy and IMRT, where treatment fields (and corresponding dose distributions) are shaped using dynamic methods involving multi-leaf collimators (MLCs) and calculated using inverse planning methods,<sup>4,5</sup> allow for delivery of more complex dose distributions that have a closer correspondence to the actual tumour shape. Further, they allow for the prescription of higher doses.

Tomotherapy is a state of the art technique that takes the idea of multiple irradiations from different directions to a logical extreme, where the source is rotated in a helical

fashion around the patient.<sup>6</sup> Future directions point towards adaptive radiotherapy<sup>7,8</sup> and the more intimate incorporation of biological effects in treatment plans<sup>9</sup> that will allow treatment to be tailored more specifically to the individual patient's response to the therapy.

With increased doses to tumour volumes it becomes increasingly necessary to ensure the accuracy of treatment fields and doses in order to maximise the benefits of radiation therapy and minimise the complications.<sup>10</sup> Even small changes in the dose distribution can significantly affect tumour control and/or increase the probability of complications. The International Commission on Radiation Units and Measurements (ICRU) states that the overall accuracy in dose delivery should be  $\pm 5\%$  or lower.<sup>11</sup> Modern treatment planning systems are expected to adhere to even stricter limits such as  $\pm 2\%$  in low dose gradient regions.<sup>12</sup> This is a rather strict criterion when one considers the potential sources of uncertainty in a radiotherapy treatment procedure. These include: variability in machine output, patient alignment and motion, organ motion, leakage radiation, mechanical alignments, compensator and cut-out fabrication, alignment of anatomy with markers, etc.<sup>13-16</sup> Further, significant errors can be introduced as a result of inadequacies in treatment planning systems.<sup>17-20</sup> It is therefore understandable that a substantial effort is made by professionals involved with the radiation therapy process to minimise these uncertainties.

### 1.3 PORTAL IMAGING AND DOSIMETRY IN RADIOTHERAPY

Portal imaging is a technique that historically involved placing an x-ray film behind the patient to produce a setup verification image based on the exit radiation. Because the energies of the photons involved are significantly higher than those used for diagnostic imaging (megavoltage (MV) versus kilovoltage (kV)), the photon interactions that take place as the photons transit the patient tend to be predominantly Compton scattering events, which results in a lower overall contrast in the image.<sup>21</sup> Besides patient and field setup verification, portal images can also be used for dosimetric verification.

Setup verification can detect a large number of potential problems because a portal image can show the position of a patient's bony anatomy relative to the edges of the radiation field. The portal image can be compared with a localisation image captured by a treatment simulator, or with a digitally reconstructed radiograph (DRR) produced from CT data. Discrepancies between the two images may indicate setup errors. Clinical implementation of a regular portal imaging protocol can detect gross setup errors (eg. switched field dimensions), as well as errors in patient positioning and field positioning (both of which have been shown to exceed 10 mm on occasion).<sup>22</sup> Because systematic errors in patient setup can be minimised after the first few treatment fractions,<sup>22</sup> the associated cumulative errors in dose delivery can be largely avoided.

Dosimetric information can also be extracted from portal images of treatment fields (imaging fields are generally open fields). The major advantage of making dose measurements with a portal imager is that it provides a two dimensional (2D) map of dose in a plane behind the patient. In contrast, ion chambers provide point measurements. In one approach, investigators can generate a simulated portal image using a treatment planning system, and then compare it to an actual image in order to identify inconsistencies between what is planned and what is delivered.<sup>23</sup>

Alternatively, the measured image can be processed to yield an estimate of the dose or fluence in various planes.<sup>18,20,24</sup> In figure 1.1 we present a sample of the different planes of interest for radiotherapy. The transmission dose plane lies beyond the patient and corresponds to the image formation plane inside the detector. Based on the doses observed in this plane (with patient present and absent), techniques exist to predict the dose in the entrance, mid-patient and exit planes.<sup>24-27</sup> Note that the entrance plane is defined at the depth of dose maximum on the central axis (CAX). The exit plane is defined at the depth of dose maximum upstream from the patient's exit surface, and the mid-patient plane is defined as being half way between the entrance and exit planes. Once the dose has been measured in the transmission plane, the exit dose can be determined as follows. First, the primary dose is derived (contributions from scatter are estimated and subtracted). Then, the resulting primary transmission dose image can be back-projected to the exit surface of the patient to yield the primary exit dose. Finally, the scatter exit dose can be estimated by convolving the primary exit dose with a scatter kernel, and this can be added to the primary contribution.<sup>27</sup> A number of methods have been suggested for determining

the mid-plane dose, ranging from a simple linear average of entrance and exit doses, to more sophisticated algorithms that incorporate CT or depth dose data to predict how patient attenuation effects modify the entrance or exit dose.<sup>27</sup>

#### 1.4 ELECTRONIC PORTAL IMAGING DEVICES

Traditionally, film (coupled with a screen inside a cassette) has been the technology of choice with which to obtain portal images because of its high spatial resolution and ready availability. By calibrating the optical density of exposed film to dose, it is also possible to use it for portal dosimetry. There are some substantial drawbacks to film however, which have prompted investigators to explore other technologies. For example with film, the radiation therapist is required to spend time loading, setting up, and processing the film medium (while the patient is lying on the couch).<sup>28</sup> Film is subject to processing errors, and must be physically archived or digitally scanned.<sup>28</sup> And most importantly for dose measurement, it presents a number of challenges because its dose response is non-linear, dependent on processing variables, and subject to manufacturing variability from batch to batch. In an ideal scenario, these problems could be solved using an electronic device that provides equivalent image quality for a similar (or smaller) radiation exposure.

Precursor technologies to the amorphous silicon (a-Si) type EPID that is the focus of the present work include matrix ion chamber and TV camera-based systems.<sup>29</sup> Other alternatives to film besides EPIDs include scanning systems, where

the radiation detector subtends only a small fraction of the radiation beam and must scan the area of interest to produce an image. Because much of the transmission dosimetry work was pioneered with the matrix ion chamber and TV camera-based systems, we briefly outline their characteristics here.

In TV camera-based systems a copper plate and underlying phosphor screen (such as  $\text{Gd}_2\text{O}_2\text{S}$ ) make up the x-ray detector. When the copper plate is irradiated electrons are produced, which then interact with the screen causing it to phosphoresce. The optical photons emerging from the screen are then reflected onto a video camera using a  $45^\circ$  mirror, and the video signal is recorded and digitised. The angular distribution of optical photons is very wide and as a result only 0.01 to 0.1 % of the emitted photons are detected by the camera.<sup>29</sup> These devices also suffer from significant glare (scattered optical photons) and distortions.<sup>30</sup>

A matrix ion chamber uses a different approach to form an image. Originally developed by Meertens and van Herk,<sup>31</sup> this device consists of two sets of electrodes (typically  $\sim 256 \times 256$ ) oriented perpendicular to each other. The electrodes are separated by a gap (typically  $\sim 0.8$  mm) that is filled with a fluid, which becomes ionised when the device is irradiated. One set of electrodes is connected to a bank of electrometers while the other is connected through a multi-position switch to a high voltage power supply. The device is read out by applying a high voltage to each of the electrodes in succession and reading out the electrometers in between. One of the major limitations of this type of technology is that only one of the high voltage

electrodes is active at any one time, limiting the overall radiation sensitivity of the EPID. Furthermore, the resulting current  $I$  (proportional to the pixel value) is related to the dose rate  $\dot{D}$ , by the square root relation<sup>32</sup>

$$I = a\dot{D}^{\frac{1}{2}} + b\dot{D} \quad (1.1)$$

where  $a$  and  $b$  are device-specific parameters. Naturally this leads to additional complexity in dose calibration and measurement.

Recent advances in active-matrix technology have allowed for semiconductors (such as a-Si) to be deposited in a controlled manner across large area substrates, which has led to the fabrication of flat-panel x-ray imagers.<sup>28</sup> The detection schemes used by flat panel imagers can be subdivided into two categories: *direct* and *indirect*.<sup>33</sup>

In the direct detection scheme, image information is essentially transferred directly from the incident x-rays to electrical charge, with no intermediate stage. In these devices a thick layer of photoconductive material such as amorphous selenium<sup>28,34</sup> is placed in direct electrical contact with an underlying flat panel array. Interacting x-rays create charge in the photoconductor, which is then collected and stored by a conductive electrode and capacitor that are incorporated into each pixel of the flat panel.

In the indirect detection scheme an intermediate process takes place between the x-ray interaction and the collection of charge. A phosphor such as  $\text{Gd}_2\text{O}_2\text{S:Tb}$  is

placed in contact with the active-matrix array to generate an emission of optical light in response to x-ray irradiation. The optical photon fluence is presumed to be proportional to the energy of the x-ray beam incident on the surface of the detector directly above it (quantum detection efficiency is approximately 0.018-0.02).<sup>35</sup> The optical light is then collected in each pixel of the active matrix by a photosensitive element that generates an electrical charge that is stored until the active matrix is read out. The EPID used in the present work employs an indirect detection scheme and is discussed in detail in Chapter 2.

## 1.5 THE MONTE CARLO METHOD

The majority of the studies conducted in the present work employed Monte Carlo techniques to simulate the transport of both ionising and non-ionising radiation. In order to understand the operation of the a-Si EPID we simulated a variety of physical processes. These included the spreading of dose in the phosphor in response to an incident pencil beam of photons, the propagation of optical photons emitted from an isotropic point source inside the phosphor and subsequently impinging onto the photodiode plane, the changes to a 6 MV linac photon spectrum arising from passage through a steel shot attenuator, and the dose response of the phosphor to a monoenergetic incident photon beam. Each of these processes is very difficult to examine experimentally. The problem of dose spreading in the phosphor, for example, would require a very sensitive detector able to measure doses over several orders of magnitude across sub-millimetre dimensions. Furthermore, analytical



solutions only become practical after making fairly severe approximations. The problem of optical spreading in the phosphor, for example, was initially investigated as a first-scatter ray-tracing problem that could be solved analytically, but it was found that the contribution from multiply scattered photons could not be ignored. A fully accurate treatment increases the complexity of this problem substantially, making an analytical solution impractical.

The Monte Carlo method provides a practical approach to estimating reasonable solutions to the problems encountered in the present work. Essentially the method uses statistical sampling of a large number of microscopic processes occurring in a system to predict the macroscopic behaviour of that system. Radiation transport can be simulated by considering the fundamental interactions that occur between particles in the radiation beam and those in irradiated objects. The specific details of the simulations employed in the present work are described in chapter 3. At this point however, we can introduce the basic Monte Carlo formalism.<sup>36,37</sup>

The Monte Carlo method is used to obtain an approximate solution to problems that can be represented in integral form. Thus we consider a general  $n$ -dimensional integral that yields an arbitrary quantity  $\Gamma$

$$\Gamma = \int_0^1 \int_0^1 \dots \int_0^1 f(u_1, u_2, \dots, u_n) du_1 du_2 \dots du_n = \int_{u_i=0}^{u_i=1} f(\mathbf{u}) d\mathbf{u}. \quad (1.2)$$

The Monte Carlo method obtains an approximate solution to this integral using a random vector  $\mathbf{U}$ , which is uniformly distributed over the region of integration.

Using the function  $f$ , we can generate a random variable  $f(\mathbf{U})$ . The expectation value for this random variable is then

$$\langle f(\mathbf{U}) \rangle = \int_{u_i=0}^{u_i=1} f(\mathbf{u}) p(\mathbf{u}) d\mathbf{u}, \quad (1.3)$$

where  $p(\mathbf{u})$  is the probability density function of  $\mathbf{U}$ . However,  $\mathbf{U}$  was defined as being uniformly distributed over the region of integration, so  $p(\mathbf{u})$  is constant (and can be put to unity in this formalism), hence

$$\langle f(\mathbf{U}) \rangle = \int_{u_i=0}^{u_i=1} f(\mathbf{u}) d\mathbf{u}. \quad (1.4)$$

Based on Eq's. 1.2 and 1.4 we can obtain a probabilistic expression for  $\Gamma$

$$\Gamma = \langle f(\mathbf{U}) \rangle. \quad (1.5)$$

Thus we have a random variable  $f(\mathbf{U})$  with a mean value of  $\Gamma$  and some standard deviation  $\sigma$ . Hence, we can define an unbiased estimator of  $\Gamma$  based on a single sample of  $\mathbf{U}^{[1]}$

$$g = f(\mathbf{U}^{[1]}). \quad (1.6)$$

If we want to obtain a reasonable estimate of  $\Gamma$  and reduce the standard error to less than  $\sigma$ , the estimator needs to be generalised to a sample of  $N$  random vectors  $\{\mathbf{U}^{[1]}, \mathbf{U}^{[2]}, \dots, \mathbf{U}^{[N]}\}$ . Applying the function  $f$  to each vector generates  $N$  independent and identically distributed random variables  $f\mathbf{U}^{[1]}, f\mathbf{U}^{[2]}, \dots, f\mathbf{U}^{[N]}$  – all with an expectation value  $\Gamma$  and a standard deviation  $\sigma$ . Eq. 1.6 can then be generalised such that an estimator  $G$  can be defined as

$$G = \frac{1}{N} \sum_{k=1}^N f(\mathbf{U}^{[k]}). \quad (1.7)$$

This is an unbiased estimator of  $\Gamma$  with a standard error  $\delta G$  of

$$\delta G = \frac{\sigma}{\sqrt{N}}. \quad (1.8)$$

The advantage of the Monte Carlo method is apparent at this point. First of all in Eq. 1.8 we see that the standard error in the estimator  $G$  of  $\Gamma$  decreases with the square root of the sample size  $N$ . More importantly the estimator is independent of the dimensionality of the problem,  $n$ . It depends only on the sample size,  $N$ . Other analytic or deterministic approaches to problems of the kind illustrated by Eq. 1.2 exhibit a dependence on  $n$ . In general, the number of computations required to solve the problem increases exponentially with  $n$ , thus limiting the application of such methods to integrals of only a few dimensions (or to integrals of higher dimension simplified by approximations that limit the applicability of the solution). In figure 1.2 (based on a similar figure presented by Bielajew<sup>38</sup>) we depict the Monte Carlo advantage on an arbitrary scale. As the complexity of the problem increases, we reach an intersection point where the Monte Carlo method becomes a more efficient means of finding a solution. The problems associated with radiation detection by an a-Si EPID discussed earlier fall into a category where the complexity is sufficient that the Monte Carlo method is far more practical than analytic or deterministic methods.

## 1.6 OVERVIEW OF THE THESIS

As stated at the outset of the chapter, the goal of this work was to improve the operational performance of the Varian aS500 EPID for portal dosimetry applications

through a rigorous study of the physics that underlie its operation. Specifically we concentrated on two areas: blur kernel development and dose calibration.

A blur kernel describes the response of an imaging system to a pencil beam of radiation. An accurate blur kernel is necessary so that the raw EPID image can be processed to obtain a map of transmission fluence through a standard deconvolution process. While other authors have generated approximate blur kernels, the present work addressed several outstanding issues. We used Monte Carlo techniques to generate a blur kernel based on a comprehensive model of the detector (as opposed to a simpler generic model), and we simulated the optical component of the blur kernel to understand the effects of optical photon spreading in relation to the overall blurring process. We were able to verify our simulated results through a comparison with an experimentally measured line spread function. Further, we were able to fit analytical forms to both the overall and optical blur kernels. Finally, we were able to quantify the accuracy of fluence profile recovery using blur kernels obtained through a variety of means.

Dose calibration relates EPID image pixel values to ion chamber readings obtained at the same spatial location. For the aS500 the calibration curve is generally linear. However, Menon and Sloboda<sup>39</sup> observed a significant calibration discrepancy when comparing the response in an open beam to that in an attenuated beam. We were able to reproduce this experiment and quantify the maximum variation. Monte Carlo modelling confirmed our suspicion that the discrepancy was due to an increase in the

dose response of the phosphor screen to lower energy photons. Although the aS500 already contains an internal copper plate, we used an additional, external copper plate to partially remove the low energy photons preferentially and reduce the variation to acceptable levels. With this in place we measured the consequent effects on the imaging properties of the EPID.

The work that follows is organised to provide a logical record of these investigations. In chapter 2, we present a detailed overview of the characteristics and operation of the aS500 EPID. Chapter 3 examines the Monte Carlo method extensively as it relates to radiation transport. We describe EGSnrc and DETECT 2000, the simulation codes used to model the transport of ionising and optical radiation, respectively. We also present some in-house benchmarking for EGSnrc, as well as some additional work performed in the fields of microdosimetry and nuclear medicine.<sup>40</sup> The following chapters comprise the majority of the scientific investigations undertaken. Chapter 4 presents the development and application of various blur kernels for energy fluence measurement with an aS500 EPID.<sup>41</sup> Chapter 5 examines the dose calibration of the EPID in attenuated fields, and describes the work done to reduce the observed calibration discrepancies.<sup>42</sup> Finally, chapter 6 concludes with a summary of our work and discussion of future directions in this field.

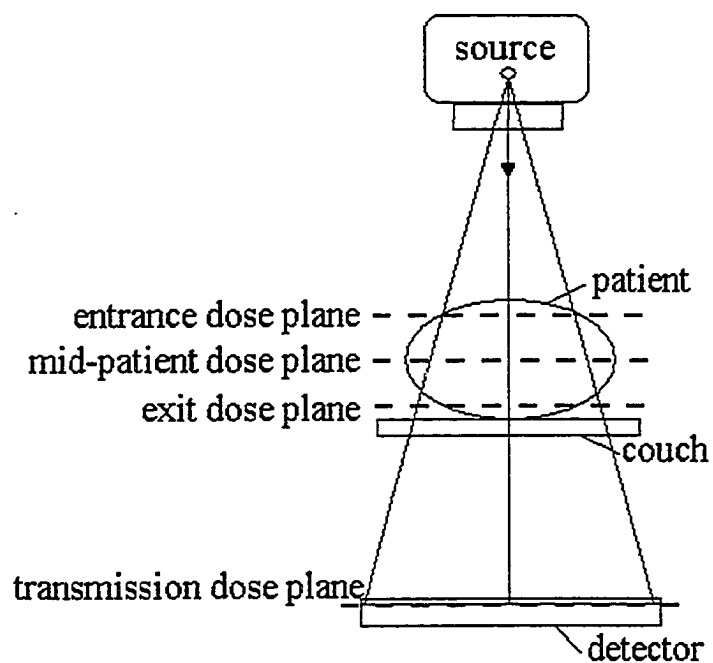


**Figure 1.1.** A schematic illustration of the various planes of interest in portal dosimetry.

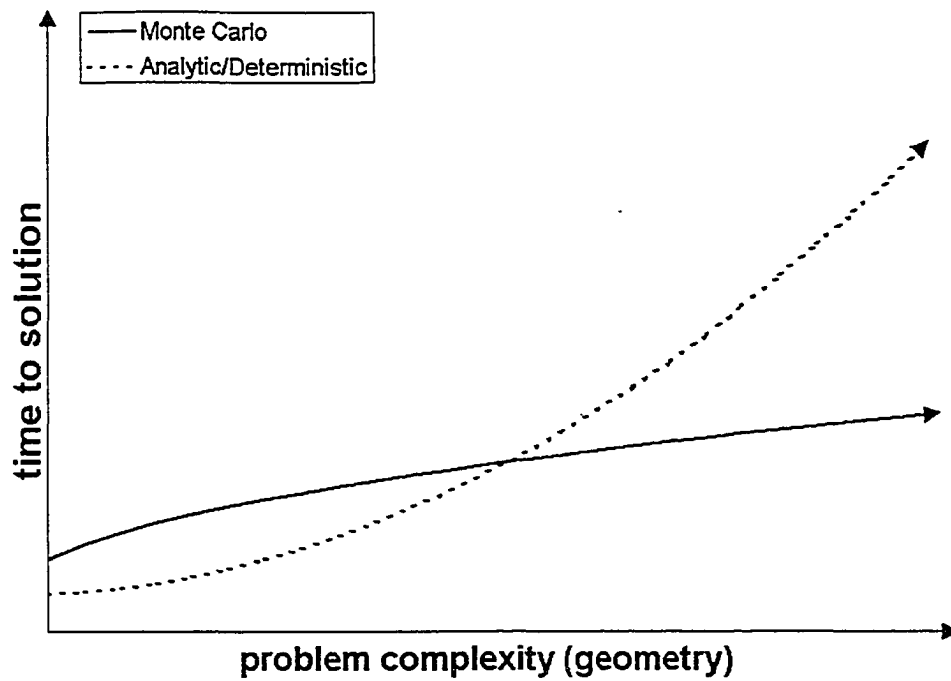


**Figure 1.2.** The time to solution for the Monte Carlo method as compared to analytic or deterministic approaches. As the complexity of the problem increases, Monte Carlo offers a more efficient means to solve a given problem.

## 1.7 REFERENCES

- <sup>1</sup>National Cancer Institute of Canada, *Canadian Cancer Statistics 2004* (National Cancer Institute of Canada, Toronto, ON, 2004).
- <sup>2</sup>ASTRO, Radiation Therapy for Cancer: Facts to Help Patients Make an Informed Decision, 2004.
- <sup>3</sup>E. A. Alpen, *Radiation Biophysics*, 2 ed. (Academic Press, New York, NY, 1998).
- <sup>4</sup>T. Bortfeld, J. Burkelbach, R. Boesecke, and W. Schlegel, "Methods of image reconstruction from projections applied to conformation radiotherapy," *Phys Med Biol* **35** (10), 1423-34 (1990).
- <sup>5</sup>A. Brahme, "Optimization of stationary and moving beam radiation therapy techniques," *Radiother Oncol* **12** (2), 129-40 (1988).
- <sup>6</sup>T. R. Mackie, J. Balog, K. Ruchala, D. Shepard, S. Aldridge, E. Fitchard, P. Reckwerdt, G. Olivera, T. McNutt, and M. Mehta, "Tomotherapy," *Semin Radiat Oncol* **9** (1), 108-17 (1999).
- <sup>7</sup>A. A. Martinez, D. Yan, D. Lockman, D. Brabbins, K. Kota, M. Sharpe, D. A. Jaffray, F. Vicini, and J. Wong, "Improvement in dose escalation using the process of adaptive radiotherapy combined with three-dimensional conformal or intensity-modulated beams for prostate cancer," *Int J Radiat Oncol Biol Phys* **50** (5), 1226-34 (2001).
- <sup>8</sup>D. Brabbins, A. Martinez, D. Yan, D. Lockman, M. Wallace, G. Gustafson, P. Chen, F. Vicini, and J. Wong, "A dose-escalation trial with the adaptive radiotherapy process as a delivery system in localized prostate cancer: Analysis of chronic toxicity," *Int J Radiat Oncol Biol Phys* **61** (2), 400-8 (2005).
- <sup>9</sup>P. Stavrev, D. Hristov, B. Warkentin, E. Sham, N. Stavreva, and B. G. Fallone, "Inverse treatment planning by physically constrained minimization of a biological objective function," *Med Phys* **30** (11), 2948-58 (2003).
- <sup>10</sup>M. G. Herman, R. A. Abrams, and R. R. Mayer, "Clinical use of on-line portal imaging for daily patient treatment verification," *Int J Radiat Oncol Biol Phys* **28**, 1017-1023 (1994).
- <sup>11</sup>ICRU, ICRU Report 24: Determination of absorbed dose in a patient irradiated by beams of X or gamma rays in radiotherapy procedures, 1976.
- <sup>12</sup>J. Van Dyk, "Quality Assurance," in *Treatment Planning in Radiation Oncology*, edited by F.M. and Potish Khan, R.A. (Williams & Wilkins, Baltimore, MA, 1998), pp. 131.



- <sup>13</sup>A. G. Haus and J. E. Marks, "Detection and evaluation of localization errors in patient radiation therapy," *Invest Radiol* **8** (6), 384-91 (1973).
- <sup>14</sup>I. Rabinowitz, J. Broomberg, M. Goitein, K. McCarthy, and J. Leong, "Accuracy of radiation field alignment in clinical practice," *Int J Radiat Oncol Biol Phys* **11** (10), 1857-67 (1985).
- <sup>15</sup>E. E. Klein and D. A. Low, "Interleaf leakage for 5 and 10 mm dynamic multileaf collimation systems incorporating patient motion," *Med Phys* **28** (8), 1703-10 (2001).
- <sup>16</sup>G. Baroni, G. Ferrigno, R. Orecchia, and A. Pedotti, "Real-time three-dimensional motion analysis for patient positioning verification," *Radiother Oncol* **54** (1), 21-7 (2000).
- <sup>17</sup>C. M. Ma, E. Mok, A. Kapur, T. Pawlicki, D. Findley, S. Brain, K. Forster, and A. L. Boyer, "Clinical implementation of a Monte Carlo treatment planning system," *Med Phys* **26** (10), 2133-43 (1999).
- <sup>18</sup>B. Warkentin, S. Steciw, S. Rathee, and B. G. Fallone, "Dosimetric IMRT verification with a flat-panel EPID," *Med Phys* **30** (12), 3143-55 (2003).
- <sup>19</sup>J. W. Wong and J. A. Purdy, "On methods of inhomogeneity corrections for photon transport," *Med Phys* **17** (5), 807-14 (1990).
- <sup>20</sup>B. Warkentin, "Development of Verification Procedures using a Flat-Panel EPID, and Application and Investigation of Radiobiological Models, for Intensity-Modulated Radiotherapy," Ph.D. Thesis, University of Alberta, 2005.
- <sup>21</sup>H. E. Johns and J. R. Cunningham, *The Physics of Radiology 4th ed.* (Springfield: Charles C. Thomas, Springfield, IL, 1983).
- <sup>22</sup>C. L. Thomason, "Implementation and clinical use of portal imaging," *Cancer Treat Res* **93**, 69-99 (1998).
- <sup>23</sup>J. V. Siebers, J. O. Kim, L. Ko, P. J. Keall, and R. Mohan, "Monte Carlo computation of dosimetric amorphous silicon electronic portal images," *Med Phys* **31** (7), 2135-46 (2004).
- <sup>24</sup>T. R. McNutt, T. R. Mackie, P. Reckwerdt, and B. R. Paliwal, "Modeling dose distributions from portal dose images using the convolution/superposition method," *Med Phys* **23** (8), 1381-92 (1996).
- <sup>25</sup>R. Boellaard, M. van Herk, and B. J. Mijnheer, "A convolution model to convert transmission dose images to exit dose distributions," *Med Phys* **24** (2), 189-99 (1997).

- <sup>26</sup>C. Fiorino, A. del Vecchio, G. M. Cattaneo, M. Fusca, B. Longobardi, P. Signorotto, and R. Calandrino, "Exit dose measurements by portal film dosimetry," *Radiother Oncol* **29** (3), 336-40 (1993).
- <sup>27</sup>R. Boellaard, M. Essers, M. van Herk, and B. J. Mijnheer, "New method to obtain the midplane dose using portal in vivo dosimetry," *Int J Radiat Oncol Biol Phys* **41** (2), 465-74 (1998).
- <sup>28</sup>J. A. Rowlands and J. Yorkston, "Flat Panel Detectors for Digital Radiography," in *Handbook of Medical Imaging* (SPIE Press, Bellingham WA, 2000), pp. 223 - 328.
- <sup>29</sup>P. Munro, "Portal Imaging Technology: Past, Present, and Future," *Semin Radiat Oncol* **5** (2), 115-133 (1995).
- <sup>30</sup>B. J. Heijmen, K. L. Pasma, M. Kroonwijk, V. G. Althof, J. C. de Boer, A. G. Visser, and H. Huizenga, "Portal dose measurement in radiotherapy using an electronic portal imaging device (EPID)," *Phys Med Biol* **40** (11), 1943-55 (1995).
- <sup>31</sup>M. van Herk and H. Meertens, "A matrix ionisation chamber imaging device for on-line patient setup verification during radiotherapy," *Radiother Oncol* **11** (4), 369-78 (1988).
- <sup>32</sup>M. Essers, B. R. Hoogervorst, M. van Herk, H. Lanson, and B. J. Mijnheer, "Dosimetric characteristics of a liquid-filled electronic portal imaging device," *Int J Radiat Oncol Biol Phys* **33** (5), 1265-72 (1995).
- <sup>33</sup>Y. El-Mohri, L. E. Antonuk, J. Yorkston, K. W. Jee, M. Maolinbay, K. L. Lam, and J. H. Siewerdsen, "Relative dosimetry using active matrix flat-panel imager (AMFPI) technology," *Med Phys* **26** (8), 1530-41 (1999).
- <sup>34</sup>M. Lachaine, E. Fourkal, and B. G. Fallone, "Detective quantum efficiency of a direct-detection active matrix flat panel imager at megavoltage energies," *Med Phys* **28** (7), 1364-72 (2001).
- <sup>35</sup>Y. El-Mohri, K. W. Jee, L. E. Antonuk, M. Maolinbay, and Q. Zhao, "Determination of the detective quantum efficiency of a prototype, megavoltage indirect detection, active matrix flat-panel imager," *Med Phys* **28** (12), 2538-50 (2001).
- <sup>36</sup>R. Y. Rubinstein, *Simulation and the Monte Carlo Method*, 1 ed. (Wiley-Interscience, Hoboken, NJ, 1981).
- <sup>37</sup>G.S. Fishman, *Monte Carlo Concepts, Algorithms and Applications*, 1 ed. (Springer Verlag, London, 1996).

<sup>38</sup>A. F. Bielajew, *Fundamentals of the Monte Carlo method for neutral and charged particle transport* (pre-publication manuscript, Ann Arbor MI, 2001).

<sup>39</sup>G. V. Menon and R. S. Sloboda, "Compensator quality control with an amorphous silicon EPID," *Med Phys* **30** (7), 1816-24 (2003).

<sup>40</sup>A. M. Syme, C. Kirkby, T. A. Riauka, B. G. Fallone, and S. A. McQuarrie, "Monte Carlo investigation of single cell beta dosimetry for intraperitoneal radionuclide therapy," *Phys Med Biol* **49** (10), 1959-72 (2004).

<sup>41</sup>C. Kirkby and R. S. Sloboda, "Comprehensive Monte Carlo calculation of the point spread function for a commercial a-Si EPID," *Med Phys* **32** (4), 1115-1127 (2005).

<sup>42</sup>C. Kirkby and R. S. Sloboda, "Consequences of the spectral response of an a-Si EPID and implications for dosimetric calibration," *Med Phys* **32** (8), 2649-2658 (2005).

## Chapter 2: The Varian aS500 EPID

### 2.1 INTRODUCTION

As introduced briefly in the first chapter, the Varian aS500 EPID (Varian Oncology Systems, Palo Alto, CA) is a portal imaging device that uses an indirect detection scheme to generate an MV image. Its fundamental components consist of a copper plate, gadolinium oxysulfide scintillation screen, and an array of a-Si photodiodes and thin film transistors (TFTs). It originally appeared on the commercial market in 1999 and has since become widely available to cancer centers throughout the world. Three aS500 EPIDs are installed at our center (Cross Cancer Institute, Edmonton AB). In this chapter we will describe the components and properties of the detector, as well as the process of image formation.

### 2.2 DESCRIPTION OF THE VARIAN aS500 EPID

#### 2.2.1 *Overview of the EPID*

In figure 2.1 we present a cross sectional view of the aS500 EPID that shows the relative locations of the various components. For reference, radiation is incident from the top. At the heart of the EPID is a detection stack, sometimes referred to as a cassette<sup>1</sup>, that is made up of both primary image-forming components and supporting structures. The cassette consists of a protective sandwich comprised of circuit-board material and foam (top and bottom), a 1 mm thick copper plate, a 134 mg/cm<sup>2</sup> gadolinium oxysulfide scintillation screen (Kodak Lanex Fast Back, Eastman Kodak Company, Rochester, NY), an optical filter (Lee Filter, Lee Filters, Andover UK), and an a-Si flat-panel photodiode array deposited on a glass substrate followed by the

bottom layers of the protective sandwich. Exact details of the stack were provided by Varian through a non-disclosure agreement.<sup>2</sup> The details as described here are understood to be in the public domain<sup>1,3</sup>. Each pixel on the flat-panel consists of an a-Si photodiode and TFT. There are  $512 \times 385$  active pixels with a pitch of 0.784 mm making up the array. This results in an imaging area of  $\sim 40 \times 30 \text{ cm}^2$ .

Besides the sensitive elements in the detection cassette, additional components are subject to irradiation and cause scattering, and thus they need to be considered in this work. The EPID is protected with an epoxy fiberglass cover mounted on a shock absorption system that will trigger an operational interlock if the device is bumped. Further, it is housed in a contoured mold of similar material that makes up its back end and allows for cables to pass underneath the device. As indicated in figure 2.1 there are significant air gaps between the housing and the enclosed detection stack. A complex bracket assembly joins the EPID to a steel, mechanical R-arm that is used to move and hold the EPID in position. A motor used to translate the EPID on the R-arm is also present (not shown). The read-out electronics and gate drivers are kept out of direct exposure to the radiation beam during normal operation.

In typical dosimetric operation at our center (such as for IMRT verification), a plate of additional buildup material is added directly on top of the fiberglass cover as shown in the figure. Typically this is 0.5 or 2.0 cm of solid water for 6 and 15 MV beams, respectively. The additional buildup covers the entire area directly irradiated.

### 2.2.2 EPID Primary Components

From an operational point of view there are four primary components (or component subsystems) residing in the EPID.<sup>3</sup> Each plays a unique role in the formation of an MV image.

A 1 mm copper buildup plate is the first major component with which the incident radiation interacts. It serves three important purposes. First, it acts as a buildup layer to promote electronic equilibrium at the imaging plane. It generates Compton interactions (the principle interaction at typical external beam therapy energies<sup>4</sup>), thereby producing primary and secondary electrons that can migrate down to the phosphor and greatly increase the overall dose deposited per unit incident fluence. This results in an increase in the broad-area detective quantum efficiency,  $DQE(0)$ , but decreases the modulation transfer function,  $MTF$ .<sup>5</sup> Second, it preferentially attenuates lower energy photons, many of which may have arisen due to scatter. Reducing the contribution to the image from scattered radiation increases the contrast. Third, the copper plate blocks electrons generated in upstream components, also reducing unwanted contributions to the final image.

The purpose of the phosphor screen, the next primary component, is energy conversion. Incident particles (photons and electrons) excite bound electrons in the phosphor from the valence to the conduction band. Many of the excited electrons will return to the valence band through a local state created by small amounts of

impurities called activators and in the process emit light. For the gadolinium oxysulfide phosphor used in the aS500, the light is emitted with a primary wavelength of 545 nm (2.4 eV).<sup>6</sup> There is a substantial quantum gain at this step. There are approximately 60 optical photons created per keV of absorbed energy.<sup>6</sup> This means that if a typical 1 MeV photon manages to deposit all of its energy, about  $6 \times 10^4$  optical photons would be produced. A reflective foil is placed on top of the phosphor to ensure that the optical photons migrate down towards the flat panel array. There is also an optical filter between the phosphor and the photodiode layer that helps to reduce the glare from multiply scattered optical photons.

The amorphous silicon photodiodes integrate the light into an electrical signal. The aS500 EPID uses hydrogenated amorphous silicon (a-Si:H) n-i-p photodiodes that are only a few  $\mu\text{m}$  thick. These devices are fabricated via deposition and photolithic etching of layers of a-Si:H onto a glass substrate over a large area. Additional layers of dielectric insulators and conductive metals form the other electrical components and connections. At the core of the photodiode is an intrinsic layer of a-Si:H about 1-2  $\mu\text{m}$  thick. It is sandwiched between thinner layers of n- and p-doped microcrystalline silicon. A light photon absorbed by the a-Si:H moves an electron from its valence to its conduction band, creating a single electron-hole pair. An externally applied reverse bias voltage ( $\sim 5$  V) causes the charges to migrate towards the doped layers where the charge builds up.<sup>6</sup> In this sense, the device works much like a parallel plate capacitor.<sup>7</sup> The photodiode covers most of the pixel area ( $\sim 83\%$  fill factor) to collect as much light as possible.<sup>3</sup>

The final subsystem of components to consider is the readout electronics. Coupled with the photodiode is an a-Si:H thin film transistor (TFT).<sup>3</sup> Figure 2.2 shows a schematic diagram of a pixel and how it fits into the array. During irradiation a charge builds up across the intrinsic a-Si:H layer of the photodiode that is proportional to the exposure. During periods of no irradiation the gate drivers open up the TFTs on a row by row basis and the external charge preamplifiers collect the charge. An image frame is obtained when all rows have been read out.

### 2.2.3 *Image Acquisition*

Image acquisition is timed according to sync pulses generated by the linac control system, which are most conveniently considered in consecutive groups of six for Varian machines. Pulses intended to produce beam form a subset of each group of six sync pulses, their number and relative timing depending upon the chosen beam pulse repetition rate or a beam acquisition trigger. These pulses in turn drive the EPID sync generator (PVSYNC), which enables a series of rows making up an image frame to be read out between radiation beam pulses. The read-out rate is fixed at 10 Hz (default); thus, the maximum number of rows that can be read out between two beam pulses is governed by PVSYNC. For a pulse pattern corresponding to a beam delivery or rep rate of 300 MU/min at 6 MV, the number of rows read per pulse in IMRT imaging mode was set to 20 for the present work. The image acquisition processor (ACPU) can hold up to 64 frames in its memory, which is referred to as the frame buffer. This leads to a small dead time ( $\sim 0.28$ s) occurring every 64 frames



when the contents of the frame buffer are transferred to RAM memory, which can reduce the intensity of the final image when a continuous set of frames are acquired during beam delivery, and therefore may require correction.<sup>8</sup>

The aS500 EPID can be deployed at source-to-detector distances (SDDs) between 105 – 180 cm. At our center the standard deployment distance for calibration and IMRT verification is 145 cm. The detector can also be offset in the x- and y-directions by about 10 cm if desired. Images can be acquired in one of three modes: standard, high, and IMRT. In the standard and high modes a single image is taken beginning at a predefined time point during the irradiation. The difference between these modes is the number of frames that are averaged to obtain the final image – standard typically collects one frame whereas high collects 2-10. This parameter is, however, adjustable. In IMRT mode, frames are acquired continuously over the entire time the beam is on. The resulting image is then obtained as the average over all frames acquired (hence is an integrated image of the entire irradiation). Delivery of 30 MU at a rep rate of 300 MU/min at 6 MV results in an image averaged over approximately 120 frames.

Defective pixels are treated in the following manner. During EPID acceptance testing and commissioning a pixel defect map is generated by taking a pair of dark field (or no radiation) images where no pixel correction is applied. There is a fixed period of time between the acquisitions that allows for the leakage current to be integrated. Subtracting the two images then reveals the leakage present in each

pixel. This allows any defective pixels to be manually identified. For subsequent image acquisitions, pixels identified as defective are assigned a value that is obtained by interpolation from their four nearest neighbors.

#### 2.2.4 Image Calibration

Image calibration requires the acquisition of two different images – a dark field image,  $DF(x,y)$ , and a flood field image,  $FF(x,y)$ . These must be acquired separately for each acquisition mode. The manufacturer recommends that they be updated on a regular basis (every two weeks).<sup>3</sup> The DF image is acquired in the absence of radiation and is therefore independent of the linac on which the EPID is mounted. It is meant to correct for any imperfections in the detector array as well as variations in electrometer offsets. Multiple frames are acquired in quick succession ( $\sim 6.7$  frames per second) and then averaged to minimize image noise. An example DF image is shown in figure 2.3. The FF image is acquired by irradiating the entire imaging area (all pixels) without an object in the radiation field. It is used to correct for variations in pixel sensitivity as well as to improve image quality by smoothing out field inhomogeneities. Like the DF image it is obtained from image frames measured several times in quick succession and averaged to reduce noise. A FF image reflects radiation field inhomogeneity, individual pixel sensitivities and electrometer gains. An example FF image is shown in figure 2.4.

An acquired image  $I(x,y)$  is routinely and automatically obtained from a raw EPID image  $I_{raw}(x,y)$  using the correction scheme

$$I(x,y) = \frac{I(x,y)_{raw} - DF(x,y)}{FF(x,y) - DF(x,y)} k_{FFmean} \quad (2.1)$$

Here  $k_{FFmean}$  is the mean value of all the FF pixels, and pixel value units are averaged across all frames taken for each of the raw, dark, and flood field images, respectively. In general, this technique has the effect of removing pixel contributions from the dark field as well as flattening the image and normalizing out individual pixel sensitivities, operations appropriate for clinical imaging. However this correction scheme, particularly dividing by the FF, has some implications when the EPID is used for fluence measurement, which will be discussed in chapter 4. A sample image of a  $10 \times 10 \text{ cm}^2$  field (defined at the EPID's imaging plane) is shown in figure 2.5.

### 2.3 COMPREHENSIVE MODEL OF THE EPID

Monte Carlo simulations were used to model both the transport of ionizing and optical radiation through the EPID at different stages of this work. The Monte Carlo codes used for these simulations are discussed in detail in chapter 3. Here, it is relevant to conclude our overview of the asS500 EPID with a discussion of how its various components were incorporated into the Monte Carlo simulations. Other authors have presented a-Si EPID models used in Monte Carlo work<sup>1,9-14</sup> and these models vary considerably in the level of detail incorporated. Schach von Wittenau *et al.*<sup>10</sup> argued that the various nondetector portions of a flat-panel detector system (such as the covers or supporting structures) cause significant image degradation due to their contribution to the scattered radiation that delivers dose to the phosphor. Hence,

at the outset of the present work, it became clear that if we wanted to obtain an accurate blur kernel for the aS500 and distinguish the relative contributions to it from various detector components, it would be necessary to make the detector model as complete as possible. As mentioned earlier, the EPID manufacturer provided us with the technical details of this detector, and based on this information we were able to develop a comprehensive model that incorporated 18 different layers.

### 2.3.1 Assumptions in the Radiation Transport Model

We simplified the model somewhat by assuming that the detector was a symmetric stack of materials with overall dimensions  $40 \times 30 \times 9 \text{ cm}^3$ . This has one obvious implication in that any potential effects arising from asymmetrical structures such as the R-arm mounting brackets, cables, or drive motors were not accounted for. Therefore a blur kernel derived from a pencil beam incident on our model of the EPID would be inherently symmetric and spatially invariant.

Additional solid water (2.5 cm thick in most cases) was modeled in intimate contact with the bottom of the detector to approximate the backscatter contribution from the underlying mechanical structures. A thickness of 2.5 cm was chosen to be consistent with other work available at the outset of the present study.<sup>9,11</sup> A more recent investigation by Siebers *et. al.*<sup>1</sup> suggests that 1.0 cm of water placed 2.1 cm behind the detector is sufficient to model the backscatter.

EGSnrc (discussed in chapter 3) is a standard Monte Carlo code that simulates the transport of ionizing radiation with specific emphasis on medical physics problems.<sup>15,16</sup> For the EGSnrc simulations it was necessary to define the material composition of each layer present. For the primary or simple materials such as copper, air, or gadolinium oxysulfide the exact chemical compositions are well known,<sup>17</sup> but some of the other materials were approximated as mixtures (rather than specific compounds). For example the properties of the printed circuit board material FR4, a glass fiber epoxy laminate, were estimated as follows. FR4 is generally composed of multiple layers of 7628 fibreglass that are impregnated with an epoxy resin.<sup>18</sup> We estimated an overall density of  $1.35 \text{ g/cm}^3$  based on a density of  $\sim 1.05 \text{ g/cm}^3$  for the fibreglass<sup>18</sup> and  $\sim 1.80 \text{ g/cm}^3$  for epoxy resin<sup>19</sup>, which were assumed to be combined in a 60:40 ratio, respectively.<sup>18</sup> We assumed the fibreglass to have approximately the same chemical composition as alkali borosilicate.<sup>17</sup> The chemical composition of the epoxy resin was determined from the information listed online at the Macrogalleria.<sup>20</sup> The amount of each element in a given mixture was determined by the relative atomic weight. For FR4, this information is listed in Table 2.1. Modelling some of the EPID materials as mixtures introduces another uncertainty inasmuch as the effects of chemical bonds between the constituent elements on the average ionisation energy are not accounted for. However, since the contributions to the overall detector response from materials such as FR4 are presumed to be relatively small, which we infer from the work of Schach von Wittenau *et al.*<sup>10</sup> and their low relative areal densities, gross estimates of their composition should be sufficient for our purposes.

### 2.3.2 *The Optical Model*

The Monte Carlo code DETECT2000 is designed to model the propagation of optical photons through various media, simulating scattering and absorption events.<sup>21</sup> It required three parameters to describe each different medium: 1) the scattering coefficient, 2) the absorption coefficient, and 3) the index of refraction. In addition, the boundaries of each material had to be described as one of six surface types defining the transmission and reflection properties at that surface. For the phosphor, these parameters were chosen to be consistent with information provided by Kodak<sup>22</sup> (Eastman Kodak, Rochester NY), the screen's manufacturer.

Modeling the optical filter required some assumptions. This filter was designed to reduce the amount of light passing through it without altering its colour, and was originally intended for photographic, theatre, television and film set applications. Therefore it was assumed that absorption, rather than scatter, was the dominant interaction mechanism within it. The filter has an overall optical transmission of about 25% with a transmission of about 22% for photons of 545 nm wavelength (Lee Filters, Andover UK).

There is also a polyester reflector present on the upstream surface of the phosphor. At the 545 nm wavelength, it has a reflectivity of 0.88.<sup>22</sup> Rather than model the polyester, we defined the upper phosphor surface as having a reflection coefficient of 0.88. The boundary between the phosphor and the filter was assumed to be a polished surface where boundary crossing is dictated by Fresnel reflection and

Snell's law of refraction. We assumed that the remaining five surfaces of the phosphor (including the lower surface) were ground surfaces (as such the normal to the surface in the refraction calculations follows a Lambertian distribution<sup>21</sup>).

Immediately downstream from the optical filter is the photodiode array, which is deposited on a glass substrate. The optical portion of the detector stack is surrounded by black paper, which prevents any outside light from entering, and absorbs any light that exits the constituent layers. Optical backscatter from the glass substrate was assumed to be negligible. Table 2.2 provides a summary of the parameters used in the optical model.

## 2.4 SUMMARY

This chapter describes the composition and operating principles of the aS500 EPID. With an understanding of the indirect detection scheme the EPID uses to generate an MV image, along with information provided by the manufacturer, we were able to develop a comprehensive model of it for the purposes of simulating ionizing radiation transport and dose deposition, and optical photon transport. Implicit within this model are a few simplifying assumptions that should not, for our purposes, impact greatly on the simulation results. We are now poised to examine the specific Monte Carlo methods used to simulate the transport of both ionizing and optical radiation through this detector, so that we can subsequently investigate particular problems which arise when using the EPID for portal dosimetry.

Element	Relative Weight
C	0.304
H	0.028
O	0.391
Si	0.226
B	0.024
Na	0.017
Al	0.007
K	0.002

**Table 2.1.** The relative weights of the elements used in the FR4 model mixture.

Material	Scatter M.F.P. (cm)	Absorption M.F.P. (cm)	Index of refraction
Scintillation Screen $Gd_2O_2S:Tb$	0.0017	10	2.6
Optical Filter	10	0.005	1.6

**Table 2.2.** The parameters used in DETECT2000 to model the optical photon transport. Kodak<sup>22</sup> provided a scatter MFP between 10 and 25  $\mu m$  and an absorption MFP of greater than 10 cm. For comparison, Kausch et al.<sup>14</sup> used a scatter MFP of 25  $\mu m$ , an absorption MFP of 4 cm, and an index of refraction of 2.4 in a different transport code, and did not model the optical filter.



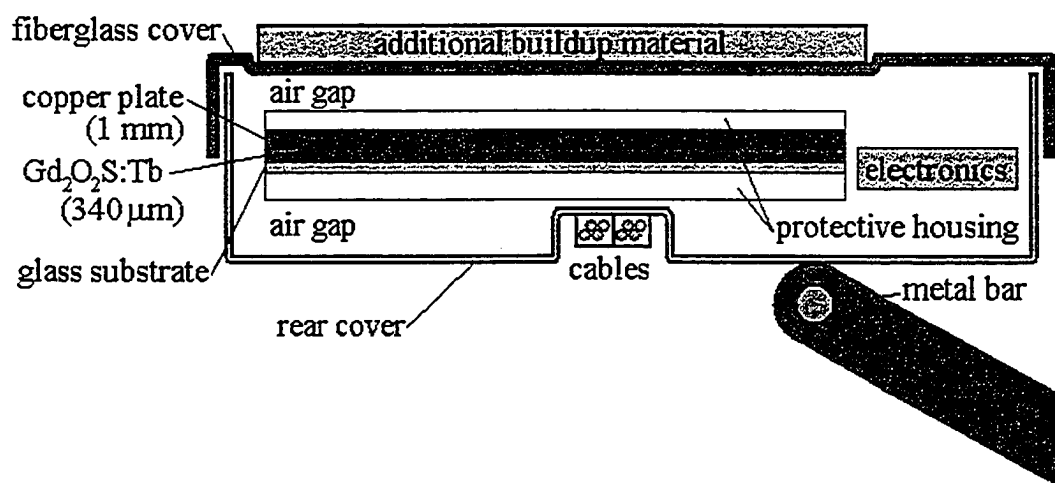


**Figure 2.1.** A cross section view of the aS500 EPID (not to scale). This view shows the relative locations of the various components of the detector. The image detection stack in the center consists of the materials indicated as well as numerous support structures (such as foam, epoxy, and paper.) The additional buildup material shown is typically solid water, and is added to the detector to enhance buildup for dosimetry applications.

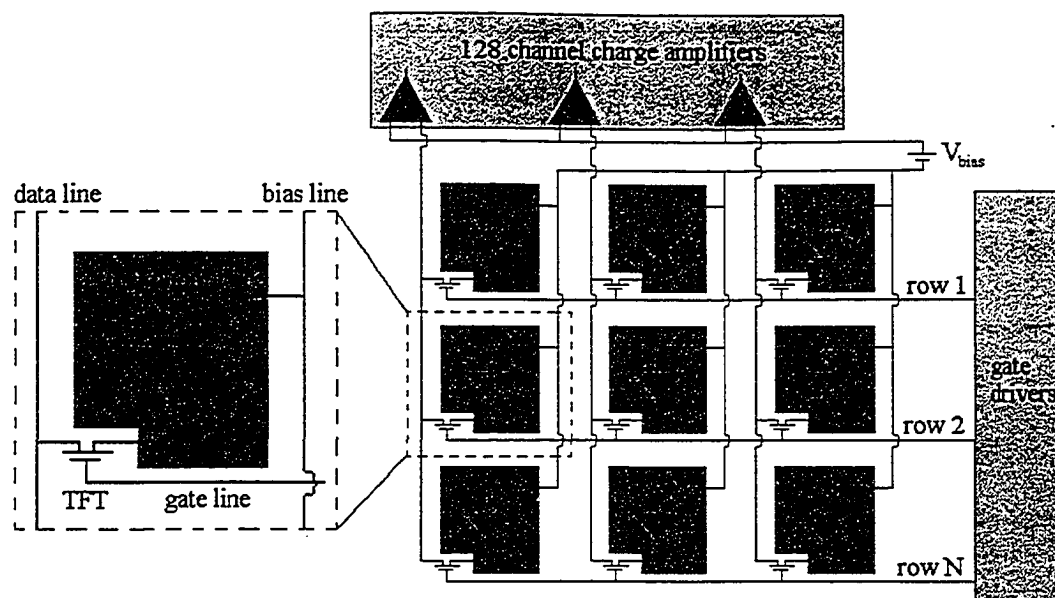


**Figure 2.2.** A schematic diagram of a typical pixel and how it is connected to the readout electronics. Optical photons absorbed by the amorphous silicon move electrons into the conduction band, from where an externally applied reverse bias voltage causes the charges to migrate towards the n- and p-doped layers above and below, effectively making the device behave like a capacitor.<sup>7</sup> During periods of no irradiation the gate drivers open up the TFTs on a row by row basis allowing the external charge preamplifiers to collect the charge. An image frame consists of a readout of all rows.

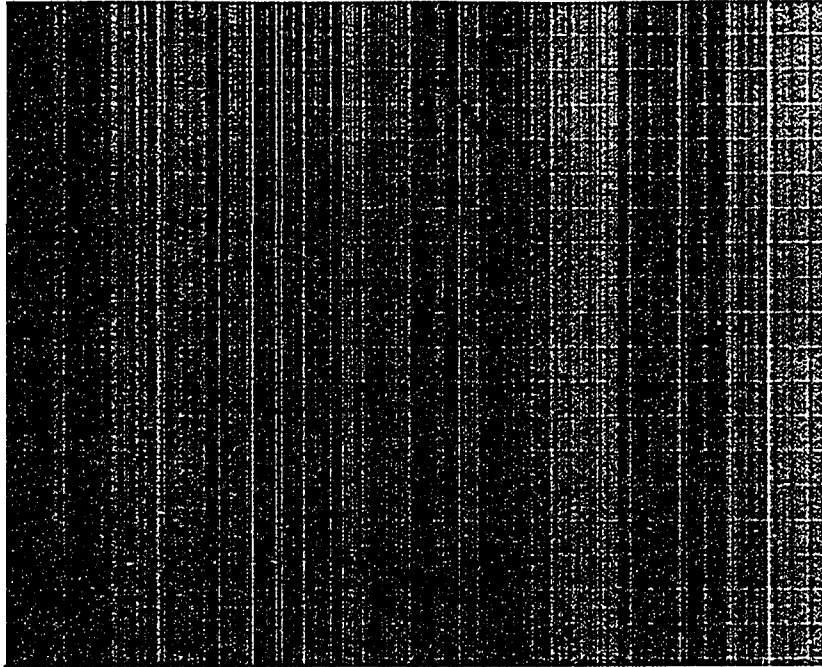


**Figure 2.3.** A sample dark field image. Approximately 60 frames were acquired with the beam off. This image reflects non-uniformities in the detector array (due to the manufacturing process and possible damage) and variations in electrometer offsets.

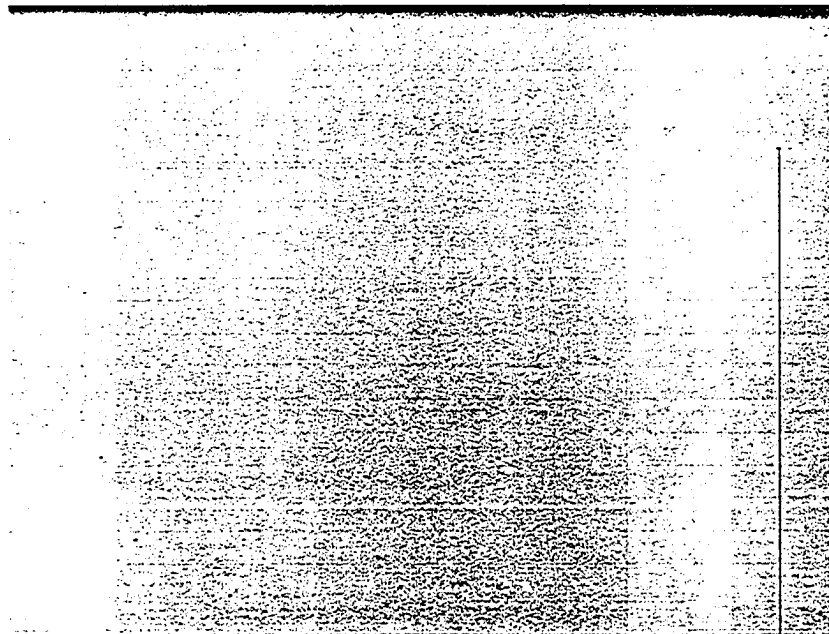


**Figure 2.4.** A sample flood field image. Approximately 30 frames were acquired with the EPID deployed at 140 cm SDD [6 MV, 300 MU/min, IMRT scan mode]. The image reflects radiation field inhomogeneity, individual pixel sensitivities and electrometer gains.

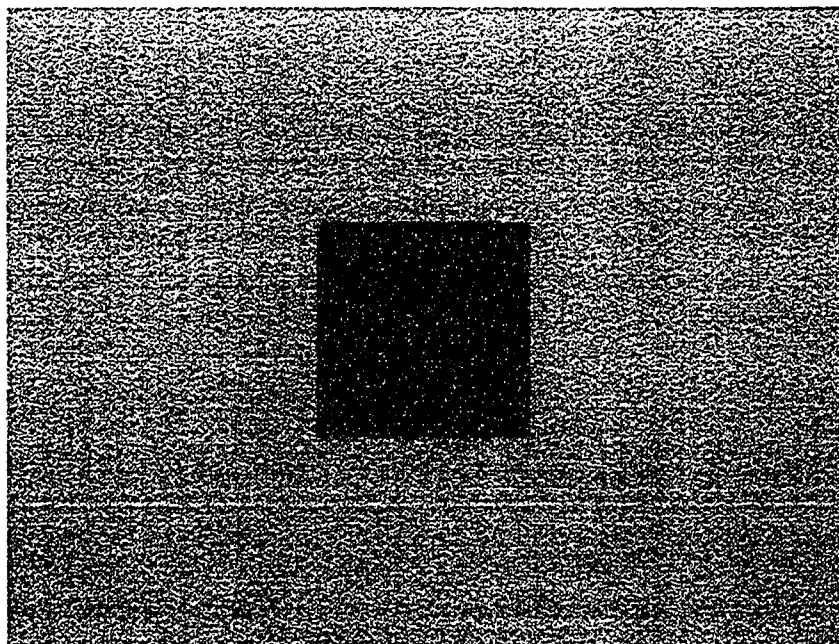


**Figure 2.5.** A sample image of a  $10 \times 10 \text{ cm}^2$  field (defined at the imaging plane) with the EPID deployed at 140 cm SDD [6 MV, 300 MU/min, IMRT scan mode].

The correction scheme defined by Eq. 2.1 has been applied.

## 2.5 REFERENCES

- <sup>1</sup>J. V. Siebers, J. O. Kim, L. Ko, P. J. Keall, and R. Mohan, "Monte Carlo computation of dosimetric amorphous silicon electronic portal images," *Med Phys* **31** (7), 2135-46 (2004).
- <sup>2</sup>W. Wong (personal communication from Varian Medical Systems).
- <sup>3</sup>Varian Medical Systems, *Portal Vision aS500 Rel.6 Reference Manual* (Varian Medical Systems Inc., Palo Alto, CA, 2000).
- <sup>4</sup>H. E. Johns and J. R. Cunningham, *The Physics of Radiology 4th ed.* (Springfield: Charles C. Thomas, Springfield, IL, 1983).
- <sup>5</sup>M. Lachaine, E. Fourkal, and B. G. Fallone, "Investigation into the physical characteristics of active matrix flat panel imagers for radiotherapy," *Med Phys* **28** (8), 1689-95 (2001).
- <sup>6</sup>J. A. Rowlands and J. Yorkston, "Flat Panel Detectors for Digital Radiography," in *Handbook of Medical Imaging* (SPIE Press, Bellingham WA, 2000), pp. 223 - 328.
- <sup>7</sup>L. E. Antonuk, K. W. Jee, Y. El-Mohri, M. Maolinbay, S. Nassif, X. Rong, Q. Zhao, J. H. Siewerdsen, R. A. Street, and K. S. Shah, "Strategies to improve the signal and noise performance of active matrix, flat-panel imagers for diagnostic x-ray applications," *Med Phys* **27** (2), 289-306 (2000).
- <sup>8</sup>P. B. Greer and C. C. Popescu, "Dosimetric properties of an amorphous silicon electronic portal imaging device for verification of dynamic intensity modulated radiation therapy," *Med Phys* **30** (7), 1618-27 (2003).
- <sup>9</sup>B. Warkentin, S. Steciw, S. Rathee, and B. G. Fallone, "Dosimetric IMRT verification with a flat-panel EPID," *Med Phys* **30** (12), 3143-55 (2003).
- <sup>10</sup>A. E. Schach von Wittenau, C. M. Logan, M. B. Aufderheide, 3rd, and D. M. Slone, "Blurring artifacts in megavoltage radiography with a flat-panel imaging system: comparison of Monte Carlo simulations with measurements," *Med Phys* **29** (11), 2559-70 (2002).
- <sup>11</sup>J. O. Kim, J. V. Siebers, P. J. Keall, and R. Mohan, "A Monte Carlo model of an amorphous silicon flat panel imager for portal dose prediction," in *EPI2K2 Program & Abstract Book* (7th International Workshop on Electronic Portal Imaging, Vancouver BC, 2002), pp. 118-119.
- <sup>12</sup>B. M. McCurdy, K. Luchka, and S. Pistorius, "Dosimetric investigation and portal dose image prediction using an amorphous silicon electronic portal imaging device," *Med Phys* **28** (6), 911-24 (2001).

- <sup>13</sup>D. A. Jaffray, J. J. Battista, A. Fenster, and P. Munro, "Monte Carlo studies of x-ray energy absorption and quantum noise in megavoltage transmission radiography," *Med Phys* **22** (7), 1077-88 (1995).
- <sup>14</sup>C. Kausch, B. Schreiber, F. Kreuder, R. Schmidt, and O. Dossel, "Monte Carlo simulations of the imaging performance of metal plate/phosphor screens used in radiotherapy," *Med Phys* **26** (10), 2113-24 (1999).
- <sup>15</sup>I. Kawrakow, "Accurate condensed history Monte Carlo simulation of electron transport. I. EGSnrc, the new EGS4 version," *Med Phys* **27** (3), 485-98 (2000).
- <sup>16</sup>I. Kawrakow and D.W.O. Rogers, *The EGSnrc Code System: Monte Carlo Simulation of Electron and Photon Transport Report No. PIRS-701*, 2002.
- <sup>17</sup>M. J. Berger, J. S. Coursey, and D. S. Zucker, *ESTAR, PSTAR, and ASTAR: Computer Programs for Calculating Stopping-Power and Range Tables for Electrons, Protons, and Helium Ions (version 1.2.2)*. [Online] Available: <http://physics.nist.gov/Star> [2005, February 7] (National Institute of Standards and Technology, Gaithersburg, MD, 2005).
- <sup>18</sup>Fels Company, "The PCB Laminate FAQ," (Fels Company, [http://www.felsweb.com/lam\\_faq.htm](http://www.felsweb.com/lam_faq.htm), 2001).
- <sup>19</sup>PlasticsUSA, "Specific Gravity of Major Polymers," (Eastpoint-Oltean, <http://www.plasticsusa.com/specgrav2.html>, 2003).
- <sup>20</sup>Polymer Learning Center, "Epoxy Resins (Macrogalleria)," (University of Southern Mississippi, Dept. of Polymer Science, <http://www.pslc.ws/mactest/level2.htm>, 2002).
- <sup>21</sup>C. Moisan, F. Cayouet, and G. McDonald, *DETECT2000 A Program for Modeling Optical Properties of Scintillators* (Dept. of Electrical and Computer Engineering, Laval University, Quebec City, QC, 2000).
- <sup>22</sup>D. J. Steklenski (personal communication from Health Imaging, Eastman Kodak).

## Chapter 3: Monte Carlo Method and Simulation Codes

### 3.1 INTRODUCTION TO THE MONTE CARLO METHOD

The Monte Carlo method was developed shortly following World War II and is largely credited to the Polish born mathematician Stanislaw Ulam who first came up with the approach while playing a game of solitaire.<sup>1</sup> As introduced in chapter 1, the fundamental idea behind the method is to employ statistical sampling that describes microscopic processes in order to obtain approximate solutions to quantitative problems concerning the behavior of macroscopic systems. As such, the Monte Carlo method offers an efficient alternative to deterministic or analytic solutions for problems with a high degree of complexity. In the present work we are concerned with the transport of both ionizing (10 keV – 20 MeV photons and electrons) and non-ionizing (optical photons) radiation through layered media where the physics describing the various interactions that take place are well known. The coupled integro-differential equations that describe the electromagnetic shower development lend themselves to a deterministic solution only under severe approximations. Over any energy range of interest to us, the Monte Carlo technique appears to be the best known solution method that can be applied.<sup>2-4</sup>

We consider the problem of photon transport through a given medium to illustrate the Monte Carlo approach to radiation transport.<sup>5</sup> The distance to an interaction site is described by the well-known probability distribution function

$$p(z) dz = \mu e^{-\mu z} dz, \quad (3.1)$$



where  $z$  is the distance to the next interaction and is valid on the range  $0 \leq z \leq \infty$ , and  $\mu$  is the interaction coefficient (a function of the particle's energy and of the medium). A cumulative distribution function  $c(z)$  can then be defined as

$$c(z) = \int_0^z p(z') dz' = 1 - e^{-\mu z}. \quad (3.2)$$

By its definition, the cumulative distribution function can be mapped onto a range of random variables  $r$ , where  $0 \leq r \leq 1$ , and  $r$  is uniformly distributed. Hence

$$r = c(z) = 1 - e^{-\mu z}. \quad (3.3)$$

Thus a sample of interaction distances,  $z$ , that have the distribution described in Eq. 3.1 can be generated from a uniformly distributed set of random numbers by inverting Eq. 3.3.

$$z = \frac{-1}{\mu} \ln(1 - r). \quad (3.4)$$

In this way, we can make use of an available random number generator to simulate the fate of individual photons released in the medium. Random number generators (RNGs) effectively generate a sequence of pseudorandom numbers with a uniform distribution based on a given seed number. For Monte Carlo investigations it is desirable to have an RNG that is portable (ie. produce the same sequence on different machines) and is able to produce a random sequence independent from other sequences (so as to avoid correlations in the results of parallel operations).

RANLUX,<sup>6,7</sup> the RNG used in EGSnrc, possesses these features and has a period  $> 10^{165}$ . An initial photon's fate, including the fates of all subsequently generated daughter particles, across the duration of the simulation, is commonly referred to as a "history." Averaging over a given set of histories can then provide an approximation

to quantities of interest (such as photon fluence through a given area). Each particle history corresponds to one point in a multi-dimensional space (with the dimensionality depending on the number of interactions), hence the averaging procedure corresponds to a multi-dimensional Monte Carlo integration,<sup>2</sup> and thus is subject to some statistical uncertainty depending on the number of histories simulated ( $N$ ). Usually the uncertainty decreases as  $N^{-1/2}$  (Eq. 1.8).<sup>3,4</sup>

## 3.2 OVERVIEW AND BENCHMARKING OF EGSNRC

### 3.2.1 *Introduction to EGSnrc*

The software package used for Monte Carlo simulation of ionizing radiation transport in the problems described herein was EGSnrc V3.<sup>2,8</sup> The roots of this software can be traced back to the early 1960s when the first electromagnetic cascade codes began to emerge to assist in the simulation of high-energy ( $> 1$  GeV) nuclear physics experiments. EGS (electron gamma shower) was initially developed at the Stanford Linear Accelerator Center (SLAC) in the 1970's where it was used for shower detector design. A shower refers to the cascade of individual particle paths in an interacting medium that directly result from (and include that of) a single incident particle.<sup>2</sup> Over the ensuing years the code passed through several incarnations, gaining popularity for medical physics applications in the late 1980s when EGS4 was released with the ability to track showers down to much lower energies. Towards the end of the 1990s the EGS code system found a new home at the National Research Council of Canada, and the first version of EGSnrc was released in the summer of

2000. EGSnrc was fitted with a completely new electron transport algorithm that eliminated the known shortcomings of its predecessor, the PRESTA algorithm. EGSnrcV3 is now capable of simulating coupled photon and electron transport down to energies of 10 keV, which in water translates to micrometer scale resolution (2.5  $\mu\text{m}$  based on continuous slowing down approximation (CSDA) range<sup>9</sup>).

In overview, the EGSnrc system simulates the transport of photons, electrons and positrons through specifically defined media and allows one to tabulate radiological quantities of interest such as the energy deposited in specifically defined regions. Hence it allows for the simulation and estimation of such quantities as particle fluence and dose per particle history. The calculations are a faithful simulation of physical reality.<sup>2</sup> Initially, particles are born into phase-space distributions that reflect the radiation source being simulated. Each particle then travels a given distance as determined by a probability distribution function based on the particle's total interaction cross section. At an interaction site, each particle then adopts a new energy and direction based on the differential cross section corresponding to the specific interaction that takes place, which is obtained by sampling a probability of occurrence distribution. Additional particles produced at the site of an interaction are also transported. This process continues in a step-wise fashion until all the particles deposit all of their energy in the defined media, or leave the geometry under consideration. Quantities of interest are then calculated by averaging the results over  $N$  histories and, as mentioned above, are subject to statistical uncertainties that usually decrease as  $N^{-1/2}$ .

Four basic processes are modeled for the interactions of photons (described as neutral particles) with surrounding media: pair and triplet production, incoherent (Compton) scattering, photo-electric absorption, and coherent (Rayleigh) scattering. The algorithm followed has four steps. First, the distance to the next interaction is determined (process outlined in Eq's. 3.1-3.4). Second, the particle is transported in a straight line, accounting for geometrical constraints, to the site of the interaction. Third, the specific interaction type is determined randomly, based on its relative contribution to the total cross section. Finally, the particle is issued a new energy and direction based on the differential cross section for the interaction selected. Further, newly energized daughter particles are added to the simulation to also be transported.

A condensed history algorithm<sup>10</sup> is used for the charged particle transport. If we consider that a fast moving electron ( $\sim 1$  MeV) undergoes approximately  $10^6$  interactions before local absorption and that typical simulations require at least  $10^6$  histories for decent statistical accuracy, that would result in the simulation of  $10^{12}$  individual interactions.<sup>2,10</sup> Although the speed of modern computers is rapidly advancing, at present, such simulations would typically take several days to complete.<sup>2</sup> Thus event-by-event simulation of charged particle interactions is not very practical. In the condensed history approach, the cumulative effects of elastic and inelastic collisions that occur over a transport step are accounted for by sampling energy and direction changes from appropriate multiple scattering distributions.

EGSnrc uses a class II condensed history algorithm<sup>2,5,10</sup> in which collisions with small energy losses are grouped, but the rarer collisions where larger amounts of energy are lost (“catastrophic” collisions) are treated individually. Catastrophic events include hard bremsstrahlung (energy threshold AP), hard inelastic collisions (energy threshold AE), and annihilation events. Soft bremsstrahlung emissions are accounted for using the restricted radiative stopping power (assumed constant over a transport step). Similarly soft inelastic collisions deposit energy based on the restricted collisional stopping power (which is again assumed to be constant.) Elastic scattering is accounted for using differential cross sections derived from multiple scattering theory.<sup>2</sup> The overall algorithm followed for the transport of charged particles is similar to that for neutral particles. First the distance to the next catastrophic interaction is determined. The charged particle is then transported, but energy is lost continuously as determined by the stopping powers. Further, multiple elastic scattering is accounted for such that some of this energy may be deposited in regions not on the linear transport path of the particle. In the vicinity of media boundaries (defined by default as being within 3 elastic mean free path lengths) event-by-event interactions are individually simulated. Finally, at the site of a catastrophic event, the specific interaction is determined and the charged particle’s energy and direction are altered accordingly.

EGSnrc is distributed with multiple user codes, some of which were also employed in this work. These codes enable the user to more quickly encode some of the more common geometries encountered in medical physics simulations. User

codes employed in this work were DOSXYZnrc and DOSRZnrc,<sup>11</sup> which correspond to Cartesian and cylindrical coordinate geometries, respectively.

### 3.2.2 Benchmarking

The EGSnrc software and the techniques it employs have been benchmarked extensively.<sup>2,8,12,13</sup> We chose to study a supplemental series of simple problems for which analytic solutions are available, in order to test the accuracy of EGSnrc in simulating radiation transport through very thin layers of material such as are found in the aS500 EPID. This section is not intended to be an exhaustive investigation of the ability of EGSnrc to simulate reality. Here, we confine our attention to examining the absorbed dose to a thin foil as outlined by Attix.<sup>14</sup>

The problem considers a monoenergetic (kinetic energy  $T$ ) beam of electrons perpendicularly incident on a very thin foil with a fluence  $\Phi$  (particles/cm<sup>2</sup>). The thin foil allows for the following assumptions to be made: a) that the collisional stopping power remains relatively constant as the electron traverses the foil, and b) that the majority of bremsstrahlung photons generated inside the foil will escape without depositing energy. At such thicknesses, the  $\delta$  rays produced in the foil will carry a non-negligible amount of energy out of the foil. To a first approximation then, the dose to the foil will be proportional to the restricted collisional stopping power  $(dT/\rho dx)_\Delta$ . Here  $\Delta$  is defined as the kinetic energy of  $\delta$  rays that will escape the foil.  $\Delta$  is chosen based on the energy of an electron with a continuous slowing down

approximation (CSDA) range equal to the foil thickness. To first order, the dose to the foil is then

$$D = 1.602 \times 10^{-10} \Phi \left( \frac{dT}{\rho dx} \right)_{\Delta} \text{ [Gy]}. \quad (3.5)$$

The restricted collisional stopping power can be obtained from the expression<sup>15</sup>

$$\left( \frac{dT}{\rho dx} \right)_{\Delta} (T, \Delta) = \frac{2\pi r_0^2 m_0 c^2 n_e}{\beta^2} \left[ \ln \left( \frac{T^2}{I^2} \right) + \ln \left( 1 + \frac{\tau}{2} \right) + G^-(\tau, \eta) - \delta \right], \quad (3.6)$$

where  $\beta$  is the electron velocity in light speed units,  $r_0$  is the classical radius of the electron,  $m_0 c^2$  is the electron's rest mass energy,  $n_e$  is the electron density,  $I$  is the mean ionization energy,  $\tau = T / m_0 c^2$ ,  $\eta = \Delta / T$ ,  $\delta$  is the density effect parameter, and for electrons

$$G^-(\tau, \eta) = -1 - \beta^2 + \ln[4(1-\eta)\eta] + \frac{1}{1-\eta} + (1-\beta^2) \left[ \frac{\tau^2 \eta^2}{2} + (2\tau+1) \ln(1-\eta) \right]. \quad (3.7)$$

Higher order corrections to the simple analytic dose estimate of Eq. (3.5) can be obtained if one considers that: (i)  $\delta$  rays with kinetic energy  $> \Delta$  (*ie.* those that escape the foil) will likely also deposit some energy, and (ii) elastic scattering will lengthen the overall path length of each incident electron traversing the foil.

To estimate the energy deposited by escaping  $\delta$  rays requires that we determine the number of such species. The Moller electron scattering cross section can be obtained by integrating the differential cross section

$$\frac{d\sigma_M^-}{dT'} = \frac{2\pi r_0^2 m_0 c^2}{\beta^2} \frac{1}{T'^2} \left[ 1 + \frac{T'^2}{(T-T')^2} + \frac{\tau^2}{(\tau+1)^2} \left( \frac{T'}{T} \right)^2 - \frac{2\tau+1}{(\tau+1)^2} \frac{T'}{T-T'} \right], \quad (3.8)$$

for all  $\delta$  rays with energy greater than  $\Delta$ . Thus

$$\begin{aligned}\sigma_M^- &= \int_{\Delta}^{T/2} \frac{d\sigma_M^-}{dT'} dT' \\ &= \frac{2\pi r_0^2 m_0 c^2}{\beta^2} \left[ \frac{1}{\Delta} + \frac{1}{T-\Delta} + \frac{\tau^2}{(\tau+1)^2} \frac{1}{T^2} \left( \frac{T}{2} - \Delta \right) - \frac{2\tau+1}{(\tau+1)^2} \ln \left( \frac{T-\Delta}{\Delta} \right) \right]\end{aligned}\quad (3.9)$$

The number  $N_{\delta/e}$  of such  $\delta$  rays produced per incident electron is then

$$N_{\delta/e} = \frac{\sigma_M^- \rho t Z N_A}{A}, \quad (3.10)$$

where  $\rho$  is the foil density,  $t$  is its thickness,  $Z$  is the atomic number,  $N_A$  is Avagadro's number ( $6.022\text{E}+23$  atoms/mol) and  $A$  is the atomic mass (in g/mol). On average each of these electrons will travel through half of the foil thickness. Under the assumption that  $\sigma_M^- \propto 1/T_{\delta}^2$ ,  $T_{\delta}$  being the kinetic energy of the  $\delta$  ray, the average kinetic energy is

$$\langle T_{\delta} \rangle = \frac{T_{\delta} \Delta \ln \left( \frac{T_{\delta}}{2\Delta} \right)}{T_{\delta} - 2\Delta}. \quad (3.11)$$

Using this energy, we can calculate a secondary restricted collisional stopping power,  $(dT_{\delta}/\rho dx)_{\Delta}$  for these  $\delta$  rays. Then, using Eq. 3.5 we can determine their dose contribution.

For thin foils, Lewis<sup>16</sup> predicts an increase in path length due to elastic scattering of

$$t' = -\frac{\ln(1-t \cdot k_1)}{k_1}, \quad (3.12)$$



where  $k_1$  is the first elastic scattering moment. This can be approximated as roughly one half of the mass angular scattering power of the medium,<sup>17</sup> or

$$k_1 \approx \frac{1}{2} \frac{\langle \theta^2 \rangle}{\rho l}, \quad (3.13)$$

which describes the scattering of electrons traveling path length  $l$ .  $\langle \theta^2 \rangle$  is the mean square scattering angle. For the case of low electron energy and small relative atomic mass, the mass angular scattering power can be calculated as

$$\frac{\langle \theta^2 \rangle}{\rho l} = 16\pi N_A \frac{Z^2}{A} r_0^2 \left( \frac{m_0 c^2}{\beta pc} \right)^2 \ln \left( \frac{137 pc}{Z^{1/3} m_0 c^2} \right)^{1/2}, \quad (3.14)$$

with  $pc$  being the electron momentum multiplied by the speed of light.<sup>15</sup> The resulting total dose obtained from the first and second approximations can then be multiplied by the path length correction  $t'/t$  to give a final estimate of dose.

For a primary test case we chose to consider a monoenergetic ( $T = 1.0$  MeV) fluence of electrons ( $\Phi = 10^6$  e<sup>-</sup>/cm<sup>2</sup>) incident on a thin ( $t = 0.001$  cm) Cu ( $Z = 29$ ,  $A = 63.55$  g/mol,  $\rho = 8.96$  g/cm<sup>3</sup>,  $I = 322$  eV,  $\delta(1 \text{ MeV}) = 0.5799$ ) foil. The EGSnrc simulation scored the dose per history inside a  $1 \times 1$  cm<sup>2</sup> region on the foil irradiated by a beam of electrons of the same dimensions (effects due to lateral spreading were assumed negligible as irradiation by a  $2 \times 2$  cm<sup>2</sup> beam resulted in a negligible dose difference). The resulting foil dose in the simulation was  $D_{\text{EGS}} = 1.8038 \pm 0.0007$  Gy. To first order, the outlined analysis predicts a dose of  $D_1 = 1.7501$  Gy, which is already within 3 % of the EGS result. Absorbed energy from escaping  $\delta$  rays are estimated to add  $D_\delta = 0.0173$  Gy, bringing the analytic estimate to within 2 %.

Incorporating the effects of elastic scattering brings the final dose estimate to  $D_{ana} = 1.8132$  Gy. This is within 0.5 % of the EGSnrc result. Table 3.1 summarizes the results for this and some additional tests.

As shown, we investigated a range of materials and thicknesses. As thickness increases, the assumptions inherent in the analytical prediction break down and the discrepancy with the Monte Carlo result increases. Elemental gadolinium was chosen to represent a high Z material and because it is present in the phosphor screen of the portal imager. Water was chosen because it is a material of fundamental interest for dosimetric investigations. Because water is a compound, its restricted collisional stopping powers were derived from ICRU Report 37<sup>15</sup> and the NIST tables<sup>9</sup> rather than direct calculation of Eq. 3.6. It is important to note here that the CSDA range of an electron with  $T = 0.01$  MeV (the default value of ECUT in EGSnrc) is  $2.5\mu\text{m}$  in water. For a foil of this thickness, the difference between the simulation and analytical prediction was 0.1 %.

### **3.3 SINGLE CELL BETA DOSIMETRY**

#### *3.3.1 Introduction*

Monte Carlo simulation provides a valuable tool for understanding radiation transport in relation to a vast range of dosimetry problems. With the successful benchmarking of the code for very thin foils of water, there was some interest in our

center to use EGSnrc to investigate a nuclear medicine application. The problem was to determine the single event spectra for beta-emitting sources used in intraperitoneal radionuclide therapy – a treatment modality employed to slow the progress of cancers that have metastasized to the peritoneal cavity. Here we outline how this problem was set up and solved using EGSnrc.<sup>18</sup>

A single event spectrum,  $f_1(z)$ , is the distribution of specific energy,  $z$  (microdosimetric equivalent of absorbed dose), produced by the traversal of a target volume by individual particles.<sup>19</sup> Specifically, we determined single event spectra for five therapeutic radionuclides (Lu-177, Cu-67, Re-186, Re-188, and Y-90) for single cells in two source geometries (see figure 3.1). The first geometry considered a surface-bound isotropically emitting point source, whilst the second immersed the cell in a bath of free radioactivity. Together, these geometries represent a targeted intraperitoneal radionuclide therapy. Understanding how each radionuclide differs in terms of the physical process of energy deposition is of use in selecting of a particular radionuclide for this type of therapy.

### 3.3.2 Monte Carlo Simulations

One of the improvements made to EGSnrc in comparison with its predecessor, EGS4, was the ability to simulate individual charged particle elastic scattering events in the vicinity of a medium boundary (single elastic scattering mode). The previous charged particle transport technique used in EGS4 adjusted path lengths for elastic

scattering based on Moliere's multiple scattering theory,<sup>20</sup> which restricted the transport step sizes to lengths over which the theory applied. EGSnrc however, is restricted only by considerations of efficiency, and it turns out that single elastic scattering becomes more efficient to simulate over distances of approximately 3 elastic mean free paths (MFPs).<sup>2</sup> Thus in order to improve the accuracy of the boundary crossing algorithm employed by the simulation, whenever a charged particle is within 3 MFPs of a boundary, EGSnrc runs in single scatter mode by default. Sacrificing efficiency for a more accurate simulation of elastic scattering, we modified the code to run in single scatter mode whenever a charged particle was within 100 MFPs from the nearest boundary. For reference, using the screened Rutherford cross section for electrons<sup>2</sup> of energy  $T = 1$  MeV in water, we estimate  $MFP \approx 0.25 \mu\text{m}$ . Hence in the vicinity of a cell  $20 \mu\text{m}$  in diameter (see figure 3.1) almost all elastic scattering was simulated on an event-by-event basis.

The other major consideration that required attention before approaching this problem was imposed by the minimum simulation cutoff energy for electrons,  $ECUT = 10$  keV. Any electron with  $T \leq 10$  keV is no longer transported and all of the energy is assumed to be locally deposited. Using the CSDA, a 10 keV electron has a range of approximately  $2.5 \mu\text{m}$  in water.<sup>9</sup> Single event spectra for electrons with energies  $< 10$  keV therefore had to be modelled independently of the EGSnrc simulations. To investigate the effect of this cutoff on the calculated single event spectra, we repeated some of the surface bound geometry simulations (described

below) with ECUT ranging from 40 keV downward, so we could estimate the error this parameter introduces by extrapolation.

The simulations were set up in the following manner. In all cases, both the target and the surrounding medium were modelled as water. The target volume was defined as a sphere of 10  $\mu\text{m}$  radius. Energy deposition in the target volume for each history was recorded and tallied in 50 eV wide bins to form a distribution of energies absorbed by the target volume resulting from a given set of initial conditions. The surface-bound radioactivity was simulated as a single isotropically-emitting point source positioned on the surface of the target volume. For both source geometries the specific emission energy of a particle was taken as the mean energy across a 1 keV bin to form a “monoenergetic” single event spectrum. Monoenergetic single event spectra were generated for initial energies from 11 to 2500 keV, spanning the range of emission energies for the radionuclides investigated. Radionuclide-specific spectra can then be generated by appropriately summing the monoenergetic spectra. For each emission energy,  $2 \times 10^6$  histories were collected.

To simulate the free radioactivity it was too inefficient to randomly sample position, energy and trajectory individually for each beta emission (Y-90 for example emits  $\beta$  particles with ranges  $> 1$  cm). Instead, we approximated the spectrum of electrons incident on the target volume. For each radionuclide, the CSDA spectrum was calculated in the manner described by Johns and Cunningham.<sup>21</sup> Under the assumption that the bath of activity is in a state of charged particle equilibrium, the

amount of energy emitted by any small volume is equal to the amount of energy absorbed in the same volume. The spectrum of energies emitted by the volume is given by the radionuclide's beta spectrum, denoted by  $I(T)$ . The relative intensity of electrons of kinetic energy  $T$  in the CSDA spectrum is given by

$$C(T) = \frac{1}{S_{tot}(T)} \int_T^{T_{\beta max}} I(T') dT', \quad (3.15)$$

where  $S_{tot}(T)$  is the total stopping power and  $T_{\beta max}$  is the maximum beta energy for the radioisotope. The beta emission spectra  $I(T)$  and the CSDA spectra  $C(T)$  for the radionuclides used in this study are shown in figure 3.2 a) and b) respectively. For the free radioactivity it was further assumed that the electrons followed random trajectories through the target. Initial trajectory direction cosines were input based on a uniform, random sampling of vectors connecting two points on the surface of the target sphere. To verify this approach, we observed that the resulting path-length distribution (obtained as the distribution of interpolated linear paths through the sphere) corresponds identically with that for a convex body exposed to a uniform isotropic fluence of infinite straight lines. This type of randomness is referred to as isotropic uniform randomness.<sup>22</sup>

Once the monoenergetic single event spectra were obtained for each case they were weighted according to the specific radionuclide's beta emission spectrum and summed to produce the composite radionuclide single event spectrum.<sup>18</sup> This work is not presented here.

### 3.3.3 Results and Discussion

The simulations demonstrated that the single event spectra for low energy electrons ( $< \sim 50$  keV) are characterised by the presence of a peak at a specific energy that corresponds to the initial energy of these electrons. This phenomenon can be seen in the low energy electron single event spectra illustrated figure 3.3 for surface bound (a) and free radioactivity (b). At these energies the target volume may either fully encompass the range of the electrons, or allow for the possibility that the electrons deposit all of their energy in the target volume because their tortuous paths are completely confined to the volume, which would result in the observed peaks. For subsequent calculations that required spectra for electrons with initial energies  $< 10$  keV, the spectra were modelled after the 11 keV spectrum with an appropriately defined peak. The low-z tails decreased sufficiently from 15 to 11 keV that they were not deemed to constitute a significant portion of the spectrum below 10 keV.

Higher energy electrons crossing the target volume were seen to deposit less energy than low energy electrons, which is likely due to the decreased stopping power. Single event spectra for electrons with higher initial kinetic energies are shown in figure 3.4 for surface bound (a) and free radioactivity (b). The surface bound spectra appear almost symmetric about the midpoint of the distributions, while the spectra for the free radioactivity are peaked toward the higher energy range of the distribution. The differences in the spectra between surface bound and free radioactivity at all energies stem from the differences in the path length distributions that describe the electron trajectories.

We compared results obtained using EGSnrc to those of two other Monte Carlo codes by repeating the calculations of other investigators for two beta energies in the surface bound source geometry. Bolch and Kim<sup>23</sup> presented single event spectra for 100 keV and 1 MeV electrons bound to the surface of a 10  $\mu\text{m}$  diameter cell as determined with the OREC Monte Carlo code. Stewart *et al.*<sup>24</sup> repeated this work with the PENELOPE code system. The OREC code system tracks electrons in water event by event, down to a cutoff energy of 7.4 eV<sup>25</sup>. The PENELOPE system implements a condensed history algorithm similar to that described for EGSnrc. Hard electron interactions, defined as events in which the polar scattering angle or the energy loss exceed user-selected values,<sup>26</sup> are simulated in a “detailed” way while multiple scattering theory is applied to the remaining soft interactions.<sup>24</sup>

Table 3.2 contains the values of  $\langle z_f \rangle$ , the frequency-mean specific energy for a sphere of radius 5  $\mu\text{m}$ , determined by all three code systems. There is very good agreement between EGSnrc and OREC for 1 MeV electrons. At 100 keV, EGSnrc produces a value for  $\langle z_f \rangle$  that is 7.4% lower than that from OREC and 2.4% greater than that from PENELOPE. The shapes of the 100 keV spectra are similar, though not identical, and it is unclear if this results from differences in the transport physics or is a potential artefact related to the 10 keV cutoff energy.

The effect of the cutoff energy on the Monte Carlo generated monoenergetic single event spectra was found to be minimal. Spectra for  $T = 0.5$  and 1.0 MeV were



indistinguishable whether ECUT was set to 10 keV or 40 keV, and the  $T = 0.1$  MeV spectrum showed only a very small difference in the low-z tail. This suggests that for the majority of energies relevant to beta-emitting radionuclide therapy, the 10 keV cutoff will not adversely affect results. For  $T = 20$  and 50 keV and  $ECUT = 15$  keV and 20 keV respectively, the higher ECUT values increased the height of the high-z peak and slightly decreased the tail regions. However, an investigation of peak height versus ECUT value suggests that at  $ECUT = 10$  keV, these differences are approaching an asymptotic value. In general, we conclude that for very low values of  $T$ , EGSnrc may slightly overestimate the true number of events depositing all of their energy in the target volume, but that this overestimation would not be significant in the context of the overall single event spectra generated for each radionuclide.

### **3.4 OVERVIEW OF DETECT2000**

#### *3.4.1 Introduction to DETECT2000*

One of the problems considered in the present work concerns the transport of optical photons through the scintillation screen of the aS500 EPID and an adjoining optical filter, and onto the amorphous silicon photodiode plane. Because this problem involves multiple optical scattering and absorption events, deterministic solutions that incorporate simple ray tracing and attenuation of first and second order interaction events proved to be insufficiently accurate. Hence once again Monte Carlo techniques appeared to offer the most attractive method for solution. The transport of non-ionizing radiation, and in particular optical photons, cannot be performed with

EGSnrc because at these much lower energies, the physics of photon interactions is markedly different. Instead, we opted to use the DETECT2000 Monte Carlo code.<sup>27</sup>

DETECT2000 was developed to model the behavior of optical systems, with special emphasis on scintillation detectors.<sup>27</sup> It evolved from the DETECT code originally developed at the University of Michigan,<sup>28</sup> and its successor DETECT97 created at TRIUMF, to model the position and energy response of positron emission tomography (PET) detectors.<sup>29</sup> DETECT2000 incorporates several new features including wavelength dependent transport coefficients and an improved random number generator, and has been translated from the C to C++ language. The code initiates individual scintillation photons according to a user-defined distribution and follows each through different detector components. It simulates transmission and reflection from surfaces, accounts for bulk absorption, re-emission, and scattering processes, and records the fate of each photon. Distances to collision events are determined by sampling from a probability distribution function that is based on the combined mean free paths for scattering and absorption. Relative cross section weightings then determine which specific interaction takes place.

DETECT2000 requires three parameters to simulate the propagation of photons through each material: 1) the scattering coefficient, 2) the absorption coefficient, and 3) the index of refraction. The interaction coefficients are specified in terms of the photon mean free path between scattering or absorption events. In addition, the boundaries of each material must be described as one of six surface

types, which define the transmission and reflection properties at that surface. We considered two surface types in this work. One was a *polished* surface where the boundary is defined at a flat intersection of surfaces. Here photon boundary crossing is dictated by Fresnel reflection and Snell's law of refraction. The other was a *ground* surface, where the interface between the two materials is assumed not to be perfectly flat. Instead the surface is roughened such that the normal to the surface in the refraction calculations follows a Lambertian distribution.<sup>27</sup>

Details of the optical parameters used in the DETECT2000 simulations for the aS500 EPID are provided in section 2.3.2 and a summary is provided in table 2.2.

#### 3.4.2 *Benchmarking DETECT2000*

Because DETECT2000 is much less well known in the medical physics community than EGSnrc, we believe it is appropriate to include some discussion of the applications for which this code has been used previously, as well as a description of the preliminary in-house benchmarking performed.

As mentioned, DETECT2000 was derived from the DETECT code which was used by Tsang *et al.*<sup>29</sup> to model the position encoding multicrystal detectors used in PET. It was tested against experimental results acquired using the EXACT HR PLUS block detector (Siemens Medical Solutions USA, Inc., Malvern, PA). DETECT was able to reproduce the line spread function (LSF) for four columns of crystals with an accuracy of  $\pm 0.5$  mm and to predict crystal-by-crystal photopeak pulse heights and

full-widths at half maximum (FWHMs) within a range of  $\pm 14\%$  and  $+9\%/-6\%$ , respectively. DETECT2000 has been used by Cayouette *et al.*<sup>30</sup> to determine the performance of a multilayer BGO scintillation block (also used for PET). More recently, Monajemi *et al.*<sup>31</sup> used DETECT2000 to model the transport of optical photons in a CdWO<sub>4</sub> scintillation detector (being developed for MVCT) to determine detector imaging characteristics. Maximum discrepancies between measured and modeled MTF( $f$ ), relative NPS( $f$ ) and DQE( $f$ ) were found to be 1.5%, 1.2% and 1.9%, respectively, for 1.25 MeV photons. MTF( $f$ ) discrepancy was shown to be 2.5% for a 6 MV beam.

We considered a simple problem having an analytical solution to verify the basic operation of DETECT2000. Figure 3.5 illustrates the geometry of the problem. We consider an isotropically emitting point source of optical photons centered inside a  $40 \times 40 \times 40$  cm<sup>3</sup> volume. The medium inside the volume is defined such that the scattering mean free path is very long ( $10^3$  cm) and the absorption mean free path is very short (0.1 cm). We then score the photons that cross a plane defined  $z$  cm above the point source. The number of photons that reach the scoring plane,  $N_{\text{detected}}$ , can be determined by considering the photons that reach a ring of radius  $r$  and incremental area  $dA = 2\pi r dr$ , a distance  $l$  from the source.

$$N_{\text{detected}} = \frac{N_0}{2} \int_0^{20 \text{ cm}} \frac{rz \exp(-\lambda \sqrt{r^2 + z^2})}{(r^2 + z^2)^{3/2}} dr \quad (3.16)$$

Here  $N_0$  is the number of photons emitted from the point source ( $10^6$ ), and  $\lambda$  is the absorption coefficient ( $10 \text{ cm}^{-1}$ , scattering ignored in this analysis). The right-hand

side of Eq. 3.16 was evaluated numerically. Because of the rapid fall-off of the integrand, it is sufficient to consider a radial integration out to 20 cm for values of  $z \ll 20$  cm. We considered integration planes at  $z = 0.1, 0.2$  and  $0.4$  cm. Table 3.3 summarizes both the analytical and Monte Carlo results, relative differences between which are minimal and decrease as the number of photons scored for a particular plane increases, roughly following an  $N^{-1/2}$  trend.

This simple investigation of DETECT2000 confirmed our understanding of its operation and instilled confidence in the results it provided in later investigations.

### 3.5 SUMMARY

In the present work we are concerned with modeling the response of the aS500 EPID to MV radiation. Analytic approaches to the problems we wish to study are complex and only feasible by introducing simplifying approximations. Thus, the Monte Carlo method is a superior alternative for examining many of the problems under consideration. In order to model the transport of ionizing radiation incident on the detector through the various components of the imaging cassette and arrive at an estimate of the dose deposited in the phosphor (including the dose from scattered particles), we chose to use EGSnrc. We performed some supplementary in-house benchmarking of this code, and also demonstrated that it can be successfully applied to a microdosimetry problem. In order to model the spreading of optical photons within the EPID phosphor layer we chose a separate code, DETECT2000, which was

specifically developed by the nuclear and particle physics community to model the transport of optical photons in scintillation detectors.

Material	thickness (cm)	D <sub>EGS</sub> (Gy)	D <sub>ana</sub> (Gy)	difference (%)
Cu	0.00100	1.804	1.813	0.5
Cu	0.01000	2.608	2.684	2.9
Gd	0.00100	1.515	1.498	-1.1
Gd	0.00340	1.766	1.783	1.0
H <sub>2</sub> O	0.00025	2.373	2.370	-0.1
H <sub>2</sub> O	0.01430	2.680	2.752	2.7

**Table 3.1.** A summary of Monte Carlo thin foil dose estimates for a 1 MeV incident photon beam compared to corresponding analytical predictions, for a variety of materials and foil thicknesses. In general, discrepancies are 1% or less where the assumptions inherent in the analytical method are strongest.

Monte Carlo System	$\langle z_f \rangle$	
	0.1 MeV	1.0 MeV
EGSnrc	0.63	0.27
OREC	0.68	0.26
PENELOPE	0.615	Within 6 % of OREC

**Table 3.2.** Values of  $\langle z_f \rangle$  calculated for a sphere of radius 5  $\mu\text{m}$  using the Monte Carlo codes EGSnrc, OREC, and PENELOPE. Agreement between EGSnrc and OREC is very good at 1 MeV, but shows a 7.4 % discrepancy at 0.1 MeV. PENELOPE also shows reasonably good agreement with EGSnrc.

Plane	z (cm)	$N_{\text{DETECT2000}}$	$N_{\text{analytical}}$	diff. (%)
1	0.1	74211	74246	0.05
2	0.2	18746	18767	0.11
3	0.4	1562	1599	2.31

**Table 3.3.** The number of optical photons passing three scoring planes for a simple benchmarking problem (Fig 3.5) detected by DETECT2000, compared to the analytical expression of Eq. 3.16.  $10^6$  photons were simulated. Predictably, the relative difference between the Monte Carlo results and the theory increases as the number of particles detected decreases.



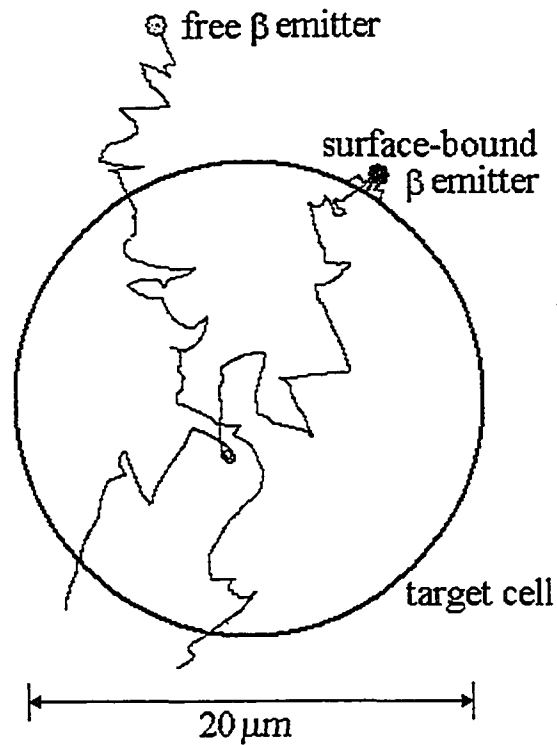


**Figure 3.1.** The geometries used in the single cell beta dosimetry investigation. In the first geometry a beta-emitting radionuclide is part of an antibody that binds to the surface of a spherical cell. In the second geometry we consider the case of a cell immersed in a bath of radioactivity. Sample electron tracks are shown for each case.

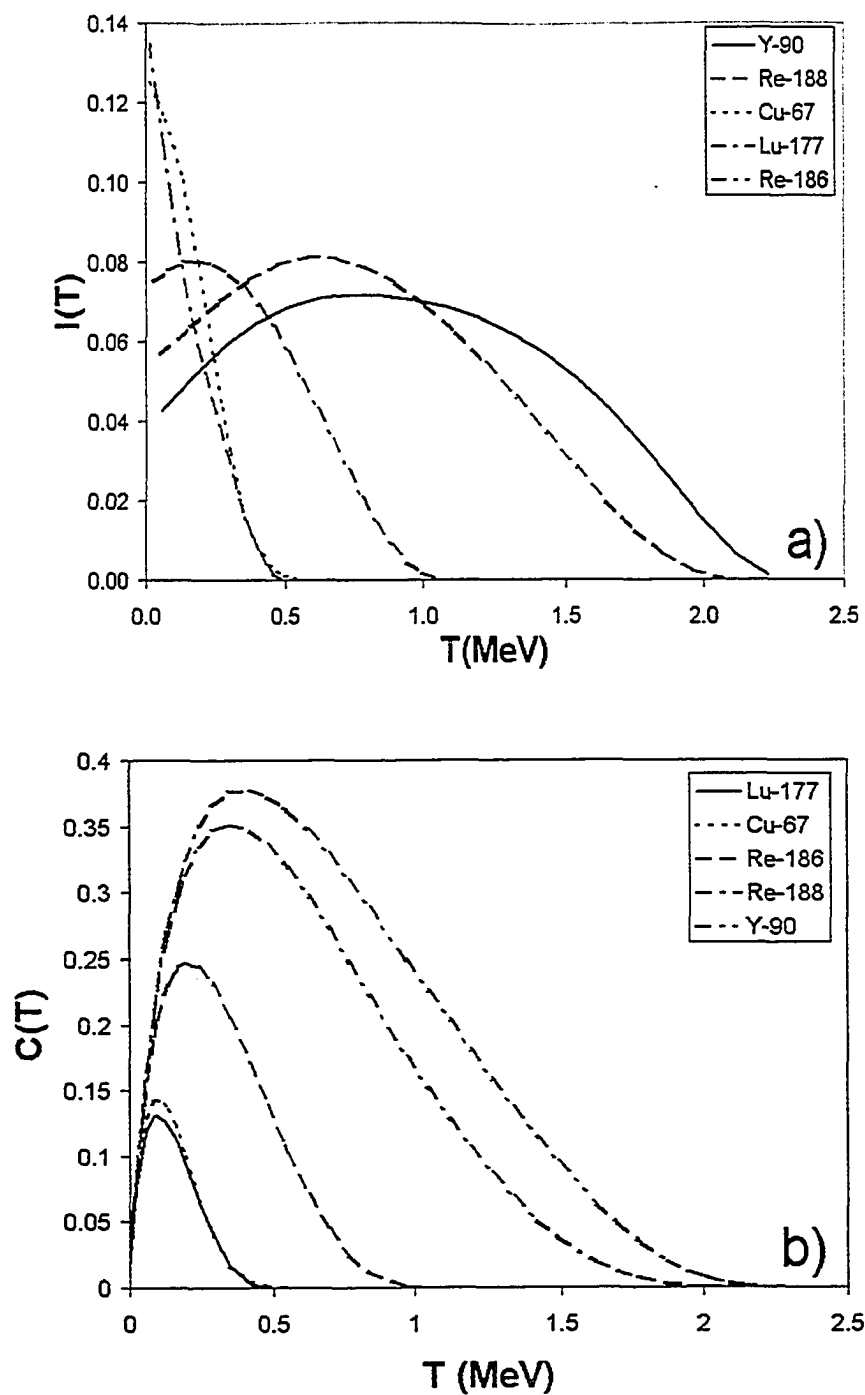


**Figure 3.2.** Beta emission spectra (a) and CSDA spectra (b) for the radionuclides used in this study.  $I(T)$  denotes the relative intensity of beta emissions of kinetic energy  $T$ .  $C(T)$  denotes the relative intensity of electrons with energy  $T$  at any point in the medium. The spectra have not been normalised.

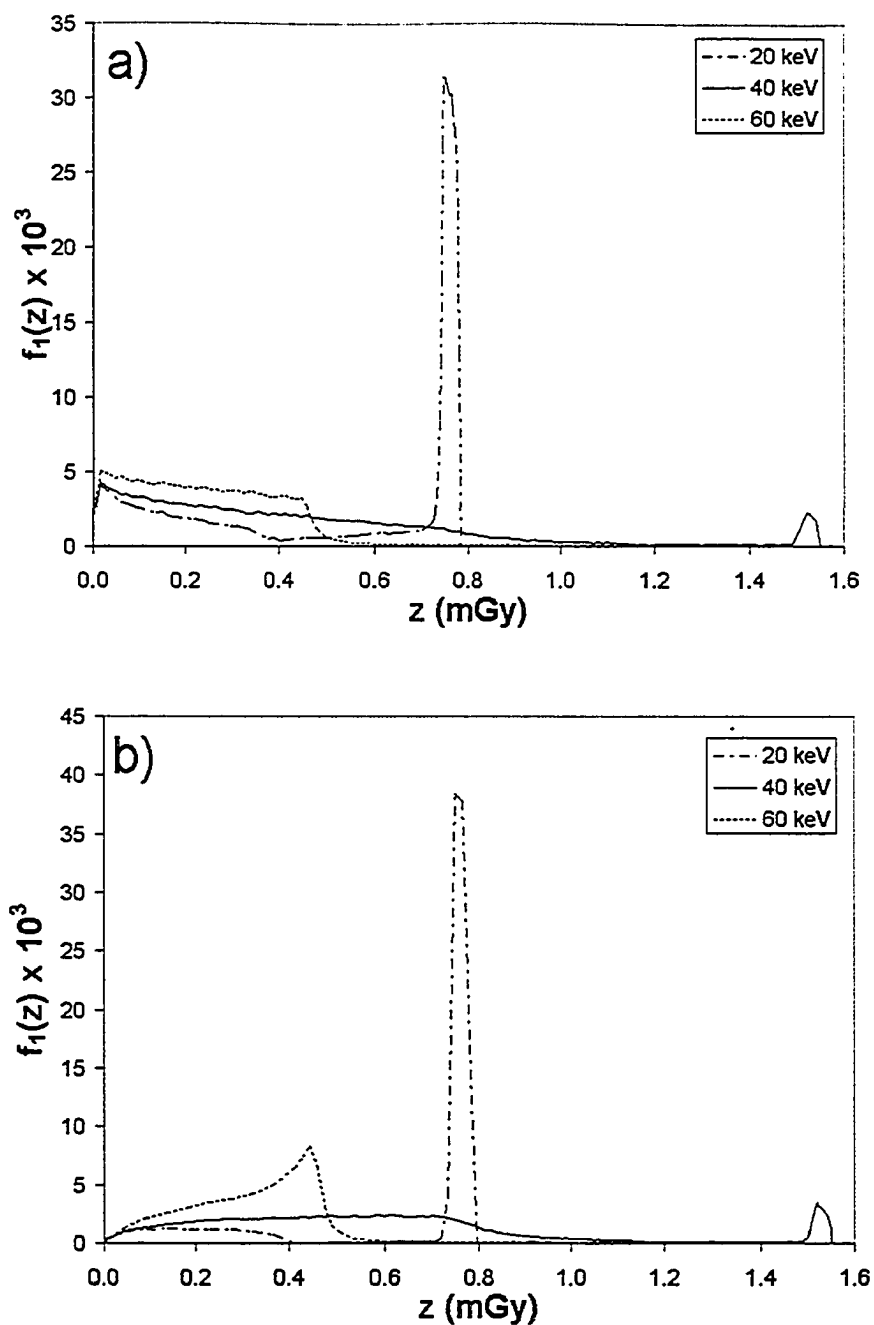


**Figure 3.3.** Single event spectra for low energy electrons in the surface bound (a) and in the free radioactivity (b) geometries. Below 50 keV the spectra show a peak at a value of  $z$  corresponding to the initial energy of the electrons. The low energy spectra change rapidly with energy.

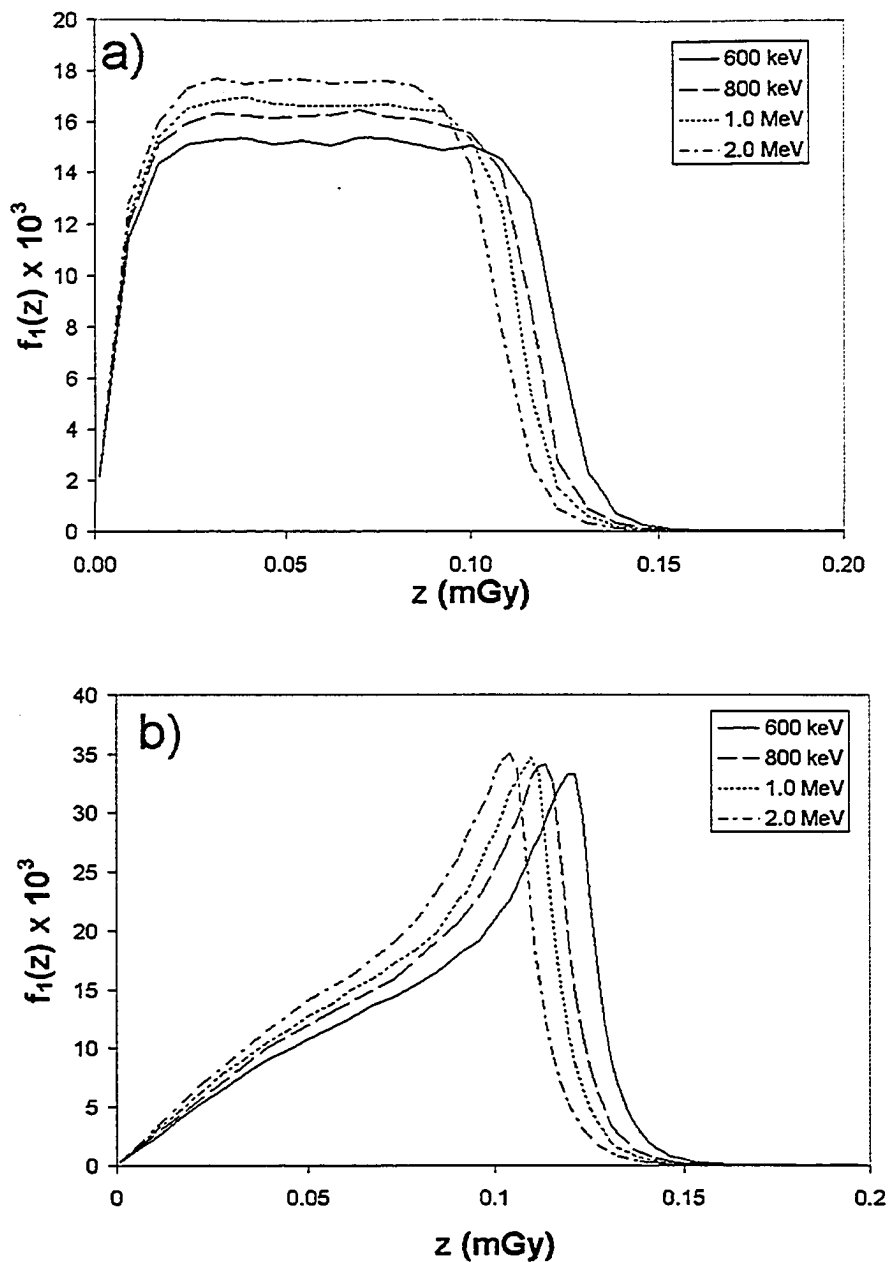


**Figure 3.4.** Single event spectra for high energy electrons in the surface bound (a) and free radioactivity (b) geometries. The spectra change more slowly at these energies. The free radioactivity geometry results show a shift towards higher  $z$  values relative to the corresponding surface bound case due to larger mean path lengths through the target.

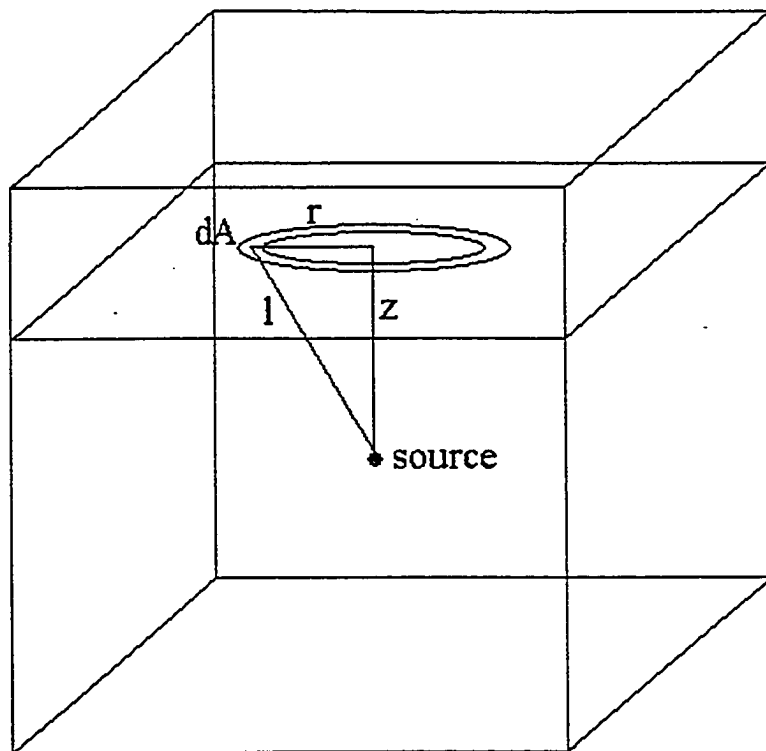


**Figure 3.5.** A point source of optical photons inside a  $40 \times 40 \times 40 \text{ cm}^3$  cube. The dominant interaction in the medium is absorption. Photons are scored as they cross a plane at a distance  $z$  above the source.

### 3.6 REFERENCES

- <sup>1</sup>R. Eckhardt, "Stan Ulam, John von Neumann, and the Monte Carlo method," *Los Alamos Science* **15**, 131-137 (1987).
- <sup>2</sup>I. Kawrakow and D.W.O. Rogers, *The EGSnrc Code System: Monte Carlo Simulation of Electron and Photon Transport*, NRCC Report PIRS-701 (NRCC, Ottawa ON, 2002).
- <sup>3</sup>G.S. Fishman, *Monte Carlo Concepts, Algorithms and Applications*, 1 ed. (Springer Verlag, London, 1996).
- <sup>4</sup>R. Y. Rubinstein, *Simulation and the Monte Carlo Method*, 1 ed. (Wiley-Interscience, Hoboken, NJ, 1981).
- <sup>5</sup>A. F. Bielajew, *Fundamentals of the Monte Carlo method for neutral and charged particle transport* (pre-publication manuscript, Ann Arbor MI, 2001).
- <sup>6</sup>F. James, "RANLUX: A Fortran implementation of the high-quality pseudorandom number generator of Luscher," *Computer Phys Commun* **79**, 111-114 (1994).
- <sup>7</sup>M. Luscher, "A portable high-quality random number generator for lattice field theory simulations," *Computer Phys Commun* **79**, 100-110 (1994).
- <sup>8</sup>I. Kawrakow, "Accurate condensed history Monte Carlo simulation of electron transport. II. Application to ion chamber response simulations," *Med Phys* **27** (3), 499-513 (2000).
- <sup>9</sup>M. J. Berger, J. S. Coursey, and D. S. Zucker, *ESTAR, PSTAR, and ASTAR: Computer Programs for Calculating Stopping-Power and Range Tables for Electrons, Protons, and Helium Ions (version 1.2.2)*. [Online] Available: <http://physics.nist.gov/Star> [2005, February 7] (National Institute of Standards and Technology, Gaithersburg, MD, 2005).
- <sup>10</sup>M. J. Berger, "Monte Carlo calculation of the penetration and diffusions of fast-charged particles," in *Methods in Comput Phys*, edited by B. Alder, S. Fernbach, and M. Rotenberg (Academic, New York, 1963), Vol. 1, pp. 135-215.
- <sup>11</sup>D. W. O. Rogers, I. Kawrakow, J.P. Seuntjens, and B.R.B. Walters, NRC User Codes for EGSnrc Report No. PIRS-702(revA), 2002.
- <sup>12</sup>I. Kawrakow, "Accurate condensed history Monte Carlo simulation of electron transport. I. EGSnrc, the new EGS4 version," *Med Phys* **27** (3), 485-98 (2000).
- <sup>13</sup>B.R.B. Walters, J. Treurniet, D. W. O. Rogers, and I. Kawrakow, QA tests of the EGSnrc system and comparison with EGS4 (Draft) Report No. PIRS-703, 2003.

- <sup>14</sup>F. H. Attix, *Introduction to Radiological Physics and Radiation Dosimetry* (John Wiley and Sons, New York NY, 1986).
- <sup>15</sup>ICRU, ICRU Report 37: Stopping Powers for Electrons and Positrons, 1984.
- <sup>16</sup>H. W. Lewis, "Multiple Scattering in an Infinite Medium," *Phys. Rev.* **78**, 526-529 (1950).
- <sup>17</sup>I. Kawrakow and A. F. Bielajew, "On the condensed history technique for electron transport," *Nuclear Instruments and Methods* **142B**, 253-280 (1998).
- <sup>18</sup>A. M. Syme, C. Kirkby, T. A. Riauka, B. G. Fallone, and S. A. McQuarrie, "Monte Carlo investigation of single cell beta dosimetry for intraperitoneal radionuclide therapy," *Phys Med Biol* **49** (10), 1959-72 (2004).
- <sup>19</sup>ICRU, ICRU Report 36: Microdosimetry, 1983.
- <sup>20</sup>G. Z. Moliere, "Theorie der Streuung schneller geladener Teilchen. I. Einzelstreuung am abgeschirmten Coulomb-Feld," *Z. Naturforsch* **2a**, 133-145 (1947).
- <sup>21</sup>H. E. Johns and J. R. Cunningham, *The Physics of Radiology 4th ed.* (Springfield: Charles C. Thomas, Springfield, IL, 1983).
- <sup>22</sup>A. M. Kellerer, "Chord-length distributions and related quantities for spheroids," *Radiat. Res.* **98**, 425-37 (1984).
- <sup>23</sup>W.E. Bolch and E-H. Kim, "Calculations of electron single event distributions for use in internal beta microdosimetry," *Radiat. Prot. Dosim.* **52**, 77-80 (1994).
- <sup>24</sup>R. D. Stewart, W. E. Wilson, J. C. McDonald, and D. J. Strom, "Microdosimetric properties of ionizing electrons in water: a test of the PENELOPE code system," *Phys Med Biol* **47**, 79-88 (2002).
- <sup>25</sup>E-H. Kim, W.E. Bolch, W. D. Reece, and J. D. Poston, "A microdosimetric algorithm for electron point kernel data: 1. Monoenergetic electron sources," *Radiat. Prot. Dosim.* **63**, 245-52 (1996).
- <sup>26</sup>J. Baro, J. Sempau, J. M. Fernandez-Varea, and F. Salvat, "PENELOPE: an algorithm for Monte Carlo simulation of the penetration and energy loss of electrons and positrons in matter," *Nucl. Instrum. Methods Phys. Res B* **100**, 31-46 (1995).
- <sup>27</sup>C. Moisan, F. Cayouet, and G. McDonald, *DETECT2000 A Program for Modeling Optical Properties of Scintillators* (Dept. of Electrical and Computer Engineering, Laval University, Quebec City, QC, 2000).

<sup>28</sup>G. F. Knoll, T. F. Knoll, and Henderson T. M., "Light Collection Scintillation Detector Composites for Neutron Detection," *IEEE Trans. Nucl. Sci.* **35** (1), 872-875 (1988).

<sup>29</sup>G. Tsang, C. Moisan, and J. G. Rogers, "A simulation to model position encoding multicrystal PET detectors," *IEEE Trans. Nucl. Sci.* **42** (6), 2236-2243 (1995).

<sup>30</sup>F. Cayouet, C. Moisan, N. Zhang, and C.J. Thompson, "Monte Carlo Modeling of Scintillator Crystal Performance for Stratified PET Detectors with DETECT2000," *IEEE Trans. Nucl. Sci.* **49** (3), 624-628 (2002).

<sup>31</sup>T. T. Monajemi, S. Steciw, B. G. Fallone, and S. Rathee, "Modeling scintillator-photodiodes as detectors for megavoltage CT," *Med Phys* **31** (5), 1225-34 (2004).



## Chapter 4: Comprehensive Monte Carlo calculation of the point spread function for a commercial a-Si EPID

### 4.1 INTRODUCTION

While a-Si EPIDs are primarily employed as MV imagers for patient position verification, there has been a significant amount of work in recent years to exploit the quantitative dosimetric information available from these devices. Because of their generally linear response to dose,<sup>1-3</sup> a-Si EPIDs can be used to produce a two dimensional pixel map of entrance or exit energy fluence within a given treatment field. The most immediate application of this work employs the EPID for pre-treatment verification of fields with high dose gradients, such as those used in intensity modulated radiotherapy (IMRT).<sup>4</sup> A future objective is to perform exit dosimetry (projecting upstream from the detector to obtain a dose distribution within the patient) in a clinical setting.

To date, commercial a-Si EPIDs have used an indirect detection scheme to generate an image. An incident photon beam enters the detector stack (eg. see Fig. 4.1) and passes through several materials before interacting with a copper plate where Compton scattering predominantly occurs. The resulting electrons migrate down from the plate into the scintillation screen and deposit energy within. This causes the screen to phosphoresce – emitting optical photons, which may then be detected by an array of amorphous silicon photodiodes. This generates a charge buildup on each diode that can be integrated and read out electronically forming a digital image. Contributions to the image also come from photons that have scattered upstream in

parts of the detector such as the collision cap, supporting materials, or solid water buildup, and downstream in the photodiode glass substrate or rear cover. These multiple radiation transport paths result in blurring of the fluence incident on the detector. Recovering the incident energy fluence is necessary for making accurate measurements of transmission dose,<sup>4</sup> and can be accomplished approximately using standard deconvolution techniques.<sup>5</sup> These techniques require a blur kernel, or point spread function (PSF) – the response of the system to a beam of infinitesimal width – which, in turn, is the motivation for undertaking the study presented in this chapter.

Previous Monte Carlo studies of the PSF as well as the detective quantum efficiency (DQE) of a-Si EPIDs have made use of models that contain the basic components of the detector such as the copper plate, scintillation screen, glass substrate and in some cases water buildup.<sup>2,4,6,7</sup> Schach von Wittenau *et al.*<sup>8</sup> developed a “notional” detector, which was intended to be representative of a typical a-Si EPID and included an outside cover. They concluded that radiation scattered from “non-detector” components should be a significant source of image degradation. In order to incorporate such effects, our study focuses on a commonly available commercial EPID, the Varian aS500 (Varian Oncology Systems, Palo Alto, CA), which is described in detail in the second chapter. We incorporate a comprehensive model of the aS500 based on data provided by the manufacturer (Sec. 2.3). From the model we derive a blur kernel for the aS500 for 6 and 15 MV photon beams using Monte Carlo simulation. We break down the physical processes involved in signal creation into: i) dose deposition in the scintillation screen, and ii) spreading of optical photons emerging from the screen through an optical filter and onto the a-Si

photodiodes. We merge these two results using a convolution process to obtain a comprehensive overall PSF ('comprehensive' refers to simulations run with a full material description of the detector). A measurement of the line spread function (LSF) is used to verify the form of each kernel. We then evaluate the performance of the kernels in deblurring clinical images by comparing relative fluence profiles against those measured with a diamond detector. The comprehensive kernels are well fit by triple exponential functions, and are also well approximated by semi-analytical kernels based on a simplified model of the detector.

## 4.2 THEORY AND METHODS

### 4.2.1 *Point Spread Function*

Monte Carlo methods are used to simulate dose deposition and optical spreading independently. Figure 4.1 provides an illustration of the geometry used. Dose deposition in ten equal phosphor layers is scored in response to a pencil beam of photons normally incident at the surface of the buildup material on the central axis (CAX). Optical spreading is scored in response to isotropically emitted optical photons originating at ten equally spaced depths (corresponding to the centers of the modeled phosphor sub-layers), along the CAX. Both the magnitudes of dose deposition within the phosphor and of optical spreading will be shown to have a dependence on depth within the scintillation screen. The first dependence arises because dose is not uniformly deposited within the screen, and the second because the thickness of the screen influences the output optical fluence.<sup>9</sup> As a result, we begin

with the assumption that the overall point spread function ( $\text{PSF}^{\text{overall}}$ ) can be obtained as a convolution between two depth dependent components: the phosphor dose point spread function ( $\text{PSF}^{\text{rad}}$ ) and the optical point spread function ( $\text{PSF}^{\text{opt}}$ ),

$$\text{PSF}^{\text{overall}}(r) = \frac{\sum_{i=1}^{10} \left( w_{z_i} \int_0^{\infty} \text{PSF}^{\text{rad}}(r', z_i) \cdot \text{PSF}^{\text{opt}}(r-r', z_i) dr' \right)}{\sum_{i=1}^{10} w_{z_i}}, \quad (4.1)$$

where  $r$  is the radial distance from the EPID entry point of an infinitesimally narrow beam and  $z_i$  is the discretized phosphor depth corresponding to the center of a phosphor layer. Implicit in this expression is the further assumption that each PSF is independent and spatially invariant. The dose kernels were normalized to the CAX Monte Carlo scoring bin of maximum dose. We assume that optical photon production is linearly proportional to the dose deposited.<sup>10,11</sup> The optical kernels for each depth ( $z_i$ ) were weighted ( $w_{z_i}$ ) by the ratio of the number of optical photons that reach the photodiode plane from depth  $z_i$  to the number that reach it from the closest depth  $z_{10}$ .

#### 4.2.2 EGSnrc Simulations

EGSnrc version 3<sup>12,13</sup> with user code DOSRZnrc, (described in Sec. 3.2) was used to simulate the transport of ionizing radiation and score the dose deposited in the phosphor screen. We used the default cut-off energies  $\text{PCUT} = \text{AP} = 10$  keV and  $\text{ECUT} = \text{AE} = 521$  keV. We modeled incident fluence as a thin photon pencil beam ( $r = 0.001$  cm) having an energy distribution taken from published spectral data for generic Varian 6 and 15 MV beams, grouped into 0.25 MeV energy bins and

averaged across a radial bin ( $r = 2.5$  cm) at the central axis.<sup>14</sup> Accelerator-specific phase-space files that relate energy distribution to beam position were not used. The photons were normally incident on the surface of the solid water buildup layer.

Dose deposition within each of the 10 layers comprising the scintillation screen was scored in equally spaced radial bins ( $\Delta r = 0.00784$  cm, or 1/10 of a pixel width) to generate  $\text{PSF}^{\text{rad}}$ . The area of the incident pencil beam was only  $3.14 \times 10^{-6}$  cm<sup>2</sup>, compared to  $1.93 \times 10^{-4}$  cm<sup>2</sup> area of the central scoring cylinder. Dose was scored out to a maximum radial distance of 30 cm because that provided a balance between characterizing the detector response over the full  $30 \times 40$  cm<sup>2</sup> imaging area, and the computation time required to obtain dose estimates with reasonable statistical uncertainties in the outermost bins. For each dose kernel at least  $2 \times 10^8$  histories were run, resulting in a maximum statistical uncertainty of  $\pm 0.2$  % in the central axis dose. The average dose in the full thickness of phosphor is

$$\langle \text{PSF}^{\text{rad}}(r) \rangle = \frac{1}{10} \sum_{i=1}^{10} \text{PSF}^{\text{rad}}(r, z_i). \quad (4.2)$$

In order to accurately weight the optical spreading kernel with respect to the site of optical photon emission, it is necessary to understand how dose varies with depth within the phosphor. To investigate this we generated a central axis depth dose curve by summing the dose in the first five radial bins (a diameter of  $\sim 1$  pixel width) for each of the 10 screen layers.

### 4.2.3 *DETECT2000 Simulations*

For the optical component of the problem we used the DETECT2000 Monte Carlo code,<sup>15</sup> described in Sec. 3.4. Figure 4.2 depicts the geometry under consideration. As a result of the fluence of electrons and photons  $\Phi_0(x',y')$  incident on the screen, a three-dimensional dose distribution builds up within it. From the subsequent phosphorescence, we wish to determine the output optical fluence incident on the amorphous silicon array of the detector stack,  $\Phi(x,y)$ .

Simulations were initiated with non-polarized photons originating isotropically<sup>16</sup> at ten equally spaced points (point sources on CAX) within the scintillation screen, corresponding to the midplanes of the EGSnrc scoring layers. All sources were given equal weighting for the simulations. The variation in optical source intensity due to the variation in dose with screen depth is incorporated into the overall kernels by the relative weighting of the dose kernels. Monoenergetic photons of wavelength 545 nm were specified because this is the dominant wavelength in the  $\text{Gd}_2\text{O}_2\text{S:Tb}$  emission spectrum by an order of magnitude.<sup>17</sup> Although the index of refraction, and scattering and absorption coefficients have a small dependence on wavelength, the variance in wavelength is small ( $< 4\%$ ),<sup>17</sup> and therefore we expect that existing uncertainties in the values of the photon transport parameters (ie. scatter  $\text{MFP} = 10\text{--}25 \mu\text{m}$  in  $\text{Gd}_2\text{O}_2\text{S:Tb}$ ) will be the dominant source of uncertainty in our results. Photons were scored in radial bins ( $\Delta r = 0.00392 \text{ cm}$ , or  $1/20$  of a pixel width) as they crossed the boundary plane between the filter and the a-Si photodiodes. For each point source,  $1.5 \times 10^7$  histories were run. Additional histories ( $7 \times 10^7$ ) were simulated for the tenth layer to look for evidence of a change in the observed

exponential falloff at larger radii, as some authors have used a double-exponential form to model optical spreading.<sup>2,4,18</sup>

In addition to the optical spreading kernels generated in response to photons emitted from each layer  $z_i$ , which are used in our comprehensive overall kernel, we also consider an average response kernel defined as

$$\langle \text{PSF}^{\text{opt}}(r) \rangle = \frac{\sum_{i=1}^{10} \text{PSF}^{\text{opt}}(r, z_i) \cdot \text{PSF}^{\text{rad}}(r, z_i) \cdot w_{z_i}}{\sum_{i=1}^{10} w_{z_i}}, \quad (4.3)$$

where  $\text{PSF}^{\text{rad}}(r, z_i)$  is the relative central axis dose to layer  $z_i$  and  $w_{z_i}$  is the relative proportion of optical photons that strike the photodiode plane emitted from layer  $z_i$ .

#### 4.2.4 Combining the Kernels

The phosphor dose and optical PSF components were obtained in a cylindrical geometry for two reasons: first, because the PSF is, in theory, symmetric in the azimuthal direction and secondly, because annular bins of width  $\Delta r$  exhibit smaller statistical uncertainty than scoring bins of dimension  $\Delta r \times \Delta r$  in Cartesian geometry. The kernels were combined in radial frequency space using the Hankel transform.<sup>19</sup> This allowed us to preserve the resolution necessary to adequately describe the optical kernels without the need for a large amount of computer memory. Eqs. (4.4-4.6) describe this process.

$$\text{HPSF}^{\text{rad}}(q, z_i) = 2\pi \int_0^{\infty} \text{PSF}^{\text{rad}}(r, z_i) J_0(2\pi q r) r dr \quad (4.4)$$

$$\text{HPSF}^{\text{opt}}(q, z_i) = 2\pi \int_0^{\infty} \text{PSF}^{\text{opt}}(r, z_i) J_0(2\pi qr) r dr \quad (4.5)$$

$$\text{PSF}^{\text{overall}}(r) = \frac{2\pi \sum_{i=1}^{10} \int_0^{\infty} (\text{HPSF}^{\text{rad}}(q, z_i) \cdot \text{HPSF}^{\text{opt}}(q, z_i)) J_0(2\pi qr) q dq}{\sum_{i=1}^{10} w_{z_i}} \quad (4.6)$$

Here  $q$  is the radial frequency and  $J_0(2\pi qr)$  is the Bessel function of the first kind of order 0. We used numerical quadrature to perform each of the integrations (interpolating  $\text{PSF}^{\text{rad}}(r, z_i)$  to match sampling intervals).

In order to render it suitable for image deconvolution, we mapped the radial  $\text{PSF}^{\text{overall}}$  onto a  $42 \times 42 \text{ cm}^2$  Cartesian grid having the same pixel pitch as the EPID. As pointed out by Rathee *et al*<sup>20</sup> the area overlap mapping method can lead to errors in the Cartesian pixel values in steep gradient regions. We overcame this problem by exploiting the small bin width in our model and dividing each pixel into  $31^2$  micropixels. Each micropixel was assigned the value of the radial region with which it overlapped most, and the final pixel value obtained as the average over its composite micropixels.

#### 4.2.5 Experimental Measurement of the Line Spread Function

To provide experimental confirmation for this analysis, a standard angled slit technique<sup>21</sup> was used to measure the EPID line spread function (LSF). The angled slit technique was developed to measure the presampled analog modulation transfer function of a system beyond the Nyquist frequency (beyond which digital sampling



introduces an aliasing effect). A line of radiation is projected through a slit oriented at a small angle ( $\sim 1-3^\circ$ ) with respect to one of the axes of the pixel matrix. Without this angle, the LSF is sampled only at points separated by a single pixel width. Introducing the angle allows us to identify the center of the slit (via maximum pixel values) with a precision smaller than a pixel width, and then to sample the LSF at distances from that center not restricted to integer multiples of a pixel width.

An illustration of the experimental apparatus is given in figure 4.3. Images were taken using a pair of machined lead blocks ( $25 \times 10 \times 5 \text{ cm}^3$ , 25 cm in the beam direction) separated by steel shims that formed a slit of width  $380 \mu\text{m}$  to generate a line of incident radiation on the detector. The blocks were supported by a translation stand, which allowed the slit to be angled at  $1.7^\circ$  with respect to the EPID photodiode array. A  $2 \times 5 \text{ cm}^2$  field (defined at isocenter) was projected onto the blocks, which were placed in intimate contact with the EPID deployed at 140 cm from the source. Solid water buildup layers 0.5 and 2.0 cm thick were placed on top of the EPID for the 6 and 15 MV beams, respectively. A pair of images were taken for each measurement: the first with the beam traveling through the slit, and the second with the beam slightly offset so as to miss the slit. Each image was subject to the standard correction where a dark field image was subtracted from the raw image and the result divided by a flood field image (Sec 2.2.4). For both images the high (quality) imaging mode was used, with the number of frame averages raised to 1000 to increase the signal-to-noise ratio.

The pixel values used to form the LSF were obtained by subtracting the offset image from the slit image, thereby reducing the contribution from scattered radiation. We performed a linear regression analysis on the image column maxima to define a line coincident with the center of the slit. The distance to all data points (measured as  $x$ ) was then calculated from this center line at  $x = 0$ . Outlier pixel values, defined as lying 5 standard deviations outside of a local average (comprising  $\sim 1\%$  of the raw data), were removed from the data set, and the remaining pixel values were normalized to a global maximum. Then the pixel values were filtered using a windowed averaging technique to reduce noise (window width = 0.08 pixel). The effects of this filtering on the resulting LSF appeared negligible and were subsequently ignored.

We simulated the experimental data by integrating the Monte Carlo generated  $\text{PSF}^{\text{overall}}$  to obtain the  $\text{LSF}^{22}$  as

$$\text{LSF}^{\text{overall}}(x) = \int_{-\infty}^{\infty} \text{PSF}^{\text{overall}}(x,y) dy. \quad (4.7)$$

The integration was performed numerically, with values of  $\text{PSF}^{\text{overall}}(x,y)$  obtained by interpolation of  $\text{PSF}^{\text{overall}}(r)$ . The LSF was then convolved with a pair of top hat functions – one to account for the finite slit width and the other to account for the pixel width (aperture function).

#### 4.2.6 Other PSF's

A literature survey demonstrates that the techniques used to generate a PSF for clinical dosimetry applications using the aS500 EPID vary. Certainly it is

possible to generate an empirical spread function without the detailed knowledge or analysis described above. Chang and Ling for example assume a Gaussian shape, and determine the adjustable parameters by iterative optimization of the fit between measured and planned dose profiles for an IMRT field.<sup>23</sup> Inspection of the measured line spread function for a similar detector,<sup>24</sup> other Monte Carlo kernels generated for the aS500 EPID,<sup>2,4</sup> and our own PSF<sup>overall</sup>, suggests that the kernel would be better fit by a triple exponential curve. Hence we compare our comprehensive overall kernel with the empirical form,

$$\text{PSF}_{\text{triple exp}}^{\text{overall}}(r) = e^{-P_1 r} + P_2 e^{-P_3 r} + P_4 e^{-P_5 r}. \quad (4.8)$$

The parameters  $P_1$ - $P_5$  were initially determined by fitting the triple exponential to our PSF<sup>overall</sup>. Then they were optimized through an iterative process to yield image-derived fluence values that conformed to diamond detector measured fluence profiles (described below) for a 10×10 cm<sup>2</sup> field, and later a 20×20 cm<sup>2</sup> field. Note that we distinguish a kernel *not* obtained through Monte Carlo simulation with our comprehensive model by a descriptive subscript.

We also consider a ‘thin stack’ kernel that consists of the combination of PSF<sup>dose</sup><sub>thin stack</sub>( $r$ ), a dose kernel based on a simplified model of the EPID, and a fit to our averaged optical spreading kernel [Eq. (4.3)]. The simplified EPID model, analogous to that of Warkentin *et al.*,<sup>4</sup> consists of a water build-up layer (0.5 or 2.0 cm depending on energy), copper plate (0.1cm), phosphor screen (0.034 cm), glass substrate (0.11 cm) and water backing (2.5 cm) layer in intimate contact. We generated PSF<sup>dose</sup><sub>thin stack</sub>( $r$ ) by scoring dose in the same annular bins as for the

comprehensive model, but for the full thickness of phosphor. Based on our optical Monte Carlo results, the averaged optical kernel was assumed to have a single exponential form,  $\langle \text{PSF}^{\text{opt}}(r) \rangle_{\text{fit}} = \exp(-\lambda r)$ . As with the comprehensive kernel,  $\text{PSF}_{\text{thin stack}}^{\text{overall}}(r)$  was obtained as the convolution of its two components. Development of the thin stack kernel was motivated by reports from other authors describing overall kernels obtained from different models of the detector stack. Schach von Wittenau *et al.*<sup>8</sup> developed a “notional” a-Si detector that roughly approximates the aS500, and conducted a Monte Carlo investigation of its blur kernel. McCurdy *et al.*<sup>2</sup> used the EGS4 user code DOSRZ to score the dose response to an incident pencil beam inside the Lanex Fast-B screen of the aS500 detector. The dose distribution was then combined with a double exponential plus delta function glare kernel developed from earlier work by Heijman *et al.*<sup>18</sup> for a video EPID. Warkentin *et al.*<sup>4</sup> used a similar approach, modeling the dose deposition for a simplified detector in XYZDOS, and convolving that result with a glare kernel. The latter was determined empirically by fitting a double exponential function to fluence profile measurements.

#### 4.2.7 Fluence Recovery

All kernels were assessed by the degree to which they successfully deconvolved static field images. We investigated kernel performance first on reference images of an open  $10 \times 10 \text{ cm}^2$  field (defined at isocentre) at 6 and 15 MV, and then on a  $2 \times 2 \text{ cm}^2$  field, a  $20 \times 20 \text{ cm}^2$  field and a  $10 \times 10 \text{ cm}^2$   $45^\circ$  physically wedged field. In all cases the EPID was deployed at 105 cm SDD. It was assumed that variation in the blurring process over the SDD range (105 – 160 cm) was

negligible. We used solid water buildup thickness of 0.5 cm for 6 MV and 2.0 cm for 15 MV.

It is important to note that image pixel values are the result of acquiring a raw image, subtracting a dark field image, and then dividing the result by a flood field image (Sec. 2.2.4).<sup>25</sup> This produces an image that is uniform for an open field, but in doing so washes out the beam profile. In order to recover the profile without re-introducing pixel sensitivity variations we followed the correction technique of Warkentin *et al.*<sup>4</sup> We used the Helax-TMS (MDS Nordion, Kanata, Canada) treatment planning system (TPS) to predict the fluence distribution incident on our detector. The TPS predicted the dose at a depth of 3 cm inside a water phantom of approximate EPID dimensions. Using the same water kernel described in reference 4 the dose was deconvolved to predict the flood field fluence incident on the detector. This result was then convolved with our comprehensive PSF<sup>overall</sup> to generate a simulated flood field image. Each acquired EPID image was subsequently multiplied by the simulated flood field image to yield pixel values  $PV(x,y)$ . Henceforth we refer to this pre-processed image as the “flood field restored image”.

The pixel values  $PV(x,y)$  can be considered a convolution of the incident energy fluence  $\Psi(x,y)$  with the true detector PSF( $x,y$ )

$$PV(x,y) = C \int_{-\infty}^{\infty} \int_{-\infty}^{\infty} \Psi(x',y') \cdot PSF(x-x',y-y') dx' dy' . \quad (4.9)$$

Here  $C$  is a normalization factor that relates the pixel values to the blurred energy fluence distribution in the photodiode plane. In this work  $C$  is not determined

independently, hence our attention is confined to an examination of relative fluence.

Approximating the true detector  $PSF(x,y)$  with our calculated  $PSF^{overall}(x,y)$ , we

inverted Eq. (4.9) to recover  $\Psi(x,y)$  via deconvolution as

$$\Psi(x,y) = \frac{1}{C} FT^{-1} \left\{ \frac{FT\{PV(x,y)\}}{FT\{PSF^{overall}(x,y)\}} \right\}, \quad (4.10)$$

where  $FT$  and  $FT^{-1}$  denote the Fourier transform and its inverse, respectively. Both the original and deconvolved images were normalized to the mean pixel value in a  $1 \times 1$  cm<sup>2</sup> region in the center of the field.

#### 4.2.8 Kernel Performance Evaluation

In order to evaluate kernel performance in recovering incident energy fluence, we compared profiles measured using the EPID with those measured using a PTW diamond detector<sup>26,27</sup> type 60003 (PTW Freiburg, Germany) with 1.7 cm (15 MV) and 1.1 cm (6 MV) diameter brass buildup caps and Wellhofer's Blue Phantom scanning apparatus (Wellhofer Dosimetrie, Schwarzenbruck, Germany). A similar comparison has been made by other authors.<sup>4</sup> The apparatus was set up to scan in the cross-plane and in-plane directions through the central axis at the same SDD as the EPID's imaging plane (106.3 cm). The diamond detector was oriented along the gantry axis. Corresponding EPID data was obtained by extracting a line of pixels in the middle of each field. The field edges were determined using the MATLAB (Mathworks Inc., Natick, MA) edge detection function. The diamond detector and EPID profiles were then aligned using a shift-correction that minimized the displacements between points having 50% of maximum intensity, yielding a

maximum error in profile overlap of a single pixel width. It should be noted that the profiles measured with the diamond detector are themselves blurred because of the finite size of the detector plus buildup cap, an effect which becomes most relevant when comparing small fields, *ie.*  $2 \times 2 \text{ cm}^2$ . In order to give a true measure of the relative fluence, the diamond detector profiles would also need to be deconvolved with an appropriate detector response function.

For quantitative comparisons, we used the  $\chi$  evaluation technique proposed by Bakai *et al.*,<sup>28</sup> which is based on the  $\gamma$  evaluation concept of Low *et al.*<sup>29</sup> In the  $\chi$  technique, a multi-dimensional ellipsoid of acceptance is defined by  $\Delta D_{\max}$  – the maximum acceptable dose difference at a point, and  $\Delta d_{\max}$  – the maximum acceptable distance-to-agreement. For values of  $|\chi| \leq 1$ , the difference in two dose distributions is considered to be acceptable. In our comparisons we chose  $\Delta D_{\max} = 2\%$  (of the signal at the central axis), and  $\Delta d_{\max} = 0.0784 \text{ cm}$  (one pixel width). Reported  $\chi$  scores compare profile data only; measurements over the entire EPID imaging plane were not obtained with the diamond detector. In general, two numbers are reported for the fraction of  $\chi$  scores  $< 1.0$  corresponding to each case considered. The first compares the relative EPID dose in the flood field corrected image profile (blurred) to the relative in air dose profile measured by the diamond detector (approximating fluence). The second compares the relative EPID profile after deconvolution (a better approximation to fluence obtained from the EPID image) to the same diamond detector profile.

#### 4.2.9 *Diamond Detector Response Function and Fluence Recovery*

It is important to note that the majority of diamond detector profiles presented have not been subjected to a deblurring process themselves. Traditionally this has been justified by the small active volume of the detector ( $0.0014 \text{ cm}^3$ ), however, these measurements are not free from volume averaging effects as our results will demonstrate. As a follow up investigation, we modeled a blur kernel for our diamond detector in the dose measurement configurations outlined above. Using DOSRZnrc, we first developed an edge response function, and from this we derived a one-dimensional blur kernel. We then deconvolved a raw diamond profile to recover the relative incident fluence, which allowed us to gauge the significance of ignoring this step.

Based on the information available in the operator's manual,<sup>26</sup> we developed a rudimentary model of the diamond detector that consisted of a brass buildup cap ( $\text{Cu}_3\text{Zn}_2$ ,  $\rho = 8.6 \text{ g/cm}^3$ ), a central volume containing the diamond (modeled as carbon,  $\rho = 3.5 \text{ g/cm}^3$ ), and a water filler that approximated the structural materials in the rest of the detector volume. The brass buildup cap had a length of 2.0 cm, a diameter of 1.1 or 1.7 cm, and a thickness of 0.185 or 0.485 cm corresponding to the 6 or 15 MV setup, respectively. The diamond was modeled with a diameter of 0.240 cm and a thickness of 0.031 cm, and was centered on the z-axis 0.1 cm beneath the buildup cap. Signal wires were not incorporated into the model.



Although DOSRZnrc is published with a variety of source options, none are sufficient for modeling an edge response function. Essentially, we needed to score the dose to the diamond detector as it traversed a radiation field boundary (contributions from photons scattered in air beside the buildup cap are neglected). To accomplish this, a broad parallel beam incident from the side (positive y-axis, ISOURCE = 10) was simulated. Both the 6 MV and 15 MV spectra were the same as those used to generate  $\text{PSF}^{\text{rad}}$ . The x and z beam parameters were defined to match the dimensions of the diamond detector model projected on the x-z plane. We then modified the published code to include a parameter XSHIFT – a translation in the x-direction of photon coordinates – immediately before entering the SHOWER subroutine. XSHIFT was increased stepwise for successive simulations in increments of 0.05 cm until the cumulative translation was such that no incident photons struck the edge of the brass buildup cap. This produced the diamond detector’s edge response function  $\text{ERF}_{\text{DD}}(x)$ .

The derivative of the edge response function is the line spread function,<sup>30</sup> which for a scanning “point” detector is a blur kernel,  $\text{LSF}_{\text{DD}}(x)$ ,

$$\text{LSF}_{\text{DD}}(x) = \frac{d}{dx} \text{ERF}_{\text{DD}}(x), \quad (4.11)$$

or numerically,

$$\text{LSF}_{\text{DD}}(x_i) \approx \frac{\text{ERF}_{\text{DD}}(x_{i+1}) - \text{ERF}_{\text{DD}}(x_{i-1})}{x_{i+1} - x_{i-1}}. \quad (4.12)$$

Because the blur kernel is symmetric in the x-dimension (as modeled), we averaged corresponding data values on either side of the center line to reduce statistical fluctuations in the results.

To recover the fluence incident on the diamond detector, we performed the same operation outlined in section 4.2.7 (Eqn. 4.10), only limited to the x-dimension. We initially concentrated on the diamond detector profile measured in the cross-plane direction through a 6 MV  $10 \times 10 \text{ cm}^2$  field in order to understand the difference incorporating this operation would have on our results. We then extended the investigation to include a cross-plane profile through a 6 MV  $2 \times 2 \text{ cm}^2$  field, where previously the flood field corrected EPID data (without deconvolution) had resulted in a sharper profile than that measured with the diamond detector.

## 4.3 RESULTS AND DISCUSSION

### 4.3.1 *Dose Deposition Kernel*

#### 4.3.1.1 *Depth Dose in Scintillation Screen*

Figure 4.4 depicts the depth dose scored in a 0.0784 cm diameter radial bin for both 6 and 15 MV beams. These curves demonstrate the degree of nonuniformity of dose deposited across the thickness of the phosphor by the pencil beam, and exhibit both a buildup region and a falloff region. The maximum dose occurs at a depth of 0.0136 cm for the 6 MV beam and 0.0170 cm for the 15 MV beam. There is a 28%

difference between the maximum and minimum doses at 6 MV, and a 17 % difference at 15 MV.

#### 4.3.1.2 Pencil Beam Response in Scintillation Screen

Figure 4.5 shows the behaviour of  $\langle \text{PSF}^{\text{rad}}(r) \rangle$ , the dose in the full thickness of the phosphor, at 6 and 15 MV. Energy differences in primary electron transport result in close range ( $< 5$  cm) differences in these dose PSFs. The relative dose in the ‘tails’ contributed by scattered photons is lower for 15 MV than for 6 MV. For both beam energies the curves are observed to drop eight orders of magnitude at a radial distance of 30 cm. The central scoring bin yielded an average dose per history of  $(2.12 \pm 0.04) \times 10^{-16}$  Gy and  $(1.52 \pm 0.03) \times 10^{-16}$  Gy for the 6 and 15 MV beams, respectively. The average dose per history scored inside a 30 cm radius circle was  $(8.57 \pm 0.03) \times 10^{-23}$  Gy at 6 MV and  $(1.194 \pm 0.004) \times 10^{-22}$  Gy at 15 MV. The uncertainties are standard deviations calculated from subsets of 10 runs, each having  $1/10^{\text{th}}$  the total number of histories.

#### 4.3.2 Optical Spreading Kernel

Figures 4.6 and 4.7 depict results from the DETECT2000 simulations. Figure 4.6 shows the total number of optical photons incident on the photodiode layer as a function of the depth of emission within the phosphor. Relative contributions from each phosphor layer increase in a roughly linear fashion as the photodiode layer is approached. Given the broader distribution of detected photons emerging from the upper layers (see Fig. 4.7), it appears that the contribution to the overall optical

fluence from these layers is not entirely negligible. Kausch *et al*<sup>31</sup> estimated a total escape probability of 70 % for photons 50  $\mu\text{m}$  from the photodiode plane within a 1 mm thick phosphor, whereas we calculated a value for photons 51  $\mu\text{m}$  from the filter (about the same depth in the phosphor) of only about 6 %. It is important to note that in our EPID model, the optical filter significantly reduces the number of photons reaching the photodiode plane.

In Fig. 4.7 we present the relative optical fluence as a function of radial distance from emission points located in the first ( $z = 0.0017$  cm) and tenth ( $z = 0.0323$  cm) phosphor layers, as well as two intermediate layers. The curves exhibit an initial shoulder and fall off exponentially beyond 0.04 cm ( $\sim 1/2$  pixel width) with very similar exponential decay coefficients. As depth in the phosphor increases, a distinct peak centered at the origin emerges due to an increasing contribution from non-scattered optical photons. The average response kernel defined in Eq. (4.3) was fit using a single exponential function,  $\langle \text{PSF}^{\text{opt}}(r) \rangle_{\text{fit}} = \exp(-\lambda r)$ . Due to the different CAX depth dose curves (see Fig. 4.4), there is a slight dependence of the fit on beam energy. Regression analysis yielded values of  $\lambda = 49.3$   $\text{cm}^{-1}$  and  $\lambda = 49.5$   $\text{cm}^{-1}$  for the 6 and 15 MV beams, respectively, with a squared correlation coefficient of 0.999 for each case. The results are shown in figure 4.8.

### 4.3.3 Overall Blur Kernel

The overall blur kernels obtained by combining the dose and optical kernels are presented in figure 4.9. We see that the curves are generally similar in shape to

corresponding dose kernels for the full thickness of phosphor (Fig. 4.5). The 15 MV curve is broader inside a 5 cm radius, but tends to exhibit behavior similar to the 6 MV curve in the tail. As observed by previous investigators,<sup>8</sup> the inner broadness of the 15 MV kernel is primarily due to lateral electron transport. Dose deposition simulations done with electron transport turned off confirm this. Also shown for reference in figure 4.9 is  $\langle \text{PSF}^{\text{rad}} \rangle$  for the 6 MV beam. Incorporating optical spreading noticeably broadens the overall kernel. 6 MV kernels for different thicknesses of the solid water backscatter (2.5, 1.5 and 0.0 cm) are shown in figure 4.9 (c) to gauge the relative contributions of the optical spreading and backscatter. Note that the 0.0 cm case did not include the rear housing material of the detector, which was present for the 1.5 and 2.5 cm solid water cases. Modeled backscatter contributions manifest outside a radius of  $\sim 1$  cm and appear to contribute to the broadening of the overall kernel with roughly the same magnitude as optical spreading in the tail regions.

#### 4.3.4 Comparison with Experimental LSF

Figures 4.10 and 4.11 show the processed images analyzed, as well as the raw slit and offset images acquired to measure the LSF for the 6 MV and 15 MV photon beams, respectively. The images have been magnified by a factor of 2.5 to give a better view of the slit region. Figure 4.12 compares the simulated LSFs to our experimental data, which is plotted to a maximum distance from the center of the slit of 1.2 cm (15 pixels). A windowed average (spanning 20 data points) was fit to the data points to help quantify the differences. Both the 6 and 15 MV simulation results

agree quite well with the experimental data. At a radial distance of 2.5 pixels we observe the largest differences of 0.9% and 1.2% of the central value for the 6 and 15 MV beams, respectively. These small differences likely arise from uncertainties inherent in our Monte Carlo model (*i.e.* the assumption of a uniform water slab for backscatter, a spatially invariant incident photon spectrum,<sup>14</sup> and a point x-ray source) as well as limitations in the experimental method (*i.e.* scatter from the lead blocks forming the slit, and non-uniformity in slit width). Beyond a distance of 15 pixels from the center of the slit, it becomes difficult to distinguish the EPID signal from the background noise.

#### 4.3.5 Energy Fluence Recovery

Figure 4.13 depicts cross-plane and in-plane profiles for a 6 MV  $10 \times 10 \text{ cm}^2$  field generated by deconvolution with  $\text{PSF}^{\text{overall}}$ , plotted along with flood field restored image profiles and diamond detector profiles. In figure 4.14, the magnitudes of the  $\chi$  scores are shown as functions of cross-plane and in-plane distance. As expected, the differences between flood field restored image and diamond detector profiles are significantly reduced. The largest reductions occur outside the field and close to the field edges. The deconvolved EPID image profiles have sharper edges than the diamond profiles. This is due to the volume averaging in the diamond detector buildup cap. Inclusion of the optical kernel provides better agreement with the measured profile. In Fig. 4.13 (c) we show the cross-plane geometry again where the deconvolution has been performed with  $\langle \text{PSF}^{\text{rad}} \rangle$ . Although perhaps not obvious at first, the difference becomes apparent in Fig. 4.13 (d), where we focus on the

exterior portion of the penumbra where the deconvolution has been performed both with  $\text{PSF}^{\text{overall}}$  and  $\langle \text{PSF}^{\text{rad}} \rangle$ . In figure 4.15 we present histograms of the  $\chi$  scores for the profiles in figure 4.13. With deconvolution using  $\text{PSF}^{\text{overall}}$  there is a substantial increase in the fraction of acceptable  $\chi$  scores, from 49.0 % to 92.0 % for the cross-plane profile, and from 43.4 % to 89.9 % for the in-plane profile. Post-deconvolution  $\chi$  values  $> 1.0$  are mainly attributable to differences in the high gradient regions at the field edges. When the deconvolution is performed using  $\langle \text{PSF}^{\text{rad}} \rangle$  there is almost no change in acceptance results using our chosen parameters ( $\Delta D = 2\%$ ,  $\Delta d = 0.0784$  cm). When the parameters are tightened ( $\Delta D = 1\%$ ,  $\Delta d = 0.0784$  cm),  $\chi$  values  $> 1.0$  after deconvolution are reduced to 78.6 % for  $\text{PSF}^{\text{overall}}$  and 66.1 % for  $\langle \text{PSF}^{\text{rad}} \rangle$ .

A  $10 \times 10$  cm<sup>2</sup> field at 15 MV was also examined, where the differences between the flood field restored image (before deconvolution) and diamond detector profiles are greater than at 6 MV. Deconvolution in this case increased the proportion of  $\chi$  scores  $< 1.0$  from 37.4 % to 83.3 %. The 15 MV result did not reach the same degree of acceptance as the corresponding 6 MV case for several reasons: there were fewer values already in the acceptance range at 15 MV, there was more noise in the 15 MV image, and the detector response function was not deconvolved from the diamond detector profile (15 MV measurements were made with a thicker buildup cap, hence were blurred more).

Kernel performance across a range of field sizes was assessed by considering  $2 \times 2 \text{ cm}^2$  and  $20 \times 20 \text{ cm}^2$  fields. Quantifying performance for the  $2 \times 2 \text{ cm}^2$  field proved difficult since the diamond detector buildup cap blurs the incident fluence over a significant fraction of the field width. A follow-up study examining diamond detector blur and which includes this field is presented in section 4.3.7. For the  $20 \times 20 \text{ cm}^2$  field at 6 MV the number of  $\chi$  scores  $< 1.0$  increased from 43.1 % to 96.0 %. There is a slight under-response ( $\sim 1\%$ ) as compared to the diamond detector profile outside the field edges. For this larger field, the photon spectrum is known to change with radial distance.<sup>14,32</sup> Our work did not attempt to model variations in the kernel with distance from the central axis, however, as the flood field correction process (section 2.2.4) already compensates for off-axis spectral effects to a large degree.

We also considered a  $10 \times 10 \text{ cm}^2$   $45^\circ$  physically wedged field at 6 MV, the fluence profile for which is depicted in figure 4.16. The improvement seen in the measurement after deconvolution with  $\text{PSF}^{\text{overall}}$  is not as substantial as for the corresponding open field; the fraction of  $\chi$  scores  $< 1.0$  increased from 40.3% to 73.9%. Noise in the diamond detector profile is  $\sim 5\%$ . On the right hand edge of the field we see that deconvolution results in an over-response. Because the phosphor energy response is non-uniform<sup>28</sup> and the beam is harder in this more heavily attenuated portion of the field, it is likely that the open field kernel used in deconvolution is overcompensating. The inaccuracies introduced in the open field cases by ignoring beam spectrum changes off-axis beyond those addressed by flood correction are expected to be considerably smaller in magnitude.



#### 4.3.6 Other PSF's

The triple exponential kernel fit parameters are shown in table 4.1 along with  $\chi^2$  values<sup>10</sup> indicating the goodness of fit to our comprehensive kernels. For an open  $10 \times 10 \text{ cm}^2$  field at 6 MV the deconvolution using the triple exponential kernel improved  $\chi$  scores  $< 1.0$  to 90.3 % – approaching the value of 92.0 % obtained with the comprehensive kernel. Similar results were found for the 15 MV case (see table 4.2). It was possible to manipulate the kernel's parameters to improve the kernel's performance for a specific field size (*ie.* we were able to obtain 92.6 % of  $\chi$  scores  $< 1.0$  for a  $10 \times 10 \text{ cm}^2$  field), but this resulted in decreased performance for the other field size investigated. It is therefore important to keep in mind that when an analytical function is used to represent the PSF, fit parameters should be derived from a consideration of the kernel's performance across the intended application range of field sizes, rather than for a single field.

PSF<sub>thin stack</sub><sup>overall</sup> also performed quite well. In comparison with the other kernels for the 6 MV beam (Fig. 4.17) it exhibited a steeper falloff in the tail, but this did not appear to greatly affect its performance for our agreement criteria. At 6 MV for a  $10 \times 10 \text{ cm}^2$  field the percentage of  $\chi$  scores  $< 1.0$  was 93.0 %, and for a  $20 \times 20 \text{ cm}^2$  field, 92.0 %. Other authors have used empirically determined “glare” kernels in combination with Monte Carlo calculated dose kernels for simplified detector

---

<sup>11P</sup> The  $\chi^2$  statistic here should *not* be confused with the  $\chi$  score described previously in this paper.

Here  $\chi^2 = \sum_{i=1}^N \frac{(F_i - E_i)^2}{\sigma_i}$ , where  $F_i$  and  $E_i$  are the fitted and expected (comprehensive simulation) PSF values,

respectively.  $\sigma_i$  is the standard error in the expected value, which has been approximated as the standard deviation in the dose kernel points.

models.<sup>2,4</sup> Our result for  $\langle \text{PSF}^{\text{opt}} \rangle$  suggests that only a portion of these glare kernels can be attributed to optical spreading, and that the remainder (such as a second exponential term) is needed to compensate for missing contributions to the dose kernel.

#### 4.3.7 *Diamond Detector Response Function and Fluence Recovery*

The follow-up investigation allowed us to calculate blur kernels ( $\text{LSF}_{\text{DD}}(x)$ ) for the diamond detector in 6 and 15 MV photon beams, which were then used to deconvolve selected beam profiles. The Monte Carlo generated diamond detector blur kernels are shown in Fig. 4.18. These kernels were found to have a FWHM of 0.27 cm and 0.29 cm for the 6 and 15 MV beams, respectively. Statistical uncertainties in the edge response function data were  $\sim 2\%$  and their propagation resulted in the error bars in the figure.

In Fig. 4.19 we present the resulting diamond detector measured fluences where the profiles have been subject to deconvolution using  $\text{LSF}_{\text{DD}}(x)$ . Fig. 4.19(a) considers the cross-plane profile for a 6 MV  $10 \times 10 \text{ cm}^2$  field, corresponding to that shown in Fig. 4.13 (a). Comparing the two figures, it is apparent that the resulting diamond fluence is sharper after deconvolution. However, the improvement does not appear to be significant when assessed using our (2%, 0.0784 cm) agreement criteria. The percentage of  $\chi$  scores  $\leq 1$  with the deconvolved diamond profile improves from 46.2% to 89.7%, versus an improvement from 49.0% to 92.0% without deconvolution. With tighter criteria (1%, 0.0784 cm) the percentage of  $\chi$  scores  $\leq 1$

with the deconvolved diamond profile improves from 20.9% to 75.9%, versus an improvement from 20.6% to 66.1% without deconvolution. This suggests that for the  $10 \times 10 \text{ cm}^2$  and  $20 \times 20 \text{ cm}^2$  fields presented in this study, deconvolving the diamond profiles would not have a significant effect on the reported  $\chi$  scores using the (2%, 0.0784 cm) criteria. It is possible that we may observe a larger difference in the  $\chi$  scores reported when the EPID image deconvolution is performed with  $\langle \text{PSF}^{\text{rad}} \rangle$  indicating a stronger effect resulting from incorporating the optical spreading in the  $\text{PSF}^{\text{overall}}$ .

In figure 4.19(b) and (c) we present a small field case, showing cross-plane profiles for a 6 MV  $2 \times 2 \text{ cm}^2$  field after, and prior to, deconvolution of the diamond detector profile, respectively. In (c) there is a notable sharpening of the EPID profile after deconvolution of the EPID image, but the flood field corrected image profile is already considerably sharper than the diamond detector profile, so a quantitative comparison using the  $\chi$  method indicates that EPID image deconvolution affords little improvement. With the diamond profile deconvolved, the true effect of deconvolving the EPID image is now apparent. The percentage of  $\chi$  scores  $\leq 1$  improves from 96.0% to 99.2%. Thus it can be seen that the volume averaging effect present in the diamond detector measurements becomes increasingly more significant for smaller field sizes.

#### 4.4 SUMMARY AND CONCLUSIONS

By comprehensively simulating the processes of dose deposition within the scintillation screen of the aS500 EPID and spreading of optical photons arriving at the photodiode plane, we were able to derive overall blur kernels for 6 and 15 MV photon beams consistent with EPID LSF measurements. The kernels were implemented in a deconvolution process that yielded relative energy fluence measurements from EPID images for a variety of static fields. Using the  $\chi$  metric, we compared deconvolution results to energy fluence measurements made using a diamond detector. We saw a dramatic improvement in EPID relative energy fluence profiles after deconvolution, with  $\chi$  scores  $> 1.0$  generally limited to high gradient regions where volume averaging effects influenced the diamond detector readings. Agreement within 2 % relative fluence or 0.0784 cm distance to agreement was consistent across a range of field sizes, in both the cross- and in-plane directions. The influence of the optical kernel was found to be negligible for these  $\chi$  acceptance parameters, but for tighter parameters ( $\Delta D = 1\%$ ,  $\Delta d = 0.0784$  cm) it resulted in an improvement from 66.1% (without the optical kernel) to 78.6% (with the optical kernel) of  $\chi$  scores  $< 1$  (from 20.6 % before deconvolution). The comprehensive kernels are a limited representation of physical reality insofar as the spectrum from which they were derived was a generic CAX spectrum for a Varian linac, assumed to be emitted from the x-ray focal spot and invariant as a function of radius. In the situation where a steel wedge modifies the incident spectrum across the field, the kernel does not perform as well as for open fields. Furthermore, the assumption of a spatially invariant kernel may also be weakened somewhat by electrical cabling and support

structures below the apparatus that result in non-uniform backscatter contributions to dose in the phosphor, an issue recently addressed by Ko *et al.*<sup>7</sup>

There are several approaches to obtaining a blur kernel for a-Si EPID-based dosimetry applications. Using a simple analytical function to approximate the kernel offers the advantages of being quick to implement and flexible in permitting adjustment of parameters to optimize performance. We found that a triple exponential form, which could be determined by entirely empirical means, closely approximated our comprehensive  $\text{PSF}^{\text{overall}}$  and was able to closely match the performance of our comprehensive kernel. Combining a dose kernel derived from a simplified model of the EPID with an empirical optical kernel seems to bridge the gap between empirical estimation and full simulation. Monte Carlo simulation of the dose deposition in the phosphor layer ensures that the major portion of the physics controlling the shape of the PSF is accurately modeled. An empirically derived optical spreading kernel then characterizes the spread of optical photons, but in addition may compensate for inaccuracies in the radiation transport simulation.

The comprehensive simulation presented here provides additional insight into the physical processes contributing to the overall blur kernel for a commercial a-Si EPID. The optical part of the kernel, frequently modeled as a double exponential function, was found to exhibit a falloff best described by a single exponential, and to demonstrably broaden the overall PSF. Apart from an overall constant appearing in the deconvolution formula [Eq. (4.10)], the blur kernel obtained from a full

simulation of the image formation process did not incorporate any free parameters, yet performed very well in recovering incident energy fluence for a range of static field sizes at both 6 and 15 MV. Consequently, the full simulation approach described here appears suitable for generating PSF's that could be used as clinical standards for different EPID designs. Lastly, in a follow-up investigation we quantified the blur arising from volume averaging in our diamond detector measurements, and removed it from selected beam profiles. It was demonstrated that for the (2%, 0.0784 cm) acceptance criteria, the consequences of this operation for the majority of results presented here are minimal. A notable exception was that deblurring the diamond profile for a  $2 \times 2 \text{ cm}^2$  field resulted in improved  $\chi$  scores after EPID image deconvolution, which previously was not the case. This result confirms the notion that deblurring diamond detector profiles can be important for very small fields.

Form	$P_1$ (cm <sup>-1</sup> )	$P_2$	$P_3$ (cm <sup>-1</sup> )	$P_4$	$P_5$ (cm <sup>-1</sup> )	$\chi^2$ (fit to PSF <sup>overall</sup> )
PSF <sup>overall</sup> <sub>triple exp</sub> <sub>6MV</sub>	25.0	8.0E-04	2.0	1.7E-05	0.18	0.075
PSF <sup>overall</sup> <sub>triple exp</sub> <sub>15MV</sub>	23.0	2.5E-03	1.7	8.0E-06	0.18	0.589

**Table 4.1.** Parameter values determined empirically for the triple exponential form of the PSF.

Kernel	Energy (MV)	Field Size (cm <sup>2</sup> )	Profile Direction	Field	Before Deconvolution	After Deconvolution
PSF <sup>overall</sup>	6	10 × 10	cross-plane	open	49.0	92.0
PSF <sup>overall</sup>	6	10 × 10	in-plane	open	43.9	89.9
PSF <sup>overall</sup>	15	10 × 10	cross-plane	open	37.4	83.3
PSF <sup>overall</sup>	6	20 × 20	cross-plane	open	43.1	96.0
PSF <sup>overall</sup>	15	20 × 20	cross-plane	open	22.8	85.8
PSF <sup>overall</sup>	6	10 × 10	cross-plane	wedged 45°	40.3	73.9
$\langle \text{PSF}^{\text{rad}} \rangle$	6	10 × 10	cross-plane	open	20.6*	66.1*
PSF <sup>overall</sup>	6	10 × 10	cross-plane	open	20.6*	78.6*
PSF <sup>overall</sup> <sub>triple exp</sub>	6	10 × 10	cross-plane	open	49.0	90.3
PSF <sup>overall</sup> <sub>triple exp</sub>	6	20 × 20	cross-plane	open	43.1	96.2
PSF <sup>overall</sup> <sub>triple exp</sub>	15	10 × 10	cross-plane	open	37.4	84.4
PSF <sup>overall</sup> <sub>triple exp</sub>	15	20 × 20	cross-plane	open	22.8	88.0
PSF <sup>overall</sup> <sub>thin stack</sub>	6	10 × 10	cross-plane	open	49.0	93.0
PSF <sup>overall</sup> <sub>thin stack</sub>	6	20 × 20	cross-plane	open	43.1	92.0

**Table 4.2.** A summary of the percentage of  $\chi$  scores < 1.0 (in last two columns) corresponding to the different kernels and parameters investigated in this work. The acceptance criteria were defined as a distance to agreement of 0.0784 cm and a dose difference of 2% of the central axis value. Values marked with an asterisk used a smaller dose difference of 1%.

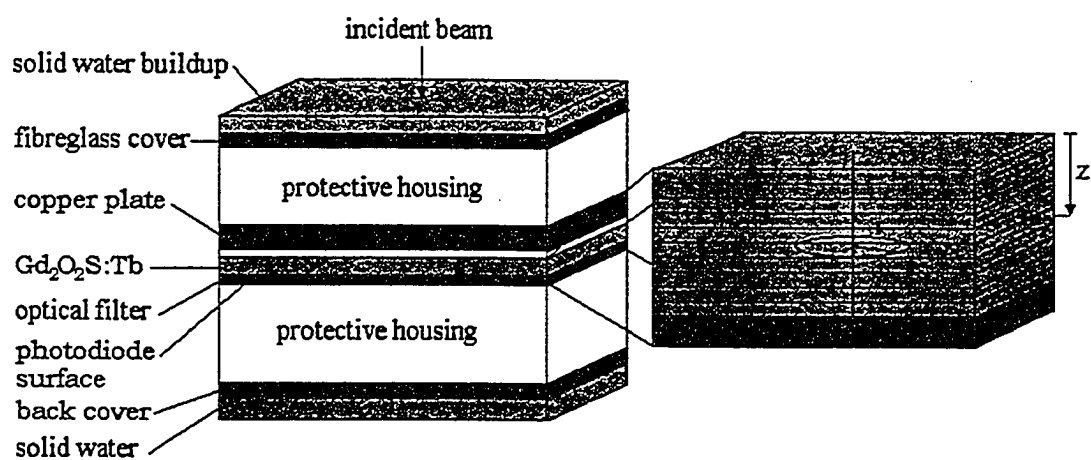


**Figure 4.1.** The principal components of the EPID detector stack. Additional supporting structures and substrate materials such as glass, foam, paper and fibreglass are also present. The pencil beam is incident on the top surface of the buildup layer. The phosphor is divided into 10 equal layers defined by discrete values of  $z$ .



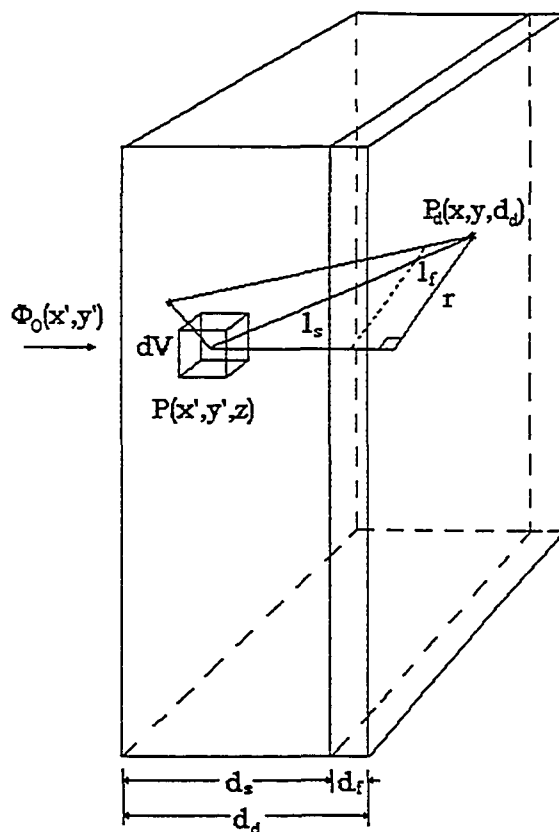


**Figure 4.2.** Geometry considered for the optical component of signal spreading: Optical photons are produced with an isotropic distribution in the scintillation screen (s) at point  $P(x', y', z)$ , and travel through the screen and through the optical filter (f) until they strike the photodiode surface (d) at a point  $P_d(x, y, d_d)$ . Two possible optical photon paths are illustrated.

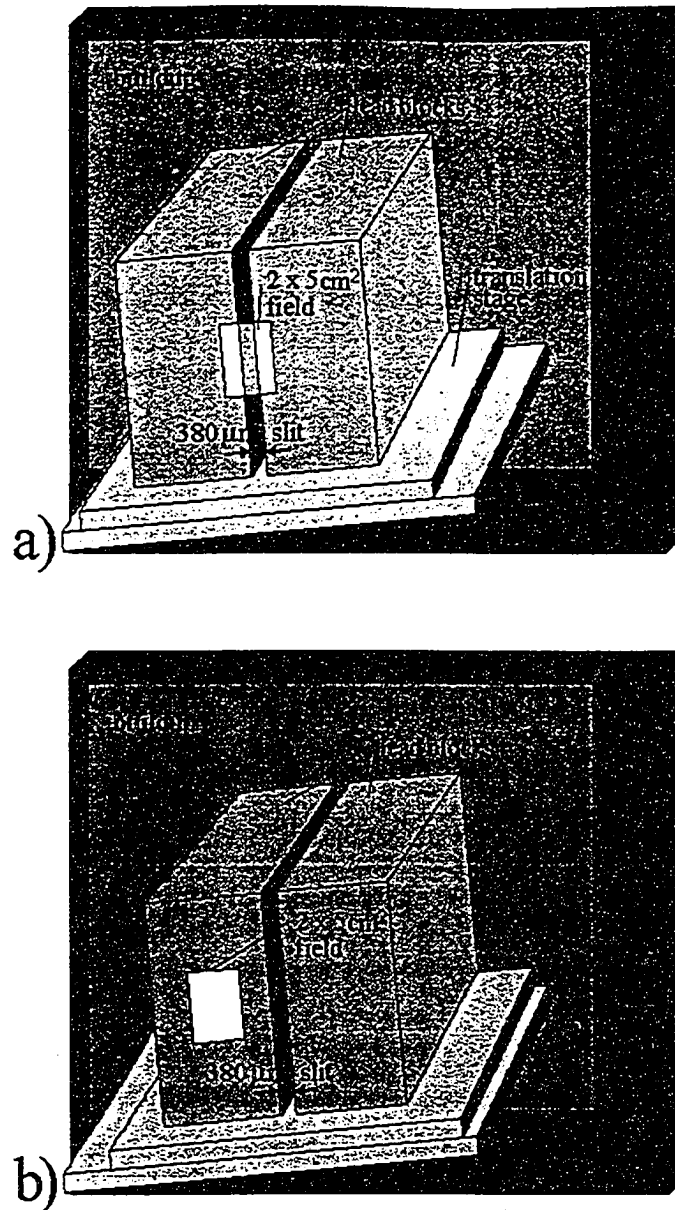


**Figure 4.3.** The apparatus used to measure the LSF. A  $2 \times 5 \text{ cm}^2$  field is projected onto a  $380 \mu\text{m}$  slit to form the slit image at an angle of  $1.7^\circ$  (a). Subsequently the lead blocks are laterally translated  $\sim 2 \text{ cm}$  on the translation stage such that the field does not pass directly through the slit, thereby forming an offset image (b).

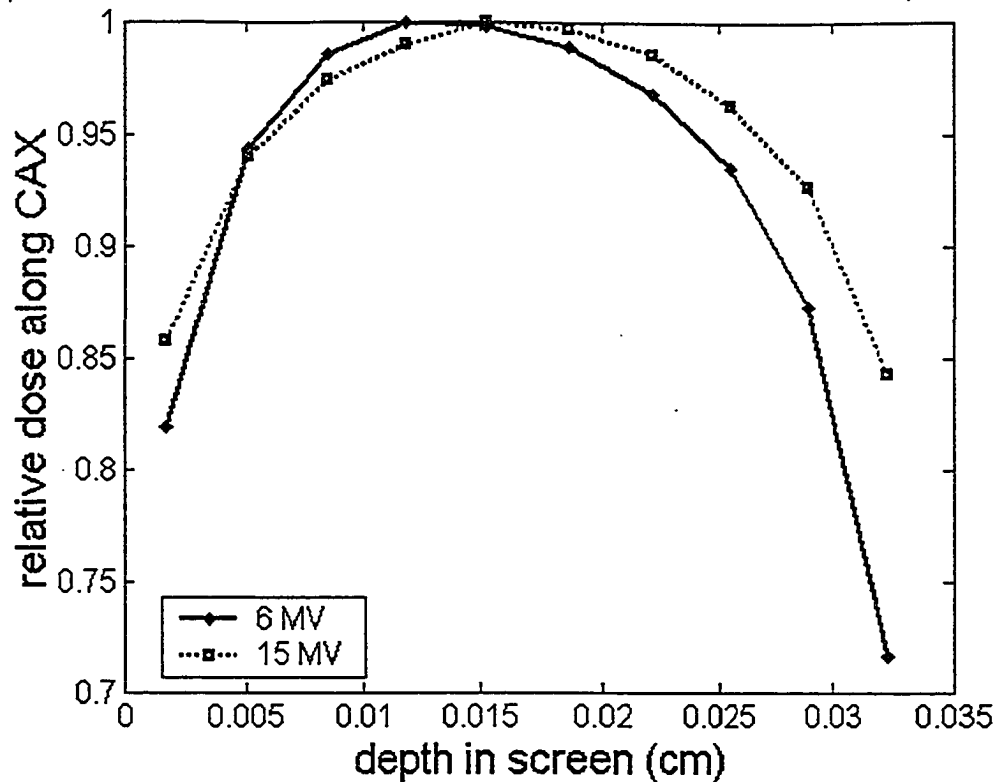


**Figure 4.4.** Relative dose deposited along the CAX in the EPID scintillation screen. The dose deposited in a 0.0784 cm diameter radial bin for each of the ten layers is normalized to the layer having maximum dose. The figure illustrates the presence of dose buildup and fall-off within the screen in response to an incident pencil beam of photon radiation.

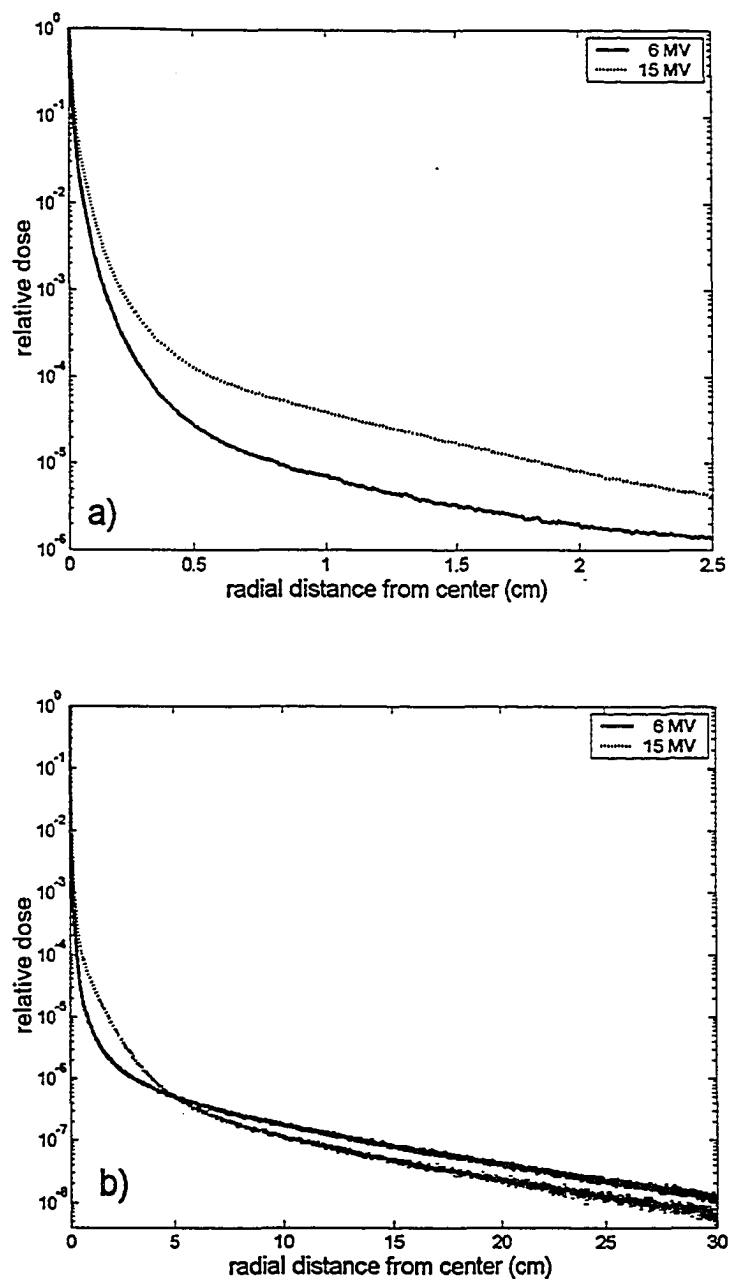


**Figure 4.5.** The relative dose in the full thickness of phosphor as a function of near radial distance (0-2.5 cm) (a) and far radial distance (0-30 cm) (b) from the point of incidence of a  $10\ \mu\text{m}$  wide pencil beam. Both the 6 and 15 MV beam responses have been normalized to unity in the central scoring bin.

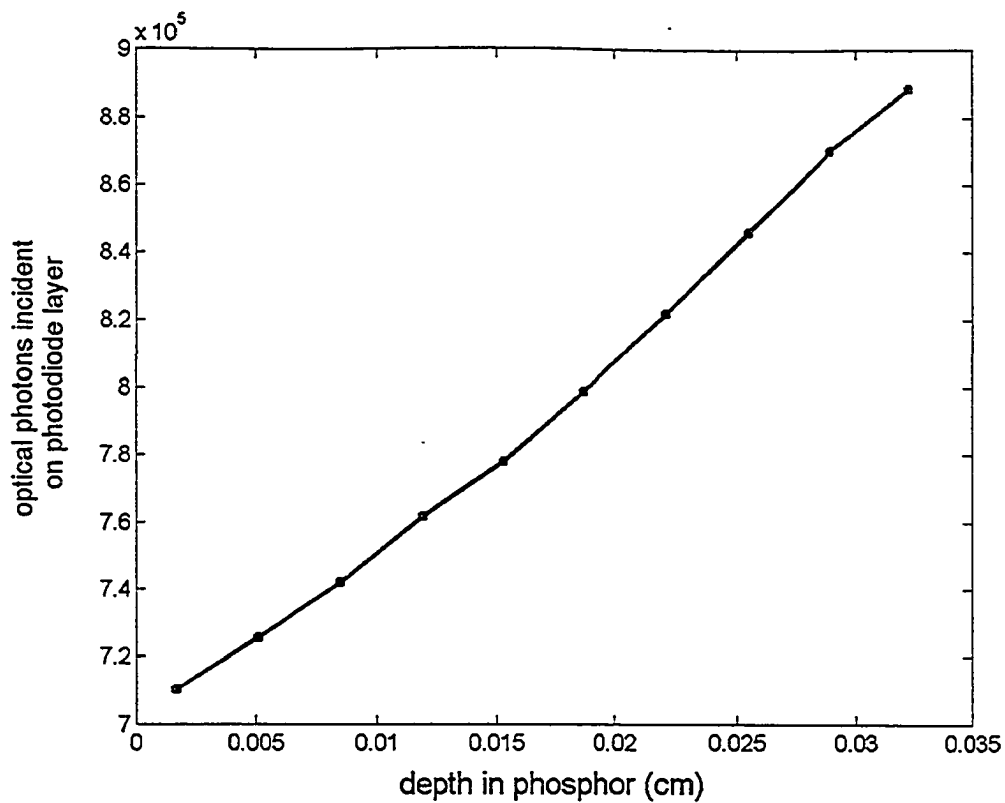


**Figure 4.6.** The total number of optical photons scored on the exit surface of the optical filter as a function of the depth of the point of emission within the scintillation screen.  $1.5 \times 10^7$  photons were initiated at each emission point.

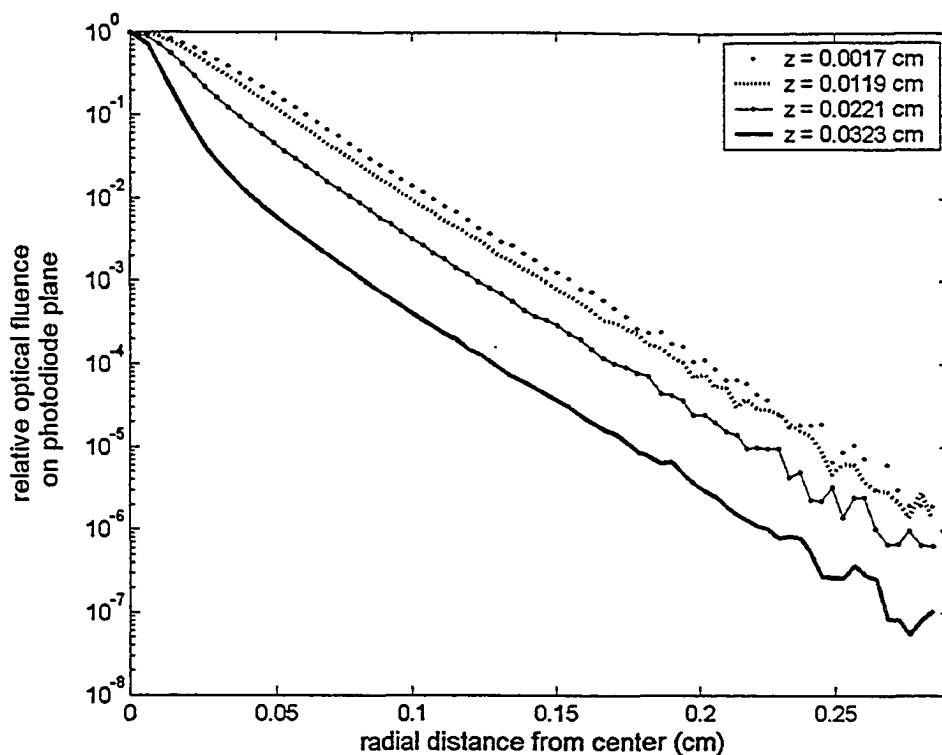


**Figure 4.7.** The relative optical fluence reaching the photodiode plane as a function of radial distance, for four different emission depths. This set of four curves is a sample of the ten produced in this study. A distinct shoulder emerges on the curves for emission depths closest to the detection plane due to an increasing contribution from non-scattered optical photons.

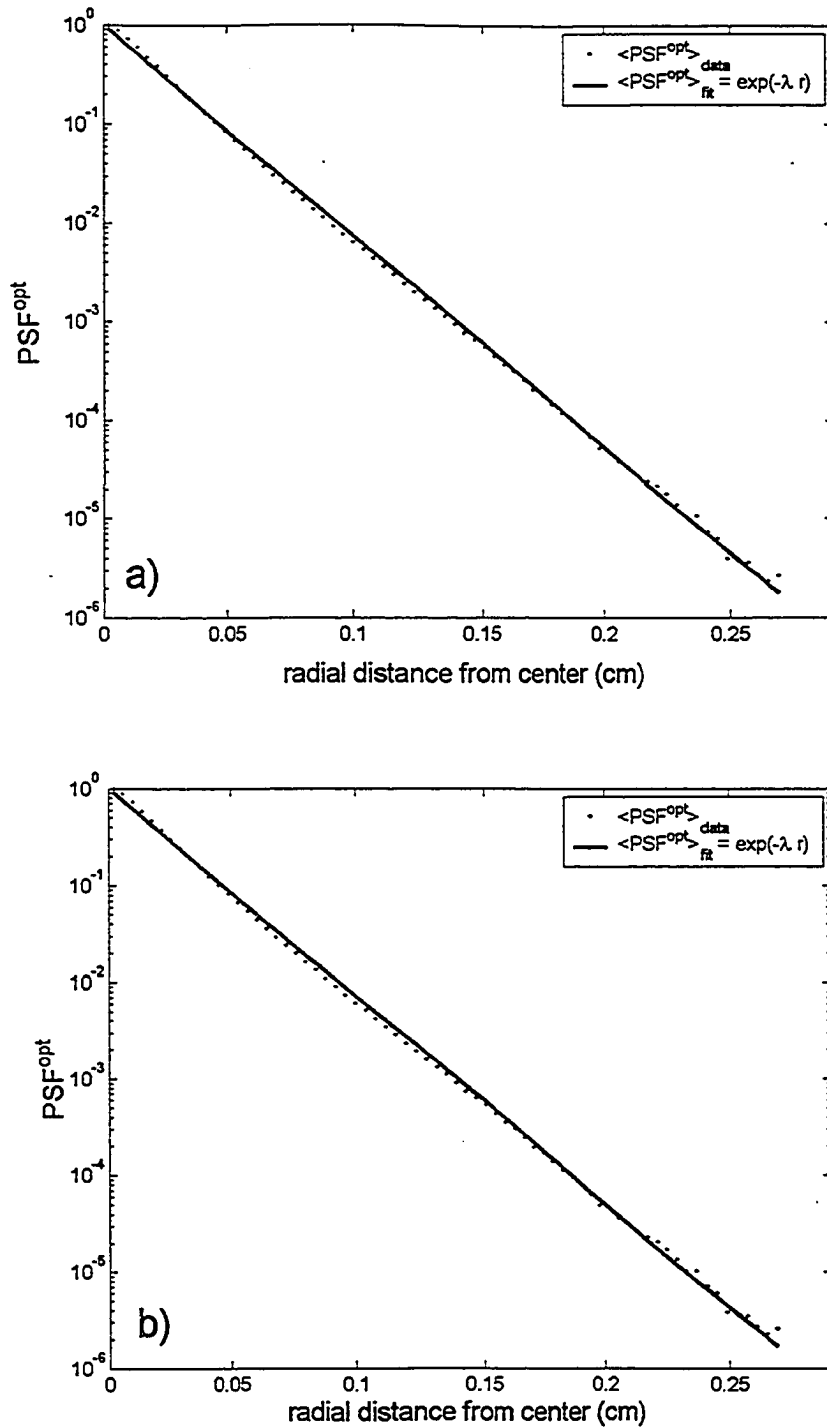


**Figure 4.8.**  $\langle \text{PSF}^{\text{opt}} \rangle$  for 6 MV (a) and 15 MV (a) beams. Single exponential fits to the data with attenuation coefficients  $\lambda = 49.3$  and  $49.5 \text{ cm}^{-1}$ , respectively, are also shown.

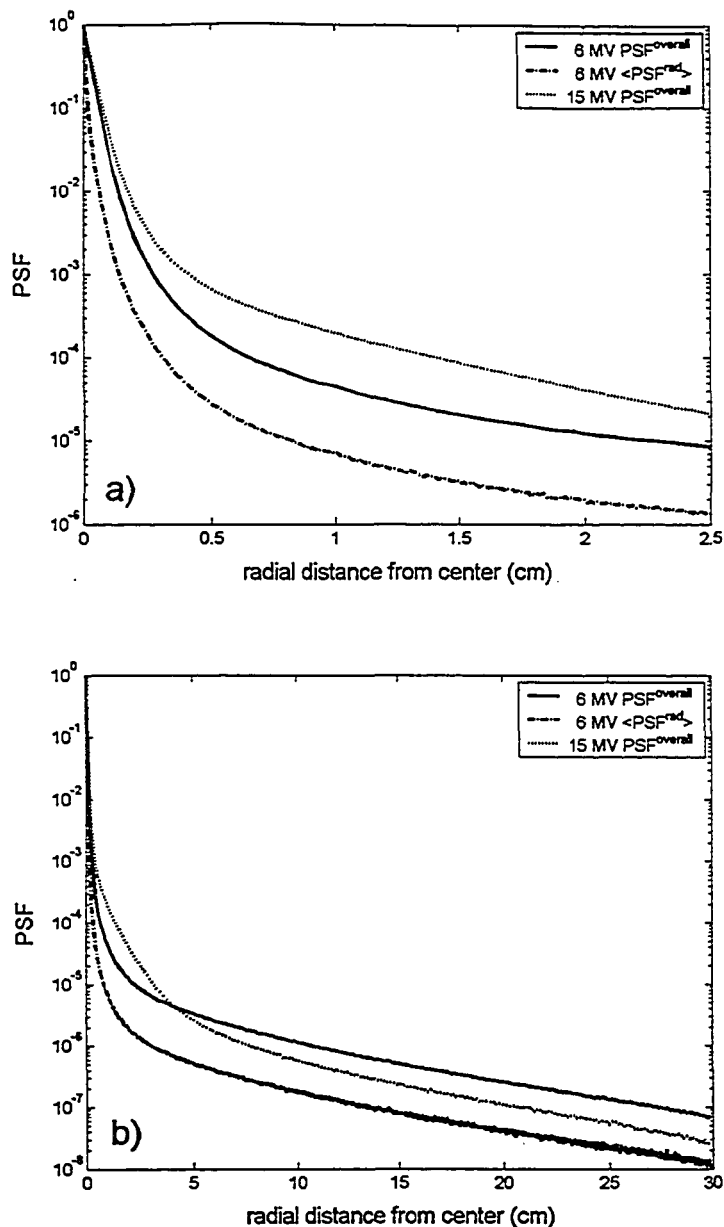
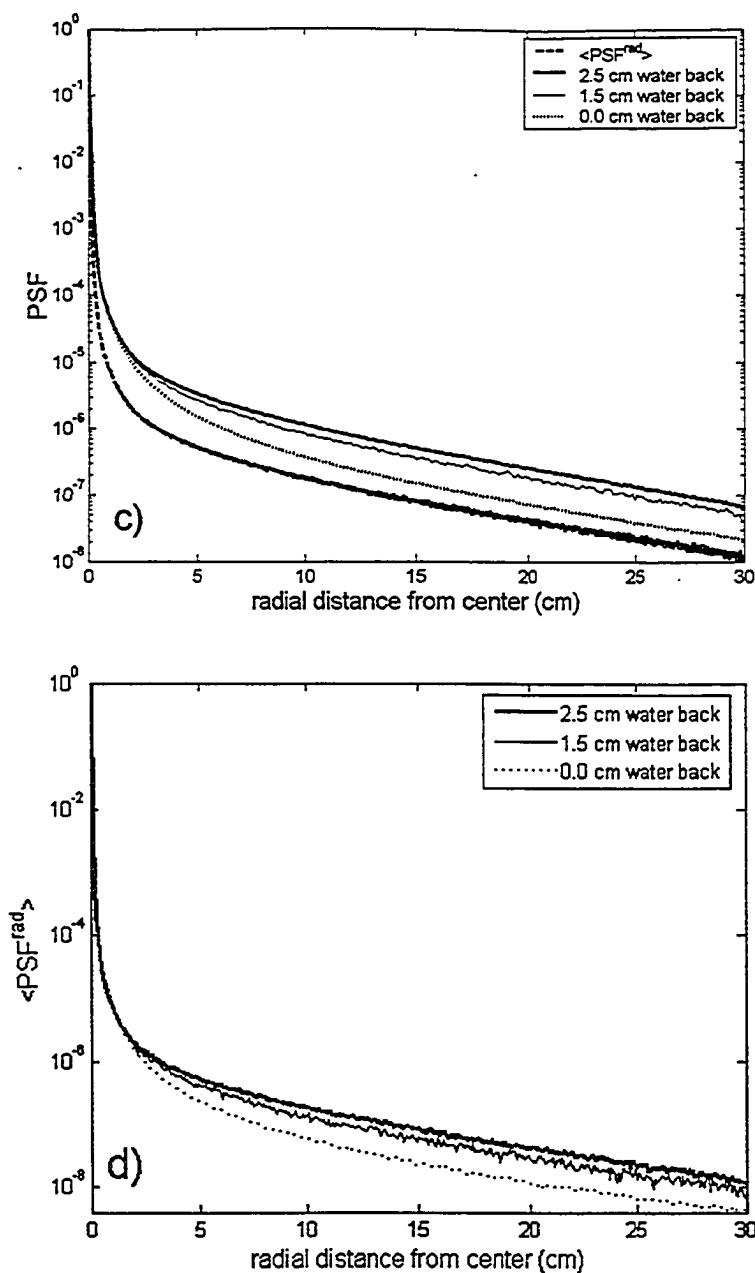


Figure 4.9 (a) and (b).  $\text{PSF}^{\text{overall}}(r)$  calculated for 6 and 15 MV beams, normalized to the central bin, shown in the near range (0-2.5 cm) (a) and far range (0-30 cm) (b).

$\langle \text{PSF}^{\text{rad}}(r) \rangle$  is also shown at 6 MV to illustrate the change in the kernel due to optical spreading. The 15 MV kernel is broader inside a 5 cm radius due to increased lateral electron transport at the higher energy. The tails display similar behavior, running nearly parallel beyond 10 cm.





**Figure 4.9 (c) and (d).** In (c) 6 MV results are shown for different thicknesses of solid water backscatter to gauge the relative contributions of backscatter and optical spreading.  $\langle \text{PSF}^{\text{rad}}(r) \rangle$  is also shown in (d) to directly illustrate the influence of the solid water backscatter thickness on the dose deposition kernel. For the 0.0 cm case, the rear panel of the detector was also removed.

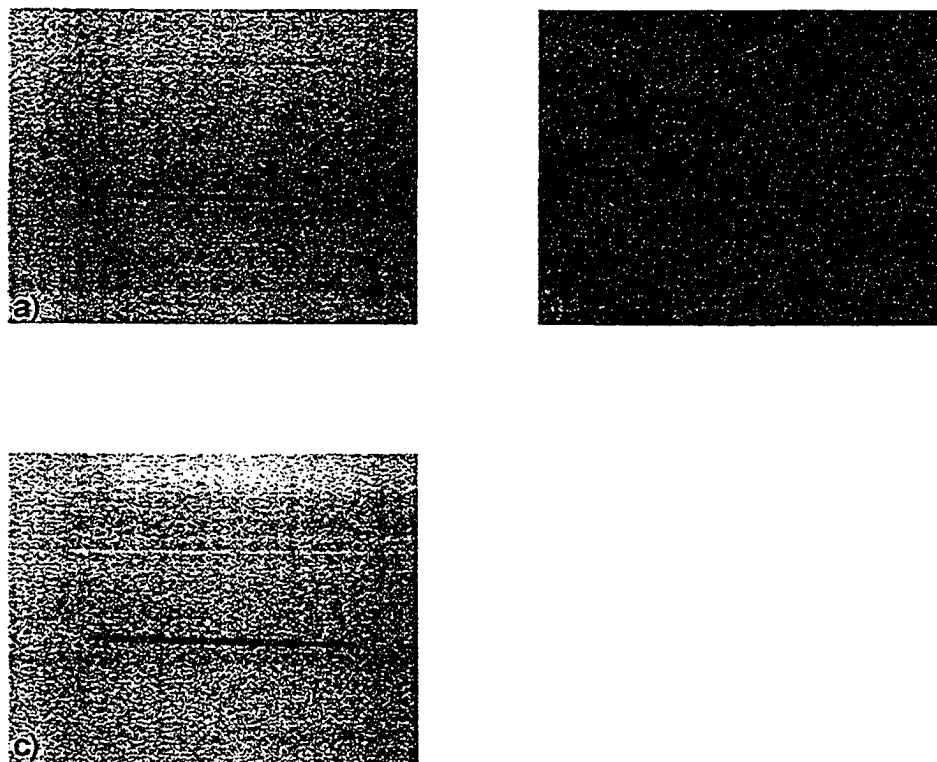


**Figure 4.10.** The images used for the LSF measurement at 6 MV. The original slit image (a), the offset image (b) as well as the final image (c) resulting from subtracting the pixel values of image (b) from image (a). The images have been magnified by a factor of 2.5 to give a better view of the slit region.

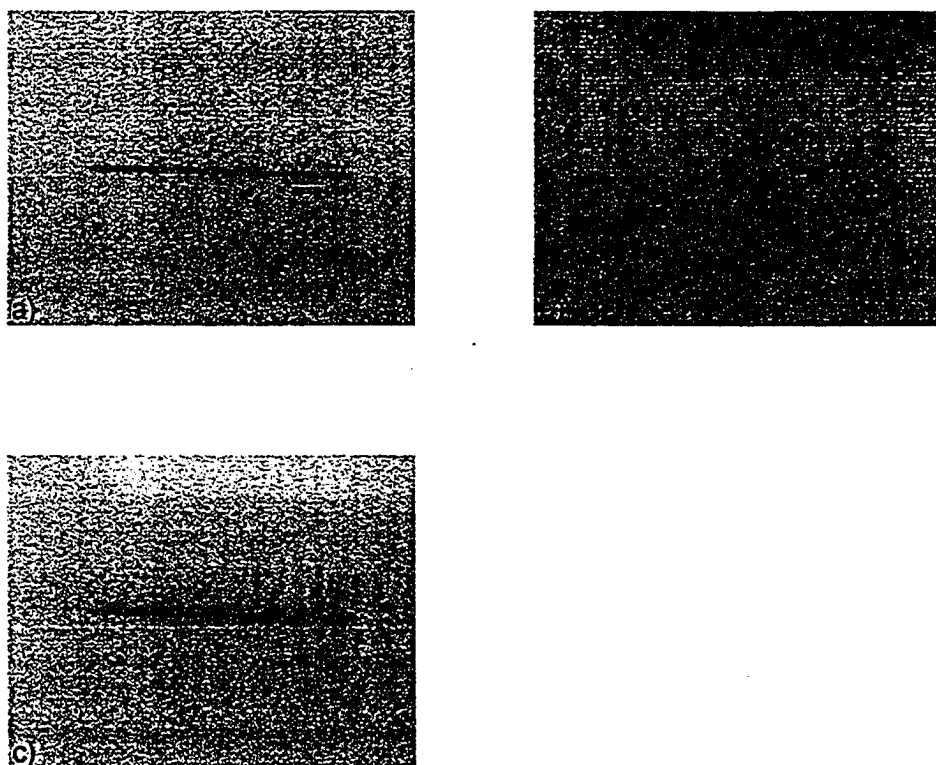


**Figure 4.11.** The images used for the LSF measurement at 15 MV. The original slit image (a), the offset image (b) as well as the final image (c) resulting from subtracting the pixel values of image (b) from image (a). The images have been magnified by a factor of 2.5 to give a better view of the slit region.

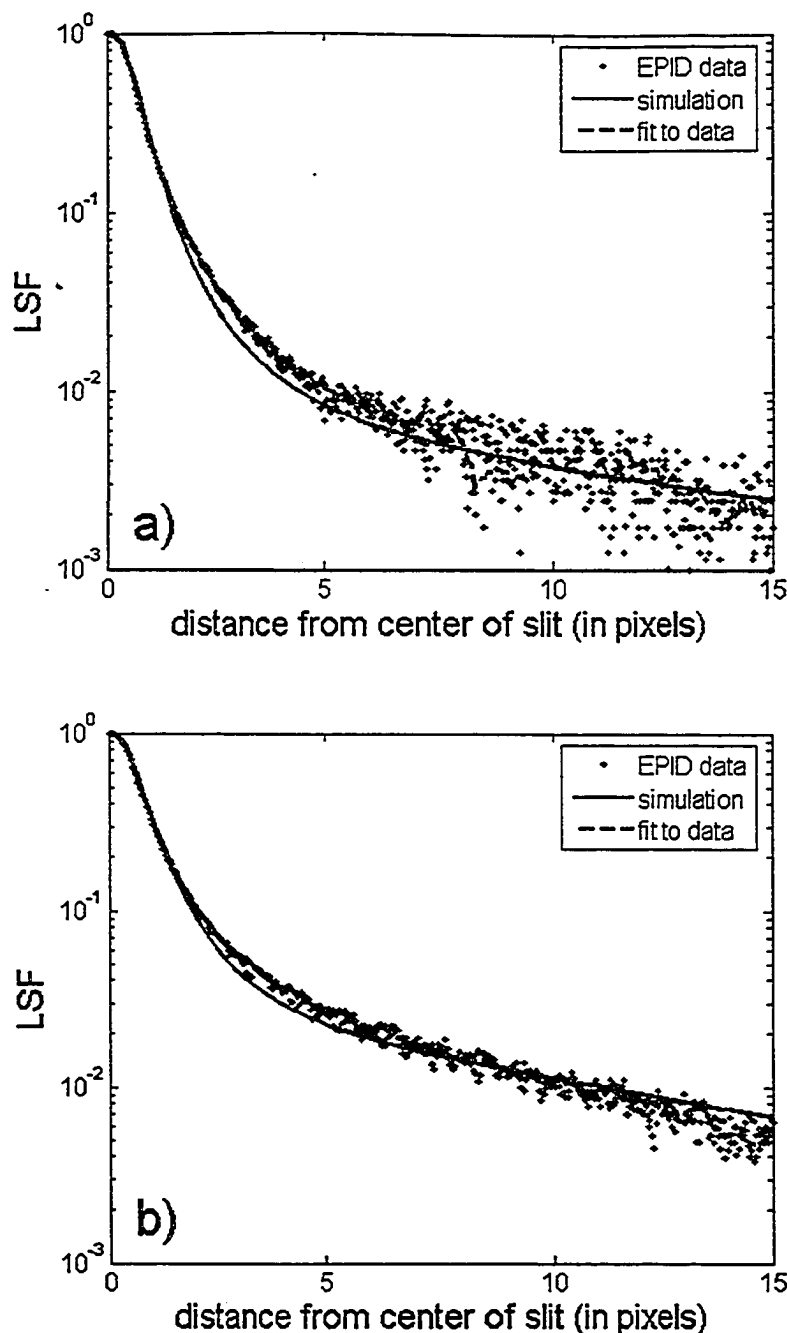


**Figure 4.12.** A comparison of our 6 MV (a) and 15 MV (b) LSF experimental data with the LSF calculated from our simulated PSF. A windowed average fit of the data points (spanning 20 points) is shown for each case as well. The data and simulation agree well as they fall through over two orders of magnitude across a distance of 15 pixels.

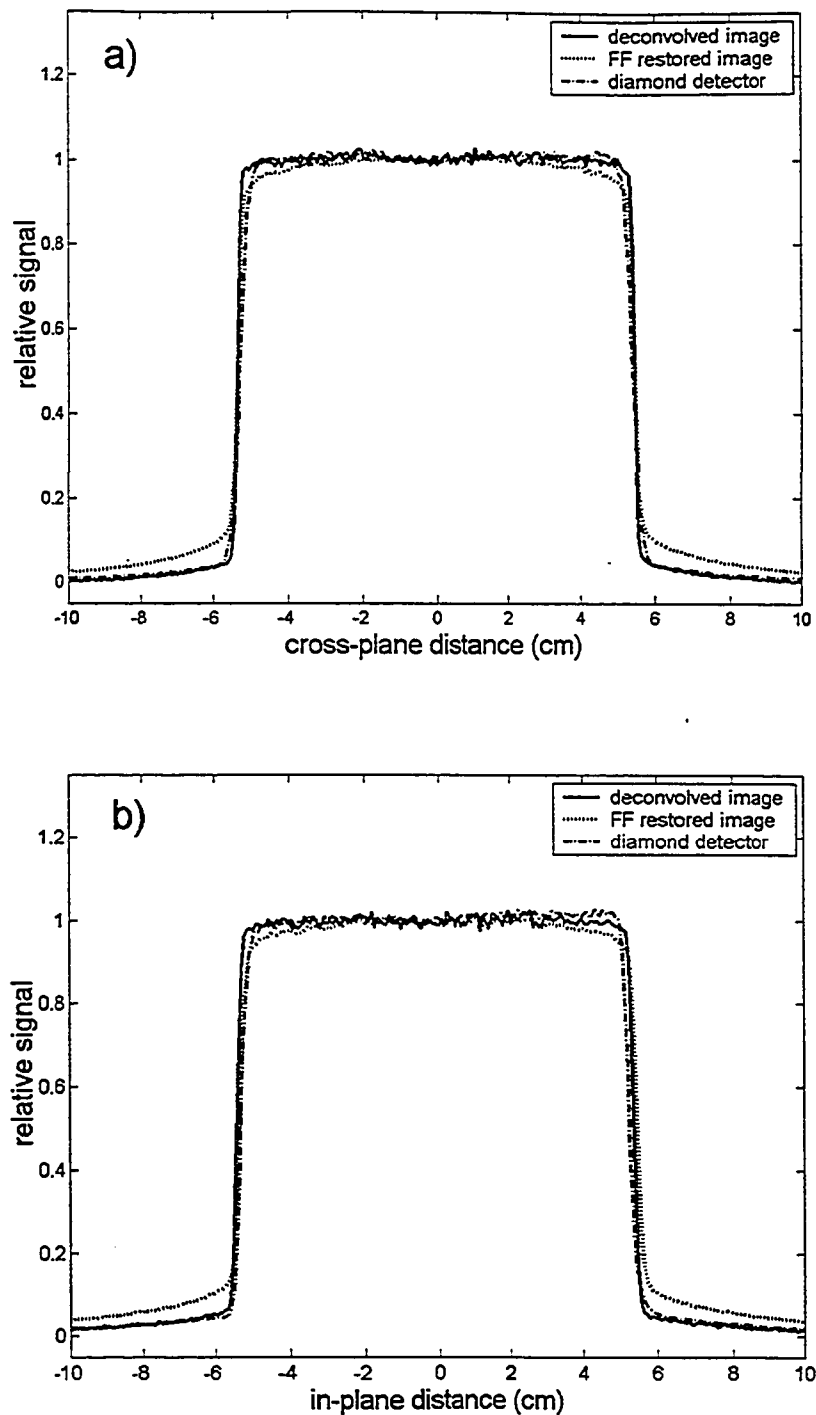


**Figure 4.13 (a) and (b).** Cross-plane (a) and in-plane (b) profiles for a 6 MV  $10 \times 10$   $\text{cm}^2$  field after deconvolution with  $\text{PSF}^{\text{overall}}$ , plotted along with flood field restored image and diamond detector profiles.

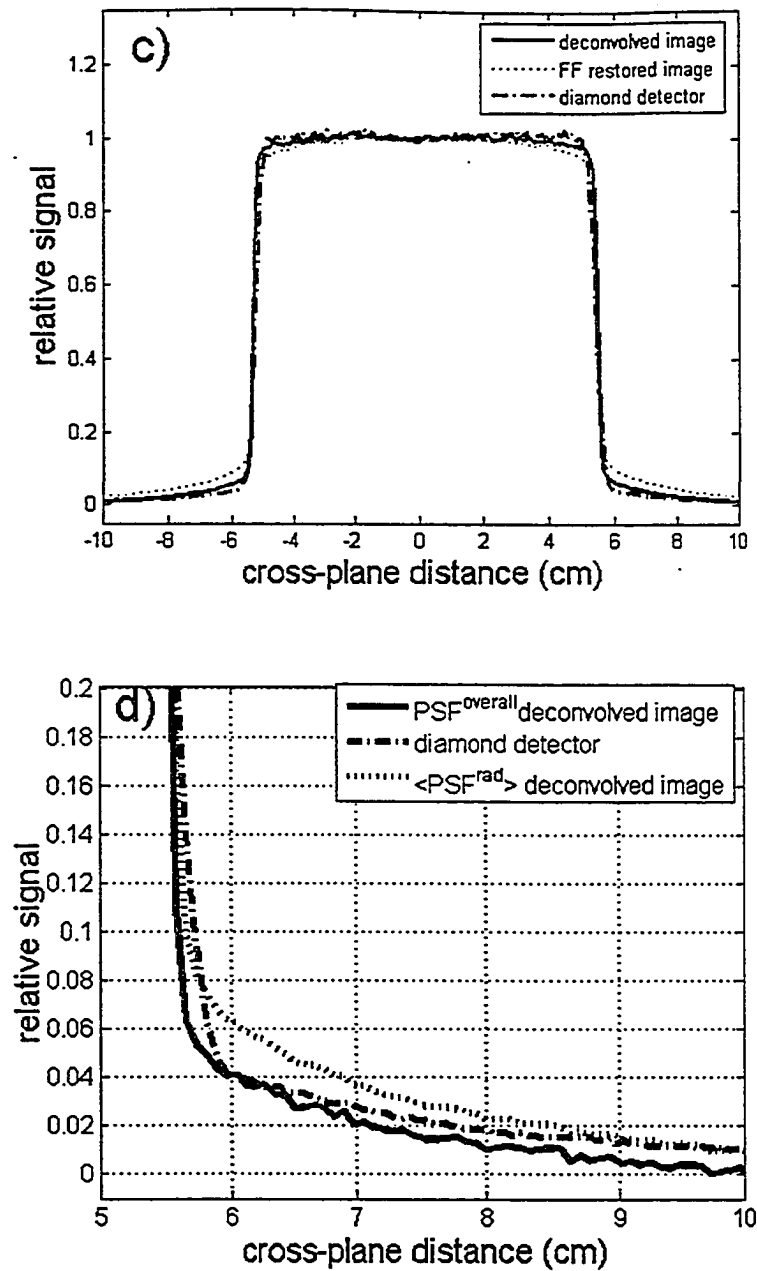


**Figure 4.13 (c) and (d).** In (c) the deconvolution had been performed with  $\langle \text{PSF}^{\text{rad}} \rangle$  in the cross-plane geometry. Differences due to the incorporation of the optical kernel are highlighted in (d), which focuses on the penumbra region where deconvolution has been performed both with (solid line) and without (dotted line) the optical kernel.

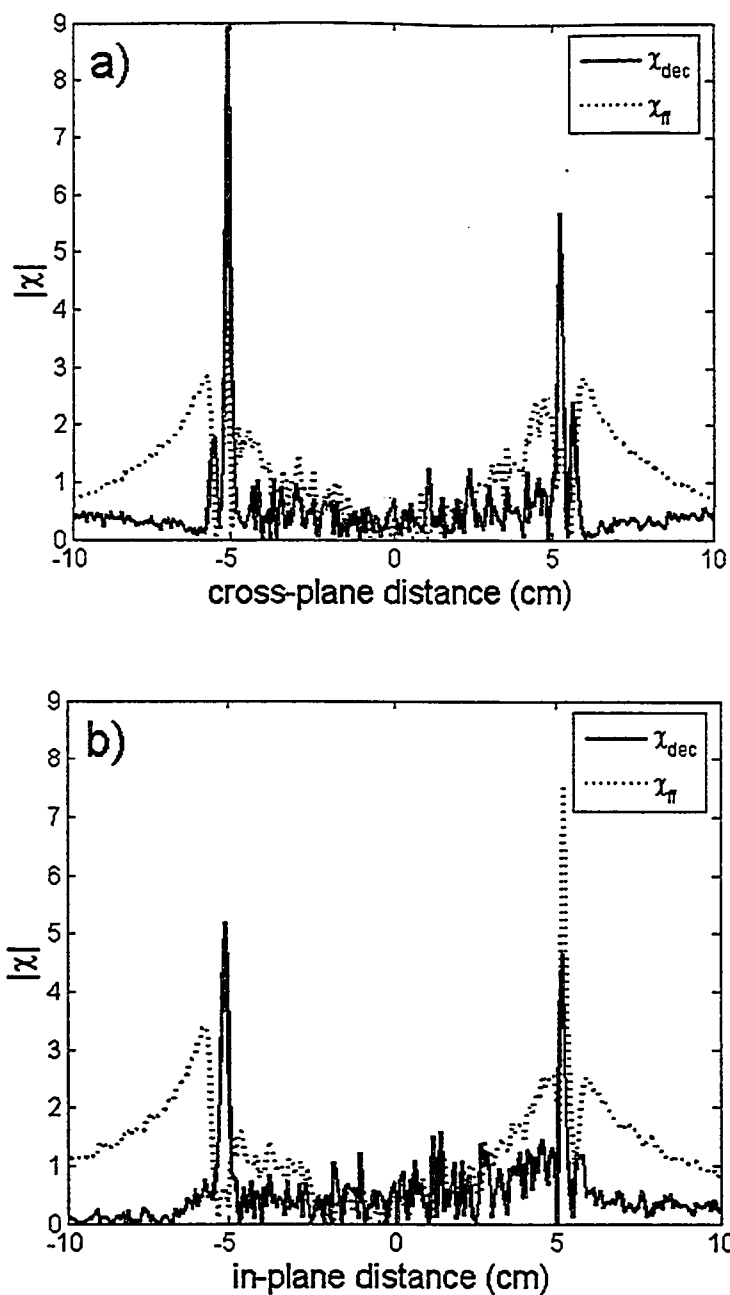


**Figure 4.14.** Magnitudes of the  $\chi$  scores corresponding to the image profiles in Fig. 4.12, cross-plane (a), and in-plane (b). Distinct peaks are seen in the high gradient regions both before and after deconvolution. The most substantial decrease is seen in the regions outside of the field.

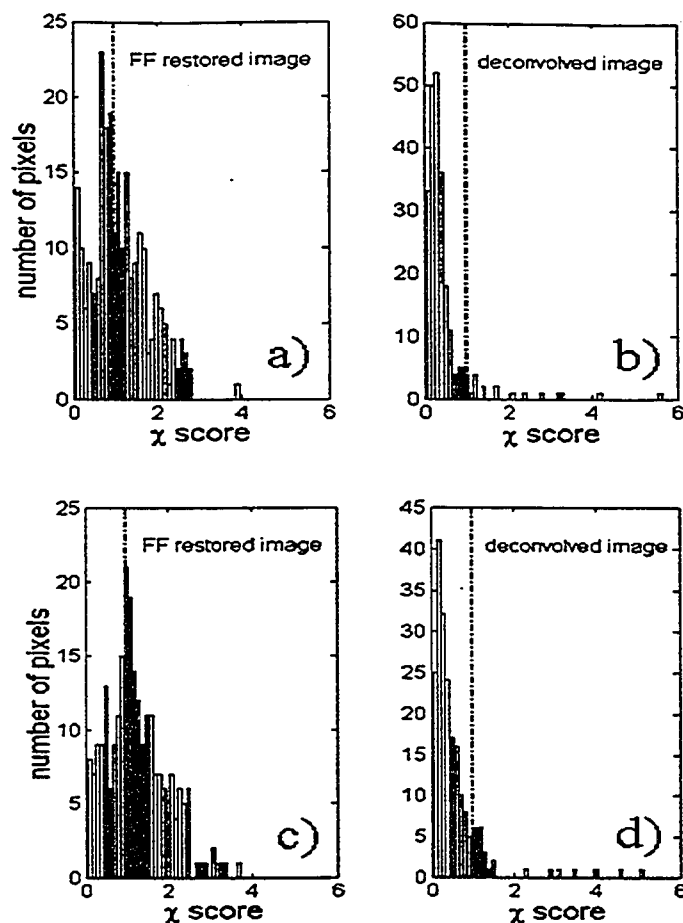


**Figure 4.15.** Histograms comparing the  $\chi$  scores of the flood field restored and deconvolved image profiles in Fig. 4.12, cross-plane (a and b), and in-plane (c and d). The dashed line on each histogram indicates a  $\chi$  score of 1.0 – below which the difference is considered acceptable. Deconvolution increased the percentage of acceptable points from 49.0 % (a) to 92.0 % (b) cross-plane, and from 43.4 % (c) to 89.9 % (d) in-plane. After deconvolution the scores are more heavily weighted towards the low end (most acceptable – least discrepancy). Due to the high gradient regions at the edges of the field and the volume averaging inherent in the diamond detector measurement, some high  $\chi$  scores cannot be avoided.



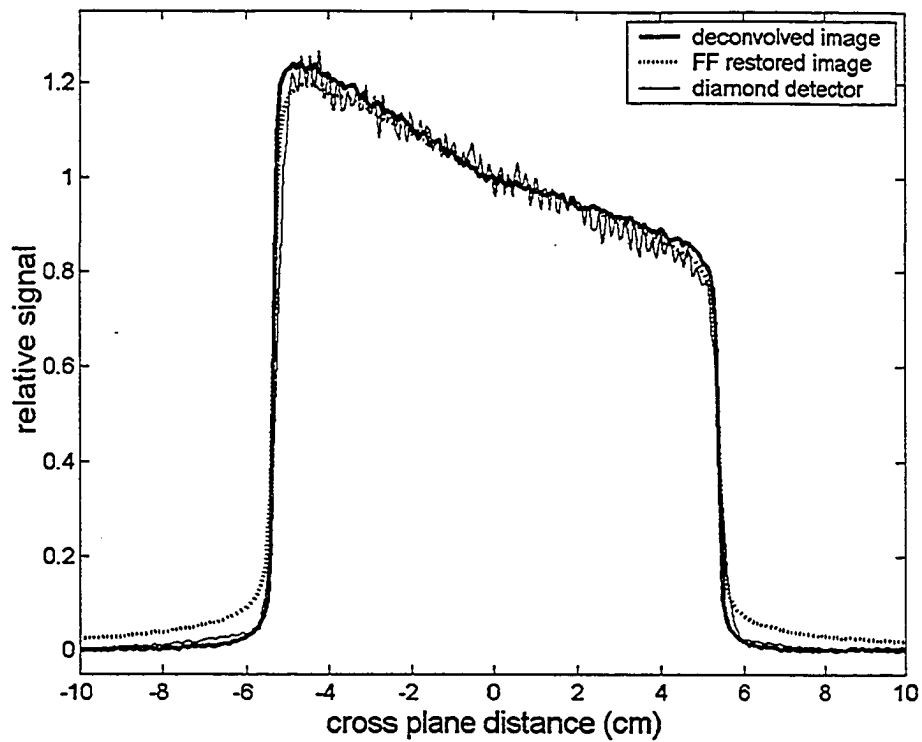


**Figure 4.16.** A  $10 \times 10 \text{ cm}^2$   $45^\circ$  physically wedged field at 6 MV. Deconvolution improves the profile measurement outside of the field. Improvements inside the field are not apparent.

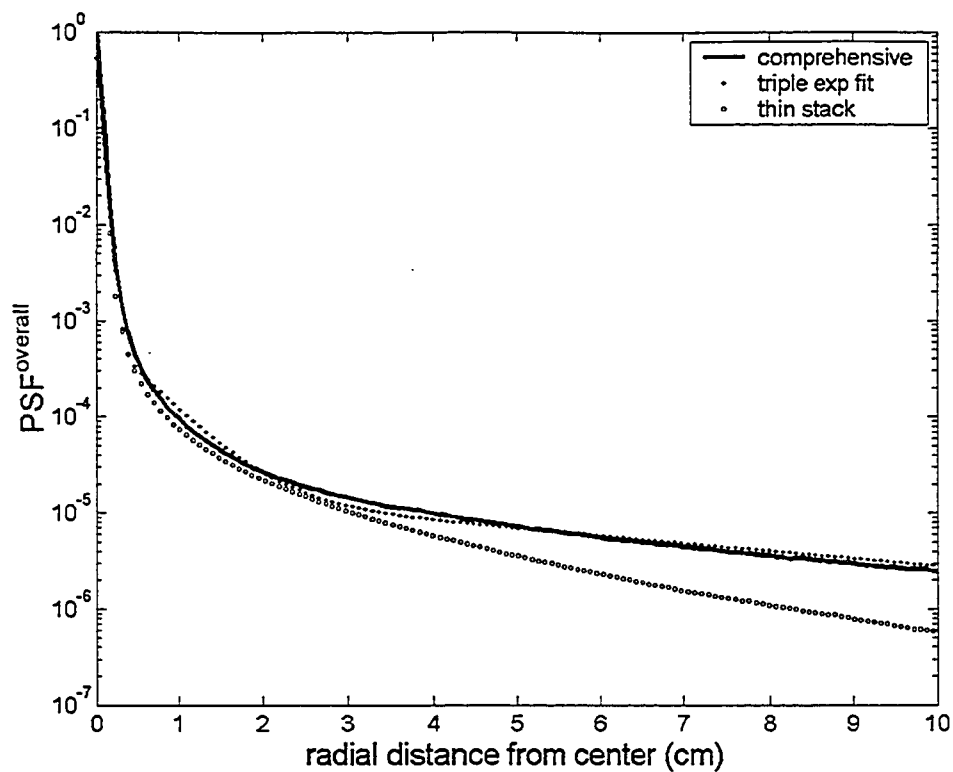


**Figure 4.17.** Comparison of different approaches to kernel calculation for the 6 MV beam. The solid line is the result derived from our comprehensive Monte Carlo model. The dotted line is a triple exponential function, obtained by fitting the comprehensive kernel, which could also be determined empirically. The open circles depict the result from our thin stack model, which differs in the tail region.

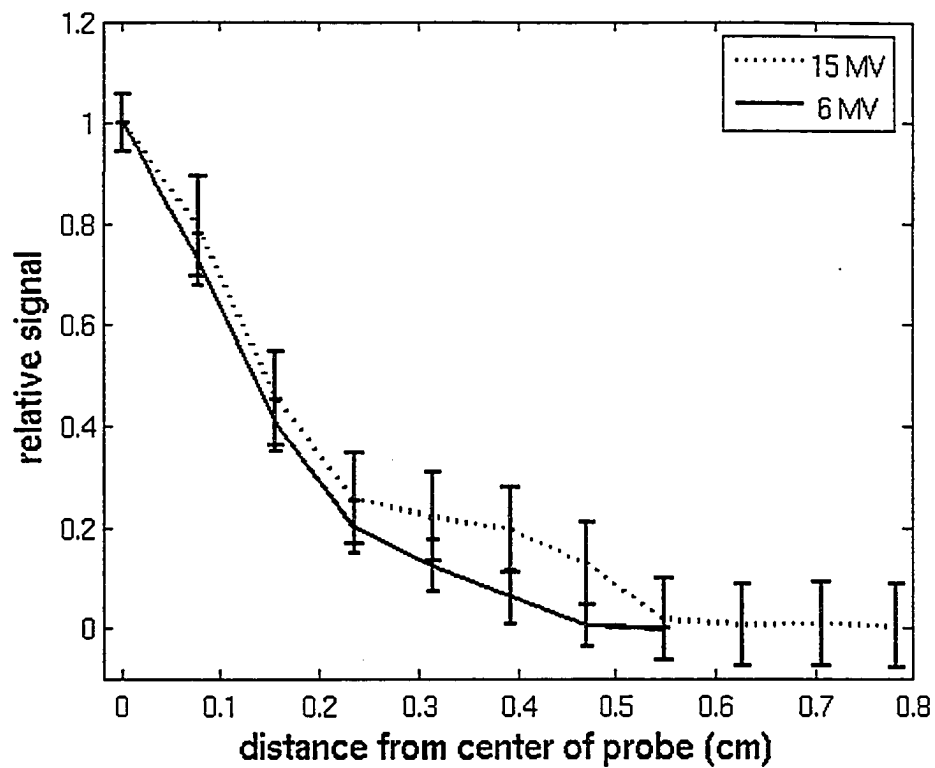


**Figure 4.18.** The blur kernels ( $LSF_{DD}(x)$ ) for the diamond detector. The FWHM is approximately 0.27 cm and 0.29 cm for the 6 and 15 MV beams, respectively. Error bars derive from the statistical uncertainties in the edge response function data.

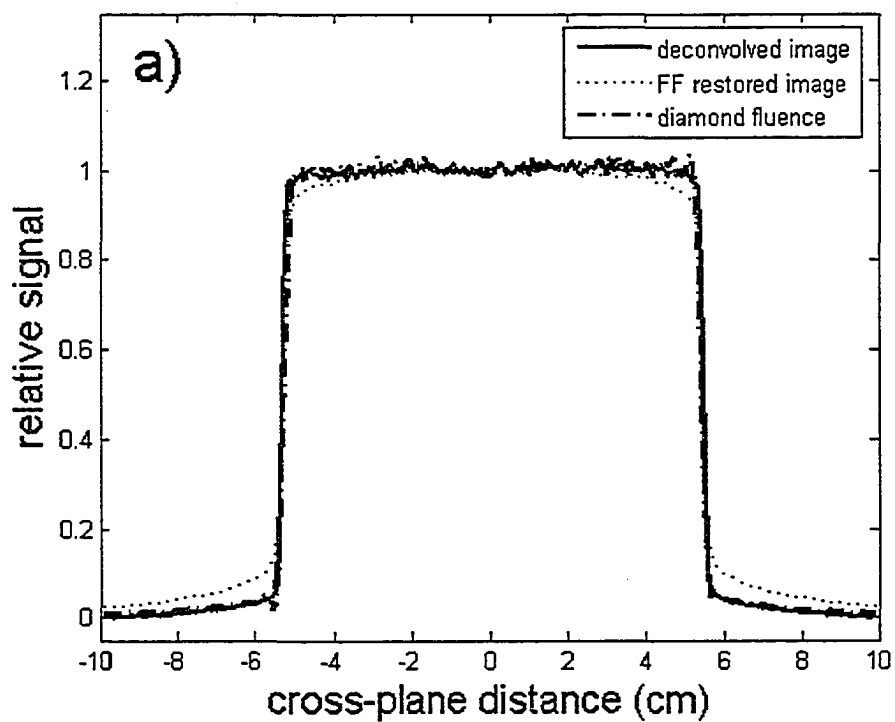


**Figure 4.19 (a)** . A cross-plane profile for a 6 MV  $10 \times 10 \text{ cm}^2$  field corresponding to that shown in Fig. 4.13 (a). Here the diamond detector profile has been deconvolved using  $\text{LSF}_{\text{DD}}(x)$ . The resulting diamond fluence is visibly sharper, but the fraction of  $\chi$  scores  $\leq 1$  is not increased significantly.

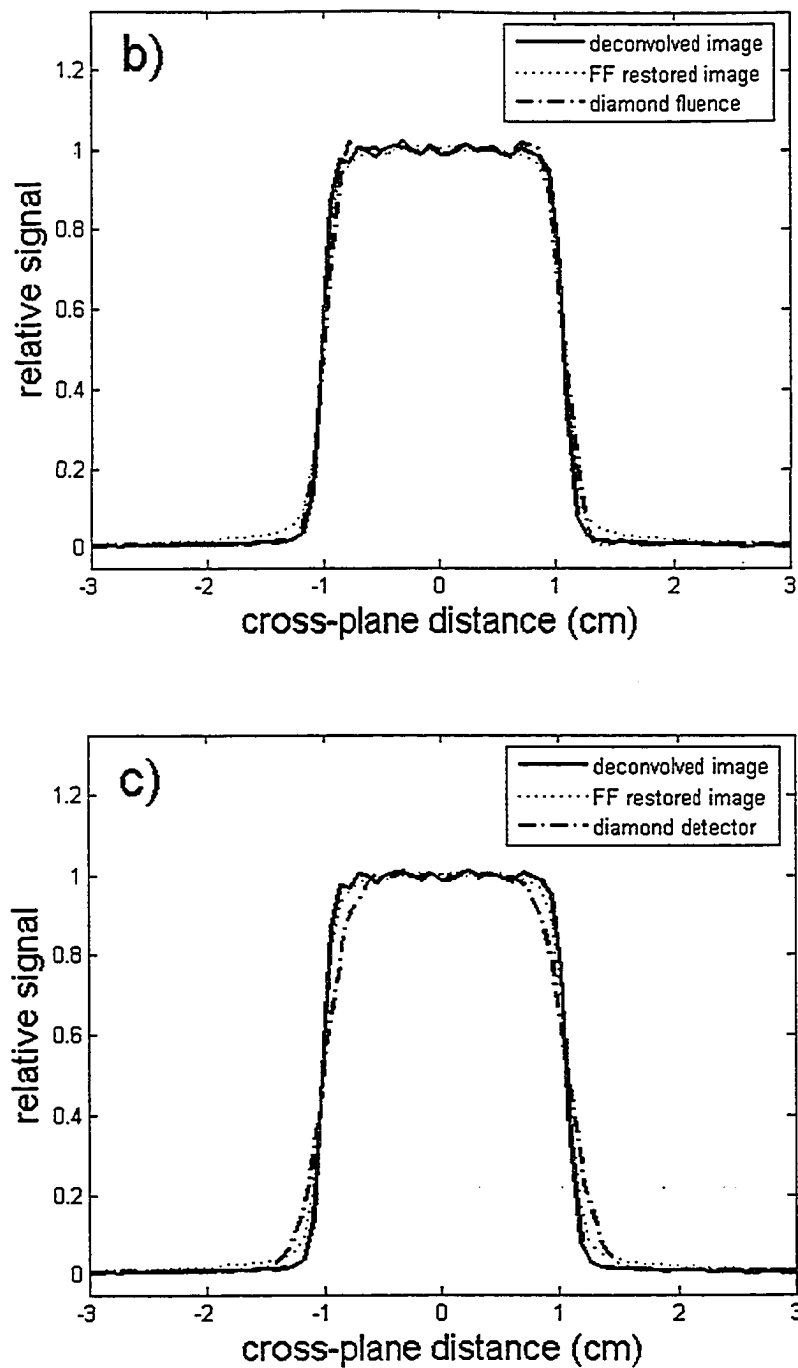


**Figure 4.19 (b) and (c)** . Cross-plane profiles for a 6 MV  $2 \times 2$  cm<sup>2</sup> field, with the diamond detector profile deconvolved (b) and for comparison, before deconvolution (c). The fraction of  $\chi$  scores  $\leq 1$  noticeably improves after deconvolution of the diamond profile for this smaller field.

## 4.5 REFERENCES

<sup>1</sup>Y. El-Mohri, L. E. Antonuk, J. Yorkston, K. W. Jee, M. Maolinbay, K. L. Lam, and J. H. Siewerdsen, "Relative dosimetry using active matrix flat-panel imager (AMFPI) technology," *Med Phys* **26** (8), 1530-41 (1999).

<sup>2</sup>B. M. McCurdy, K. Luchka, and S. Pistorius, "Dosimetric investigation and portal dose image prediction using an amorphous silicon electronic portal imaging device," *Med Phys* **28** (6), 911-24 (2001).

<sup>3</sup>G. V. Menon and R. S. Sloboda, "Compensator quality control with an amorphous silicon EPID," *Med Phys* **30** (7), 1816-24 (2003).

<sup>4</sup>B. Warkentin, S. Steciw, S. Rathee, and B. G. Fallone, "Dosimetric IMRT verification with a flat-panel EPID," *Med Phys* **30** (12), 3143-55 (2003).

<sup>5</sup>R. C. Gonzalez and R. E. Woods, *Digital Image Processing* (Addison-Wesley, Don Mills ON, 1992).

<sup>6</sup>M. Lachaine, E. Fourkal, and B. G. Fallone, "Investigation into the physical characteristics of active matrix flat panel imagers for radiotherapy," *Med Phys* **28** (8), 1689-95 (2001).

<sup>7</sup>L. Ko, J. O. Kim, and J. V. Siebers, "Investigation of the optimal backscatter for an aSi electronic portal imaging device," *Phys Med Biol* **49** (9), 1723-38 (2004).

<sup>8</sup>A. E. Schach von Wittenau, C. M. Logan, M. B. Aufderheide, 3rd, and D. M. Slone, "Blurring artifacts in megavoltage radiography with a flat-panel imaging system: comparison of Monte Carlo simulations with measurements," *Med Phys* **29** (11), 2559-70 (2002).

<sup>9</sup>G. Lubberts, "Random Noise Produced by X-Ray Fluorescent Screens," *J. Opt. Soc. Am.* **58**, 1475-1483 (1968).

<sup>10</sup>T. Radcliffe, G. Barnea, B. Wowk, R. Rajapakshe, and S. Shalev, "Monte Carlo optimization of metal/phosphor screens at megavoltage energies," *Med Phys* **20** (4), 1161-9 (1993).

<sup>11</sup>L. E. Antonuk, K. W. Jee, Y. El-Mohri, M. Maolinbay, S. Nassif, X. Rong, Q. Zhao, J. H. Siewerdsen, R. A. Street, and K. S. Shah, "Strategies to improve the signal and noise performance of active matrix, flat-panel imagers for diagnostic x-ray applications," *Med Phys* **27** (2), 289-306 (2000).

<sup>12</sup>I. Kawrakow, "Accurate condensed history Monte Carlo simulation of electron transport. II. Application to ion chamber response simulations," *Med Phys* **27** (3), 499-513 (2000).

- <sup>13</sup>I. Kawrakow and D.W.O. Rogers, The EGSnrc Code System: Monte Carlo Simulation of Electron and Photon Transport Report No. PIRS-701, 2002.
- <sup>14</sup>D. Sheikh-Bagheri and D. W. Rogers, "Monte Carlo calculation of nine megavoltage photon beam spectra using the BEAM code," *Med Phys* **29** (3), 391-402 (2002).
- <sup>15</sup>C. Moisan, F. Cayouet, and G. McDonald, *DETECT2000 A Program for Modeling Optical Properties of Scintillators* (Dept. of Electrical and Computer Engineering, Laval University, Quebec City, QC, 2000).
- <sup>16</sup>T. Yu, J. M. Sabol, J. A. Seibert, and J. M. Boone, "Scintillating fiber optic screens: a comparison of MTF, light conversion efficiency, and emission angle with Gd<sub>2</sub>O<sub>2</sub>S:Tb screens," *Med Phys* **24** (2), 279-85 (1997).
- <sup>17</sup>J. A. Rowlands and J. Yorkston, "Flat Panel Detectors for Digital Radiography," in *Handbook of Medical Imaging* (SPIE Press, Bellingham WA, 2000), pp. 223 - 328.
- <sup>18</sup>B. J. Heijmen, K. L. Pasma, M. Kroonwijk, V. G. Althof, J. C. de Boer, A. G. Visser, and H. Huizenga, "Portal dose measurement in radiotherapy using an electronic portal imaging device (EPID)," *Phys Med Biol* **40** (11), 1943-55 (1995).
- <sup>19</sup>G. Arfken, *Mathematical Methods for Physicists*, 3 ed. (Academic Press, Orlando FL, 1985).
- <sup>20</sup>S. Rathee, B. A. McClean, and C. Field, "An improved method for rebinning kernels from cylindrical to Cartesian coordinates," *Med Phys* **20** (5), 1343-51 (1993).
- <sup>21</sup>H. Fujita, K. Doi, and M. L. Giger, "Investigation of basic imaging properties in digital radiography. 6. MTFs of II-TV digital imaging systems," *Med Phys* **12** (6), 713-20 (1985).
- <sup>22</sup>B. H. Hasegawa, *The Physics of Medical X-Ray Imaging*, 2 ed. (Medical Physics Publishing, Madison WI, 1991).
- <sup>23</sup>J. Chang and C. C. Ling, "Using the frame averaging of aS500 EPID for IMRT verification," *J Appl Clin Med Phys* **4** (4), 287-99 (2003).
- <sup>24</sup>P. Munro and D. C. Bouius, "X-ray quantum limited portal imaging using amorphous silicon flat-panel arrays," *Med Phys* **25** (5), 689-702 (1998).
- <sup>25</sup>Varian Medical Systems, *Portal Vision aS500 Rel.6 Reference Manual* (Varian Medical Systems Inc., Palo Alto, CA, 2000).

- <sup>26</sup>E. Schule and C Pychlau, *Diamond Detector Type 60003 Instruction Manual* (PTW-Freiburg, Freiburg, 1998).
- <sup>27</sup>C. De Angelis, S. Onori, M. Pacilio, G. A. Cirrone, G. Cuttone, L. Raffaele, M. Bucciolini, and S. Mazzocchi, "An investigation of the operating characteristics of two PTW diamond detectors in photon and electron beams," *Med Phys* **29** (2), 248-54 (2002).
- <sup>28</sup>A. Bakai, M. Alber, and F. Nusslin, "A revision of the gamma-evaluation concept for the comparison of dose distributions," *Phys Med Biol* **48** (21), 3543-53 (2003).
- <sup>29</sup>D. A. Low, W. B. Harms, S. Mutic, and J. A. Purdy, "A technique for the quantitative evaluation of dose distributions," *Med Phys* **25** (5), 656-61 (1998).
- <sup>30</sup>J. T. Dobbins III, "Image Quality Metrics for Digital Systems," in *Handbook of Medical Imaging* (SPIE Press, Bellingham WA, 2000), pp. 161-222.
- <sup>31</sup>C. Kausch, B. Schreiber, F. Kreuder, R. Schmidt, and O. Dossel, "Monte Carlo simulations of the imaging performance of metal plate/phosphor screens used in radiotherapy," *Med Phys* **26** (10), 2113-24 (1999).
- <sup>32</sup>R. C. Taylor, V. M. Tello, C. B. Schroy, M. Vossler, and W. F. Hanson, "A generic off-axis energy correction for linac photon beam dosimetry," *Med Phys* **25** (5), 662-7 (1998).



## Chapter 5: Consequences of the spectral response of an a-Si EPID and implications for dosimetric calibration

### 5.1 INTRODUCTION

This chapter considers the aS500 EPID as a dosimeter with specific emphasis on its response across a 6 MV spectrum of photon energies and the consequences for dose calibration. In general, EPIDs have demonstrated considerable success in making dosimetric measurements<sup>1-6</sup> and offer an efficient alternative to other two-dimensional dose measurement technologies such as film. It has been established that a-Si EPIDs that employ high-Z scintillation screens, such as  $\text{Gd}_2\text{O}_2\text{S:Tb}$ , have an increased sensitivity to low energy ( $< 1$  MeV) photons.<sup>3,7-11</sup> This is in contrast with the fairly linear response vs. photon energy observed above 1 MeV where the Compton interaction dominates. Generally, EPID pixel values are calibrated against ion chamber readings in an open reference field where the energy spectrum is essentially that which exits the head of the linac.<sup>4,6</sup> However, the energy spectrum incident on the EPID can vary from that used for calibration. For example, beam hardening caused by a compensator or copious tissue can lead to a decreased fraction of low energy photons incident on the EPID. Such scenarios can alter the detector response from that observed under open field calibration conditions and introduce errors when converting from pixel values to dose.

In this chapter we investigate practical means to minimize the over-response of a commercial EPID to low energy photons. Our aim is to obtain a consistent EPID

dose-response under a variety of irradiation conditions where the incident 6 MV spectrum has hardened compared to an open field. Here we focus on the EPID response during compensator design verification measurements, but this work can also be applied in situations where a patient or phantom has hardened the beam. Naturally, any means of acquiring a consistent dose response needs to be balanced against possible degradation of the EPID's imaging characteristics.

Studies undertaken to date for other EPIDs suggest that this goal can be achieved for water-equivalent attenuators using an additional layer of copper (Cu) placed on top of the detector.<sup>3,10</sup> This layer would augment the internal Cu plate found in indirect detection EPIDs, which has been shown by Lachaine *et al.*<sup>9</sup> to have an optimal detective quantum efficiency for a thickness of 1 mm. Additional buildup material is useful in dosimetry applications to ensure that charged particle equilibrium is attained at the phosphor layer, and can also serve to further attenuate scattered radiation incident on the detector. Partridge *et al.*<sup>10</sup> suggest that Cu would be ideally suited for this purpose. Due to a sharp rise in mass attenuation coefficient below 500 keV, Cu preferentially attenuates the photons to which the EPID has an increased sensitivity. McDermott *et al.*<sup>3</sup> considered the response of an Elekta iViewGT a-Si EPID deployed downstream of a solid water phantom. They demonstrated that the EPID response varied with the air gap between the phantom and the EPID and found that the variation in EPID response was significantly reduced by placing a 2.5 mm layer of Cu on top of the EPID.

Previous work has been primarily concerned with reducing the variation in EPID response arising from scattered radiation, by modifying the detector setup after dose calibration.<sup>3,10</sup> The work presented in this chapter seeks to reduce the variation due to beam hardening in a 6 MV beam by modifying the detector prior to dose calibration. We approach the problem using Monte Carlo simulation to gain insight into the energy response characteristics of the aS500 EPID both in its conventional dosimetry configuration and with an external plate placed on top of the detector housing. Monte Carlo is also used to simulate the spectral changes to an open beam introduced by uniform attenuators of varying thickness. These results are then combined to predict trends in the overall EPID response for a range of Cu plate thicknesses. Finally, the predicted trends are investigated experimentally by measuring EPID calibration curves for a variety of operating conditions. Images of a standard quality control phantom are used to quantify the effects of the external plate on the imaging characteristics of the detector.

## 5.2 METHODS

### 5.2.1 Monte Carlo Investigations

EGSnrc version 3<sup>12-14</sup> (with user code DOSXYZnrc) was used to simulate the transport of ionizing radiation with default cut-off energies specified as PCUT = AP = 10 keV and ECUT = AE = 521 keV. Two types of simulations were performed. First, the spectral changes resulting from the passage of a 6 MV beam through a steel shot layer of variable thickness were determined to estimate the degree of beam hardening

that occurs during passage through a clinical compensator. Then the energy-specific dose deposited into the phosphor layer of the EPID was obtained.

#### *5.2.1.1 Energy Spectrum Variation*

The beam hardening simulation used an energy spectrum for a generic Varian 6 MV linac partitioned into 0.25 MeV wide bins and averaged over a small circular field ( $r = 2.5$  cm) at the central axis.<sup>15</sup>  $2 \times 10^6$  photons were normally incident at a point on the surface of a compensator model (beam divergence was ignored). The model consisted of a layer of steel shot of variable thickness sandwiched between 0.6 cm thick Lucite panels. The steel shot was assumed to have a composition of 0.99 Fe and 0.01 C and a density of  $4.69 \text{ g/cm}^3$  (low density is due to the packing ratio), consistent with measurements performed on the physical compensators.<sup>4</sup> The layers ranged in thickness from 0.5 to 4.5 cm in increments of 0.5 cm. The Styrofoam housing used to contain the shot was not modeled. Primary and scattered photons emerging from the bottom Lucite panel were collected and scored in 0.25 MeV wide bins as they crossed a  $10 \times 10 \text{ cm}^2$  plane in air located 35 or 70 cm below the compensator (corresponding to the distance between the compensator and detector for a source-to-detector distance (SDD) of 105 or 140 cm, respectively). For the purpose of assessing the effect of adding Cu on the photon spectrum, the simulations were repeated with a 1.0 cm Cu plate located 15 cm above the detection plane.

### 5.2.1.2 EPID Energy Response

The detector simulation modeled the central axis dose to the phosphor layer of the EPID for a series of monoenergetic beams of size  $10 \times 10 \text{ cm}^2$  projected in parallel geometry onto a comprehensive model of the EPID.<sup>16</sup> Dose was scored in a  $1 \times 1 \text{ cm}^2$  voxel on the central axis through the full thickness of phosphor ( $340 \text{ }\mu\text{m}$ ). Beam energies were defined by the centers of consecutive  $0.25 \text{ MeV}$  wide bins (to correspond to the scoring bins defined for the preceding simulation) spanning the range  $0 - 2 \text{ MeV}$ . Beyond  $2 \text{ MeV}$  we took advantage of the slower change in deposited dose with increasing energy and used larger steps ( $0.5 \text{ MeV}$  and  $1.0 \text{ MeV}$ ) up to  $6 \text{ MeV}$ . Doses at intermediate energies were obtained by linear interpolation. The simulations were run with enough histories to reduce the statistical uncertainty in each result to  $\leq 2 \%$  ( $\sim 2 \times 10^7$  histories for each energy interval). In order to speed up simulation, electron range rejection was used. This technique checks the electron range against the distance to the nearest boundary and terminates the history if the electron will not escape and is below a specified energy, which we set at  $0.611 \text{ MeV}$ . Differences between simulations with range rejection turned on versus off for a model of the EPID in its conventional configuration irradiated by a monoenergetic  $2 \text{ MeV}$  photon beam were  $< 1 \%$ ; thus we assume that the uncertainties introduced by using this technique are smaller than the statistical uncertainties.

The EPID model was developed based on data for the Varian aS500 provided by the manufacturer (Sec. 2.3). The principle detector components include a  $0.896 \text{ g/cm}^2$  Cu plate and Lanex Fast-B screen ( $0.134 \text{ g/cm}^2 \text{ Gd}_2\text{O}_2\text{S:Tb}$ ).<sup>17</sup> Our model also

incorporated structural components such as the screen housing and protective cover. An additional slab of 2.5 cm of solid water was modeled directly beneath the EPID to simulate the contribution from photons scattered from supporting hardware. In dosimetric operation at our center, 0.5 cm of solid water is placed directly on top of the EPID cassette to provide additional buildup at 6 MV. We refer to this as the “conventional” configuration. Other configurations simulated incorporate an additional, external plate. Cu was investigated as the primary candidate material for this plate, but aluminum and lead were also considered. Both the position and thickness of the external plate were varied. We considered positions directly on top of the EPID (in place of the solid water) or elevated from its surface. When elevated, the plate was supported by a layer of low density ( $0.05 \text{ g/cm}^3$ ) Styrofoam 0 – 30 cm thick. The external plate thickness varied from 0.25 – 1.25 cm.

### 5.2.1.3 Simulated Calibration Curve

To generate a simulated calibration curve relating the calculated EPID response to an ideal ion chamber (IIC) measurement, we first combined the above results into an overall EPID response,

$$R_{EPID} = \sum_i r(E_i) \cdot \varphi(E_i), \quad (5.1)$$

for each particular measurement scenario. Here  $r(E_i)$  is the response to a monochromatic photon beam of energy  $E_i$  modeled as the dose to the phosphor, and  $\varphi(E_i)$  is the fluence of incident photons of energy  $E_i$  impinging on the EPID, modeled as the spectral weight scored in each energy bin. EPID dose calibration, as we have indicated, is performed relative to in-air dose measurements made by an ion chamber.

Thus our simulations need to include a model of ion chamber response. To model an IIC response, we assumed a reading directly proportional to the dose deposited in the ion chamber cavity, and chamber walls and buildup material sufficient to obtain charged particle equilibrium, so that

$$R_{IC} = D_{\text{air}}^{\text{cav}} = K_C^{\text{cav}} = \sum_i \varphi(E_i) \cdot E_i \cdot \left( \frac{\mu_{\text{EN}}}{\rho} \right)_{E_i}^{\text{air}}. \quad (5.2)$$

Note that  $D_{\text{air}}^{\text{cav}}$  is the dose to air in the ion chamber cavity in the measurement scenario,  $K_C^{\text{cav}}$  is the corresponding collision kerma, and  $\left( \frac{\mu_{\text{EN}}}{\rho} \right)_{E_i}^{\text{air}}$  is the mass energy-absorption coefficient for air at energy  $E_i$ . The EPID response  $R_{\text{EPID}}$  can then be plotted against  $R_{IC}$  to yield a simulated calibration curve.

### 5.2.2 Experimental Measurements

Experimental measurements aimed to address the following problems. First, we wanted to reproduce and quantify the calibration curve discrepancy between open and steel shot attenuated beams reported earlier by Menon and Sloboda.<sup>4</sup> Then, guided by the Monte Carlo investigations outlined above, we wanted to determine the appropriate thickness of Cu to place above the EPID to minimize this discrepancy. Due to scatter from the external plate, it was also of interest to determine the best location for it relative to the imaging cassette surface. Finally, we aimed to quantify the EPID's contrast-to-noise ratio (CNR) and spatial resolution for the different scenarios as a means of assessing the consequences of introducing the external plate on EPID imaging performance.

### *5.2.2.1 EPID and Ion Chamber Measurements*

EPID measurements were made with the aS500 operating in IMRT mode. This mode continuously acquires frames over the entire time the beam is delivered and yields an averaged image. In all cases a Varian 2100X linac delivered 60 monitor units (MU) at a rate of 300 MU/min, resulting in approximately 104 frame averages in the images analyzed. All measurements were made at 6 MV, with the exception of one set made at 15 MV to determine whether or not the dose-response difference is predominantly a low energy phenomenon. Ion chamber measurements were made using a Capintec PR-06C Farmer Replacement Chamber coupled to a Capintec Model 192 Exposure/Exposure Rate Meter (Capintec, Inc. Ramsey, NJ). The ion chamber was fitted with a 1.5 cm (radial thickness) acrylic buildup cap. All measurements were performed using a field size of  $10 \times 10 \text{ cm}^2$  defined at the phosphor layer inside the EPID, or in a horizontal plane containing the center of the ion chamber. For open field measurements, the SDD was varied from 105 to 160 cm, which served to vary the dose rate at the detector. This resulted in a near-constant energy spectrum incident on the central area of the detector (apart from minor changes arising primarily from the change in head scatter with distance). For attenuated beam measurements, the detectors were fixed at an SDD of 105 or 140 cm, and the dose rate at the detector was varied by placing different thicknesses of compensator material in the beam. This approach demonstrably hardened the incident photon spectrum. Unless otherwise noted, results presented are for an SDD of 105 cm, as it



was found that ion chamber readings for the attenuated beams at SDD = 140 cm fell outside the range of open field readings.

Reported ion chamber measurements are normalized to the measurement recorded for an open  $10 \times 10 \text{ cm}^2$  field at 105 cm SDD. This allows for comparison of measurements made on subsequent days while minimizing effects due to variation in linac output or differences in measurement conditions such as temperature or pressure. Reported EPID responses are the result of averaging  $13 \times 13$  pixels ( $\sim 1 \times 1 \text{ cm}^2$ ) centered on the central axis. Similar to the ion chamber, the reported results are normalized to the average pixel value recorded for an open  $10 \times 10 \text{ cm}^2$  field defined at 105 cm SDD.

#### *5.2.2.2 Beam and Detector Configurations*

As in the simulations, the conventional setup had a 0.5 cm solid water slab placed atop the EPID. The EPID was then image-calibrated (both flood and dark field images taken) with the solid water slab in place. A number of  $15 \times 15 \text{ cm}^2$  Cu plates, each  $0.315 \pm 0.002 \text{ cm}$  thick, were stacked to produce varying thicknesses of external plate. Subsequent image calibrations with the Cu plates in place were not performed. Thus all raw image data (see Eqn. 2.1) were divided by a flood field image taken with the solid water slab in place. In this way we could track the relative effects of increasing Cu thickness by direct examination of the pixel values. Alternatively, calibrating the EPID image with a flood field image taken with a Cu plate in place is unlikely to affect the results because all points on figures 5.8 and 5.9,

for example, would simply be divided by a different factor, which would cancel out in the normalization process. Clinically speaking, image calibration should be done consistently in a single configuration that is adopted for dosimetry, as image calibration will affect absolute dose calibration.

The Cu was placed in two configurations: the first directly on top of the detector (contact configuration), and the second on top of a 15.3 cm Styrofoam slab placed on the detector (elevated configuration). The elevated configuration was used to examine the effect of scatter generated in the buildup plate on the EPID response. The distance of 15 cm was arrived at based on the results of the Monte Carlo simulations. The solid water slab was not present in configurations where the external Cu plate was used.

Compensators were used to attenuate the beams. These were constructed via the standard technique used in our center described by Menon and Sloboda.<sup>4</sup> Styrofoam slabs ( $\sim 25.5 \times 25.5 \times 5.1 \text{ cm}^3$ ) were cut and filled with steel shot to various uniform depths from 0.5 to 4.5 cm in 0.5 cm increments, covering the relevant range of steel shot thicknesses seen in the clinic. The slabs were sandwiched between Lucite plates 0.6 cm thick. As mentioned in Sec. 5.2.1.1, when the packing ratio of the steel shot is accounted for, the material has a density of  $4.69 \text{ g/cm}^3$ .

We also considered a scenario designed to mimic those in which an EPID would be used for transmission dosimetry with a patient in the beam. Slabs of solid

water ( $25 \times 25 \times 1 \text{ cm}^3$ ) were centered in the field and stacked on the treatment couch to a maximum thickness of 20 cm. The couch was placed at 100 cm from the source and the EPID deployed at 140 cm SDD. Images were taken with the EPID in the conventional configuration and with  $0.630 \pm 0.004 \text{ cm}$  of Cu in the elevated configuration.

Finally, the spectral effect at 15 MV was quantified using two measurement geometries wherein a given open field SDD and attenuator thickness yielded identical ion chamber readings. Specifically, measurements were made at 142 cm SDD for an open field, and at 105 cm SDD for a beam attenuated by 3.5 cm of steel shot. An open field measurement at 105 cm SDD was again used for normalization. At this beam energy it was found that the ion chamber gave identical readings (within 0.2 %) for the two measurements.

### *5.2.2.3 Imaging Performance*

Images of a QC-3V phantom and the PIPspro 3.2.03 software package (Standard Imaging, Inc., Middleton WI) were used to assess the effects of the different beam/detector configurations on both the CNR and spatial resolution as measured by  $f_{50}$  for a square wave modulation transfer function (SWMTF). On each image, regions of interest (ROIs) are defined that correspond to eleven different regions in the phantom. Five of these consist of bar patterns with spatial frequencies ranging between 0.76 and 0.10 lp/mm, and are used to calculate a SWMTF. The other six regions consist of uniform materials of varying depth. The CNR is taken as

the difference between average pixel values for the brightest and darkest regions divided by the standard deviation of the image noise in these regions. For a detailed description of the methodology employed refer to Rajapakshe *et al.*<sup>18</sup> and the PIPSPRO User's Guide.<sup>19</sup>

The images were taken in IMRT mode through delivery of 60 MU at a rate of 300 MU/min, the same parameters used for the other measurements. The QC-3V phantom was placed at isocenter while the EPID was deployed at SDD = 120 cm, a distance chosen to allow room for both external plate configurations and to keep the projected field within the area ( $15 \times 15 \text{ cm}^2$ ) covered by the Cu plates. Images were taken for the conventional configuration as well as with the Cu plate in the contact and elevated positions.

### 5.2.3 Calibration Curve Differences

For both the Monte Carlo and experimental results it was necessary to evaluate the difference between the open and attenuated beam calibration curves. The open field case yields a linear relation<sup>4,6</sup> between the relative ion-chamber reading ( $\mathfrak{R}_{IC}$ ) and relative EPID pixel value ( $\mathfrak{R}_{EPID}$ , which is assumed to be equivalent to phosphor dose for the Monte Carlo results); thus it can be fit with a straight line.

$$\mathfrak{R}_{EPID}^{\text{open}} = y_1 + a_1 \cdot \mathfrak{R}_{IC} \quad (5.3)$$

Other work<sup>4</sup> has suggested that the attenuated field curve can be well fit using a quadratic form.

$$\mathcal{R}_{\text{EPID}}^{\text{atten}} = y_2 + a_2 \cdot \mathcal{R}_{\text{IC}} + b_2 \cdot \mathcal{R}_{\text{IC}}^2 \quad (5.4)$$

For the Monte Carlo investigation, we assumed an ideal response ( $y_1 = 0$ ,  $a_1 = 1$ ) for the open field. For all other cases the coefficients were determined using the regression analysis tool in Sigmaplot 8.0 (SPSS Inc., Chicago, IL) by fitting all data points on each curve. The maximum difference between the open and attenuated curves is then estimated as

$$\left( \mathcal{R}_{\text{EPID}}^{\text{open}} - \mathcal{R}_{\text{EPID}}^{\text{atten}} \right)_{\text{max}} = y_1 - y_2 + \frac{(a_1 - a_2)^2}{4b_2}. \quad (5.5)$$

Differences quoted are expressed as a percentage of  $\mathcal{R}_{\text{EPID}}^{\text{open}}$  at the point of maximum difference,  $\mathcal{R}_{\text{IC}}|_{\text{max d}}$ , or

$$\text{difference} = \frac{\left( \mathcal{R}_{\text{EPID}}^{\text{open}} - \mathcal{R}_{\text{EPID}}^{\text{atten}} \right)_{\text{max}}}{\mathcal{R}_{\text{EPID}}^{\text{open}} \left( \mathcal{R}_{\text{IC}}|_{\text{max d}} \right)} \cdot 100\%. \quad (5.6)$$

## 5.3 RESULTS

### 5.3.1 Monte Carlo Investigations

#### 5.3.1.1 Energy Spectrum Variation

Figure 5.1(a) shows the relative spectra computed in the plane at SDD = 105 cm in relation to the 6 MV spectrum incident on the compensator model. We can make two observations. First, there is a substantial reduction in the number of transmitted photons. Second, we note that the mean energy of the spectrum increases from 1.67 MeV for the incident beam to 2.08 MeV for the beam filtered by 4.5 cm of steel shot, a change of 24%. Hence there is significant beam hardening through the

range of attenuator thicknesses examined. In Fig. 5.1(b) we see an example of the spectrum change with a 1.0 cm Cu plate placed 15 cm above the detection plane. The relative change in the distribution is significantly decreased for the low energy bins.

### 5.3.1.2 EPID Energy Response

In figure 5.2 we present the results of the dose response simulations for the EPID in the conventional setup as a function of energy. The uncertainties are  $\leq 2\%$  of the scored dose, as represented by the error bars. Error bars are omitted in subsequent figures, but have equal or smaller magnitudes. Also plotted is an

estimated IIC relative dose response,  $E_i \cdot \left( \frac{\mu_{EN}}{\rho} \right)_{E_i}^{\text{air}}$ , taken from equation 5.2. For

comparison, we have normalized each curve to the dose scored in the energy bin centered at 1.125 MeV (the same normalization applies to Figs. 5.4 and 5.5). For photon energies  $> 1$  MeV, the IIC response and EPID response are reasonably consistent with each other. In this region the mean difference between the curves is 9%. Below 1 MeV however, the EPID response deviates substantially from the IIC response. At the lowest energy, the difference is greater than an order of magnitude. The increased sensitivity of the EPID in this region is likely due to the sharp increase in the mass energy-absorption coefficient of  $\text{Gd}_2\text{O}_2\text{S}$ ,<sup>20</sup> shown in figure 5.3. This increase is due to a transition of physical interaction processes; at the lower energies the dominant interaction is the photo-electric effect experienced by incident and scattered photons in the phosphor, as opposed to Compton interactions in the

overlying copper plate at higher energies. For air this transition occurs at a significantly lower energy.

In figure 5.4 we present the simulated dose response as a function of photon energy with the Cu plate in the contact configuration. As the thickness of the plate is increased, the overall dose to the phosphor goes down. More importantly with the addition of the Cu plate, the dose response in the low energy region is substantially reduced relative to the smaller reductions at higher energies. Increasing the Cu plate thickness enhances this effect. Table 5.1 summarizes the differences between the EPID response and the IIC response for the four scoring bins below 1 MeV for the EPID configurations of Fig. 5.2, 5.4 and 5.5. With increasing thickness of the Cu plate, the reduction in this difference is most evident at the lowest energy. Difference reductions are also observed in the second, third and fourth bins. Figure 5.5 shows the dose response when the Cu plate thickness is kept constant (0.75 cm), but the position of the plate is changed from the contact to the elevated configuration. Below 1 MeV we see a further reduction in the differences between the EPID response and the IIC response when the Cu plate is elevated (see table 5.1). Figure 5.5 also shows that in the elevated configuration the EPID response increases for energies  $> 3$  MeV. This increase, however, is not likely to have a significant effect on the overall EPID response in compensator hardened beams, as the relative spectral changes in this energy range are small compared to those below 1 MeV.

In order to select an optimal elevation for the Cu plate, additional dose response simulations were performed at 0.375 MeV with a 0.5 cm Cu plate. Elevations between 0.0 cm (contact configuration) and 30.0 cm were investigated. Results are shown in Fig. 5.6. At 15 cm and beyond the curve appears to level off. Further, a gap larger than 15 cm was found to present a practical disadvantage with respect to couch clearance of the EPID. Hence a 15 cm gap was adopted for the elevated configuration. While the external Cu plate decreases the number of incident photons seen by the EPID, it also adds to the low energy portion of the spectrum by introducing Compton scattered photons. It is unlikely that electrons produced in the external Cu plate contribute significant additional dose to the phosphor (the CSDA range in Cu for a Compton electron of the mean energy produced from a 1 MeV photon is  $\sim 0.3$  mm, which is less than the thickness of the internal Cu plate). By introducing a gap between the external Cu plate and the EPID, the fluence of scattered photons incident on the EPID will be reduced as the photons spread out over a larger area.

### *5.3.1.3 Simulated Calibration Curve*

With estimates available for both the photon energy spectrum emerging from the compensator and the dose response of the EPID, we were able to create simulated calibration curves for different beam/detector configurations using Eq's. 5.1 and 5.2. Figure 5.7 presents such calibration curves at SDD = 105 cm for the conventional setup as well as for 0.75 cm of Cu placed in the contact and elevated configurations.



The data is normalized to the open field, SDD=105 cm result (zero steel shot thickness) in the upper right hand corner. As the compensator thickness is increased, both the ion chamber response and dose to the phosphor are reduced. The data in the lower left hand corner corresponds to the response when the beam is attenuated by a 4.5 cm thick steel shot compensator. For the conventional setup there is a distinct curvature in the calibration curve. The curvature is reduced by adding Cu at the surface of the EPID cassette, and reduced even further by introducing a 15 cm gap between the Cu and the cassette surface.

The maximum difference between the open field calibration curve and the attenuated field calibration curve for each case investigated was evaluated using Eq. 5.5. With the EPID in its conventional configuration, the Monte Carlo simulations predicted a maximum difference of 10.6% at  $\mathfrak{R}_{IC}|_{\max d} = 0.58$ , which corresponds to attenuation through  $\sim 2.6$  cm of steel shot. The shapes of the attenuated curves exhibit a definite curvature for higher relative IIC readings, but are well approximated by straight lines for lower readings (below  $\mathfrak{R}_{IC} \approx 0.65$ ). A linear fit to the lowest five points of the attenuated curve with the EPID in the conventional configuration has a squared correlation coefficient of 0.9999. However, a quadratic form incorporating all of the data points was chosen to fit to this and the other attenuated curves. The simulations including an external Cu plate show a clear reduction in the maximum difference between open and attenuated field curves as Cu thickness increases. For example, adding 1 cm of Cu cuts the maximum difference from 10.6%

to 5.5% in the contact configuration and 2.9% in the elevated configuration. These results, summarized in figure 5.8, motivated a subsequent experimental investigation.

### 5.3.2 *Experimental Measurements*

#### 5.3.2.1 *Calibration Curve*

Results for both open and attenuated beam measurements at 6 MV are shown in figure 5.9. The EPID was deployed at two distances, SDD = 105 and 140 cm, for the attenuated beam measurements. At both SDD's we have normalized the pixel values to the open field value at the same SDD. Uncertainty in the ion chamber and EPID readings is approximately 0.5 % and 1%, respectively, so error bars are approximately the same size as the data symbols. Linear fits to the open field data and quadratic fits to the attenuated field data are also shown. Due to the limited deployment range of the EPID, the majority of the attenuated beam data at 140 cm SDD (fig. 5.9b) lies to the left of the open field data. The linear fit to the open field data has been extrapolated to illustrate the discrepancy between the open and attenuated beam measurements. The maximum differences are 8.2% (105 cm SDD) and 7.7% (140 cm SDD) occurring at  $\mathfrak{R}_{IC}$  values of 0.54 and 0.29 respectively. A quick survey of 200 compensator central axis thickness measurements made at our center yielded a mean value of approximately 1.5 cm, which translates into a typical difference of 6.2% at 105 cm SDD.

At 15 MV the difference between EPID pixel values for an open beam at 142 cm SDD and a beam attenuated by 3.5 cm of steel shot at 105 cm SDD was  $< 0.2\%$ , the same difference as observed with the ion chamber. This result supports the idea that EPID dose calibration differences resulting from beam hardening are much less significant for high energy beams than for lower energy beams.

Figure 5.10 depicts the effects on the 105 cm SDD calibration curves when  $0.945 \pm 0.006$  cm of Cu is added to the cassette in the contact and elevated configurations. The maximum difference from the ideal calibration curve is reduced from 8.2% for the conventional configuration to 6.4% (contact) and 3.2% (elevated). It was found that the maximum difference occurred at  $\mathfrak{R}_{IC|_{\max d}} = 0.50 \pm 0.02$  for all Cu thicknesses tested, corresponding to a steel shot compensator thickness of  $\sim 3.5$  cm. Note that the results are expressed as a percentage of

$\mathfrak{R}_{EPID}^{\text{open}}(\mathfrak{R}_{IC|_{\max d}} = 0.50 \pm 0.02)$  (see Eq. 5.6). Figure 5.11 plots the magnitude of the maximum difference as it changes with Cu thickness for both configurations. We see that in the elevated configuration there is a substantial reduction in the discrepancy with Cu thickness, whereas in the contact configuration considerably more Cu is necessary to achieve an equivalent reduction. We see that 1.0 cm of Cu reduces the difference from 8.2% to 6.1% and 3.0% in the contact and elevated configurations, respectively.

When the beam was hardened by solid water rather than steel shot a similar dose-calibration curve difference was observed. This indicates that the observed

difference is not unique to the imaging of steel shot compensators, and could present a significant dose calibration error in situations involving a beam attenuated by a patient. These results are summarized in Fig. 5.12. In this case the EPID was deployed at 140 cm SDD and the point of maximum discrepancy occurred outside of the open field data range. The maximum difference from the ideal calibration curve for the conventional configuration was found to be 6.5% (at  $\mathfrak{R}_{IC} = 0.57$ ). Adding  $0.630 \pm 0.04$  cm of Cu in the elevated configuration reduced the maximum discrepancy to 3.7%.

### 5.3.2.2 Imaging Performance

It was found that adding an external Cu plate substantially affects both the CNR and the MTF of the system. In figure 5.13 we plot the CNR as a function of Cu thickness, normalized to the value obtained for the conventional configuration. The elevated configuration is observed to have a more substantial reduction in CNR for a given thickness of Cu. A thickness of 1 cm reduces the CNR by approximately 21% and 28% in the contact and elevated configurations, respectively. The  $f_{50}$  values reported by the software were found to be reasonably constant ( $0.41$  lp/mm  $\pm 2\%$  in both configurations) even as the Cu thickness was increased to a thickness of 1.26 cm. A summary of the  $f_{50}$  values is presented in table 5.2. This result however may be misleading as the MTF values are expressed relative to that for the largest bar pattern ( $0.76$  lp/mm). Figure 5.14 shows the relative change in MTF from the conventional setup as the Cu thickness is increased. The change at all spatial frequencies for a given thickness is very similar for both configurations, indicating

that the shape of the MTF does not vary much. The magnitude of the modulation transfer decreases by  $38 \pm 1 \%$  and  $39 \pm 2 \%$  for a Cu thickness of 1 cm in the contact and elevated configurations, respectively.

## 5.4 DISCUSSION

Our results indicate that variations in the incident photon spectrum at low beam energies (eg. 6 MV) can lead to quantifiable differences in EPID dose calibration curves. The deviation from an ideal open field calibration curve is correctable to a limited extent by the addition of an external Cu plate, but at a cost of reduced image quality.

The Monte Carlo simulations conducted support our conceptual understanding of the dose response of the EPID in the conventional configuration (see Fig. 5.2). Compared to an IIC response, the simulations demonstrate an enhanced sensitivity to low energy ( $< 1$  MeV) photons and a fairly similar response at higher energies. We believe it is the low-energy photon interactions in the screen that result in the observed dose calibration differences between open and attenuated beams. Spectral differences in steel shot hardened beams are greatest below 1 MeV (see Fig. 5.1), which makes the detector response in this energy range quite important.

Estimating the EPID's dose response from first principles is not a simple task. There are a number of physical processes at work, but in general, the similarity of the

EPID's response to that of the IIC for energies  $> 1$  MeV is due to the fact that the Compton interaction is dominant in this regime for both detectors. Because this interaction is independent of atomic number ( $Z$ )<sup>21</sup> we expect similar behavior. The photo-electric effect however exhibits a strong dependence on  $Z$ ,<sup>21</sup> explaining the differences observed for energies  $< 1$  MeV. In order to derive an estimate of the EPID's dose response above 1 MeV, one has to first consider that the dose to the EPID's phosphor is primarily due to electrons emerging from the internal Cu plate<sup>8,22</sup> (due to build-up). A plot of the total interaction coefficient with energy for Cu is shown in Fig. 5.3. In Cu, the Compton interaction dominates between  $\sim 0.13$  MeV and  $\sim 9$  MeV,<sup>20</sup> although between 1 and 6 MeV we also expect some contributions from pair production. In addition to electrons from the internal Cu plate, there are other significant factors at play as well. For example, the dose contribution to the phosphor from incident and scattered MV photons interacting in it is not negligible. In the 1-6 MeV incident photon energy range the Compton interaction is also dominant in gadolinium oxysulfide.<sup>20</sup> To predict the EPID's dose response, one has to consider both the energy-dependent effects of build-up, and the charged-particle range limits that determine the extent of transient charged particle equilibrium in the phosphor itself. However, because the IIC response is based on the mass energy-absorption coefficient for air (see Fig. 5.3) which is dominated by the Compton interaction between  $\sim 0.01$  MeV and  $\sim 25$  MeV,<sup>20</sup> it is not unreasonable to expect that their relative response curves be similar in the 1 – 6 MeV range. It should be obvious at this point why the problem is a good candidate for Monte Carlo simulation.

A transition of dominant processes occurs below 1 MeV in the EPID. For an incident photon energy of 0.5 MeV, the Compton electrons produced in the internal Cu plate are no longer forward peaked and have a CSDA range in Cu of  $\sim 0.1$  mm, further, below 0.13 MeV the dominant interaction in Cu becomes the photoelectric effect. Thus the probability for electrons to escape the Cu plate in this energy range is much reduced. The results of Jaffray *et al.*<sup>8</sup> suggest that below 1 MeV, electrons set in motion in the Cu plate are no longer the dominant contributor to energy deposited in the phosphor. In gadolinium oxysulfide, the photoelectric effect is significant at  $\sim 1$  MeV, but becomes the dominant interaction at  $\sim 0.35$  MeV. The photoelectric cross section increases substantially as incident photon energy decreases below 0.35 MeV, resulting in the shape of the overall mass energy-absorption coefficient seen in figure 5.3. As mentioned, Compton scattering is still the dominant process in air down to  $\sim 0.01$  MeV. Hence, we can expect a deviation in the behaviors of the EPID and IIC response curves below 1 MeV, as seen in Fig. 5.2.

The Monte Carlo simulations predicted trends that were subsequently verified experimentally. There is a significant difference between open and attenuated dose calibration curves in the conventional configuration and this difference increases as the photon spectrum incident on the EPID hardens. The difference is reduced with the addition of an external Cu plate. Note that the differences seen in the Monte Carlo simulation results (Fig. 5.8 and Fig. 5.11) are not exactly the same as those in our experiments, as the simulations are based on a generic Varian 6 MV energy spectrum and a simplified beam geometry (pencil beam passing through compensator models,

and parallel beam geometry). Nonetheless we do note that the Monte Carlo results are consistent with experimental observations within measurement uncertainty.

Ultimately, we need to assess the clinical significance of the observed differences between open and attenuated beam calibration curves. Our results indicate that this problem could yield errors of up to 8.2% for compensator verification measurements, and of up to 6.5% for patient transmission dose measurement. Based on compensator factor data from our center an error of 6.2% could be typically expected for compensator measurements (based on measured versus planned differences, which may include some systematic errors). Without modifying the EPID itself, these errors could presumably be cut in half if a single linear calibration curve is obtained from both the open and attenuated beam data. In this instance the resulting calibration line would lie between both sets of data. Thus, if we wanted to limit the dose calibration difference to  $\pm 2\%$ , we need only reduce the maximum difference to 4%. From the fits to the data in figure 5.11 this could be achieved using an external Cu plate  $\sim 0.7$  cm thick in the elevated configuration. Similarly a reduction of the difference in the contact configuration is feasible, but  $\sim 2.5$  cm of Cu is required to obtain the same result. However, as we have shown, adding an external Cu plate leads to degradation of the MTF and CNR, which is a mitigating factor in achieving an optimal solution. The calibration discrepancies presented are extreme cases (for compensators) and under more typical operational conditions, the degree of beam hardening is expected to be less. For example, a 0.5 cm Cu plate in an elevated configuration coupled with a calibration curve based on



data both from open and attenuated beams would keep the dosimetric uncertainty due to this effect at an acceptable level ( $< 2\%$ ) in many instances. On the other hand, we also note that attenuation due to thick tungsten leaves found in multi-leaf collimators could present even more extreme cases than those addressed here. The additional space required for the Cu in the elevated configuration does however introduce some operational limitations.

On examining the QC-3V results, we see that the CNR and modulation transfer at a given spatial frequency are both reduced by adding Cu. The elevated configuration is associated with a greater reduction in CNR than the contact configuration. Recalling the experimental geometry, the Cu plate is almost directly under the QC-3V phantom in the elevated configuration, whereas in the contact configuration there is a gap of nearly 20 cm between the phantom and the Cu. Photons that have scattered through large angles in the Cu are likely to contribute to background noise in either case. However photons that have scattered through small angles have the potential to enhance contrast in the contact case, but exhibit enough lateral travel in the elevated case to cross between regions of interest, thus decreasing the contrast.

## 5.5 CONCLUSION

With the clinical role of EPIDs expanding to include dosimetry, it becomes increasingly important that dose calibration be as accurate as possible for all beam conditions. In this chapter we demonstrate that for low energy ( $\leq 6$  MV) beams a

change in the incident energy spectrum, as typically occurs when compensators modify the beam, can result in a dose measurement difference as great as 8.2% for a Varian aS500 EPID if an open field calibration curve is used. It is also demonstrated that a similar discrepancy may likewise occur when the EPID is used for patient transmission dosimetry. Monte Carlo simulations confirm that this behavior is due to an increase in the dose response of the EPID phosphor to low energy photons ( $< 1\text{ MeV}$ ). Further, the simulations suggest that the increase in the dose response of the phosphor can be partially mitigated using an external Cu plate to differentially attenuate the low energy portion of the incident photon spectrum. To reduce the maximum difference between the calibration curve for an open field and that for a beam attenuated by steel shot compensator material (maximum difference between an averaged calibration curve and either of the preceding) to  $< 4\%$  ( $< 2\%$ ), an external Cu plate  $\sim 0.7\text{ cm}$  thick is required in the elevated configuration (15 cm above the surface). A Cu plate in contact with the EPID surface can achieve an equivalent reduction, but a thickness of  $\sim 2.5\text{ cm}$  would be required. In the elevated configuration a 0.7 cm thick Cu plate will reduce the CNR by 19%, and the MTF at a given spatial frequency by 30%.

EPID setup \ E bin	0.125 MeV	0.375 MeV	0.625 MeV	0.875 MeV
0.50 cm H <sub>2</sub> O, conv	399	93	39	14
0.50 cm Cu, cont	150	85	36	16
0.75 cm Cu, cont	82	72	30	12
1.25 cm Cu, cont	23	60	25	8
0.75 cm Cu, elev	76	61	21	8

**Table 5.1.** The relative difference (expressed as a percentage of the 1.125 MeV energy bin value) between the EPID energy response and the IIC energy response for the energy bins < 1 MeV. The differences decrease with increasing Cu plate thickness and are smaller with the Cu plate in the elevated configuration compared to the contact configuration.

Cu thickness (cm)	$f_{50}$ contact (lp/mm)	$f_{50}$ elevated (lp/mm)
conventional	0.410	0.410
0.315	0.407	0.410
0.630	0.408	0.407
0.945	0.413	0.411
1.260	0.406	0.405

**Table 5.2.** The  $f_{50}$  values reported by the PIPSPRO software package. The values as calculated appear to be reasonably constant with increasing Cu thickness.

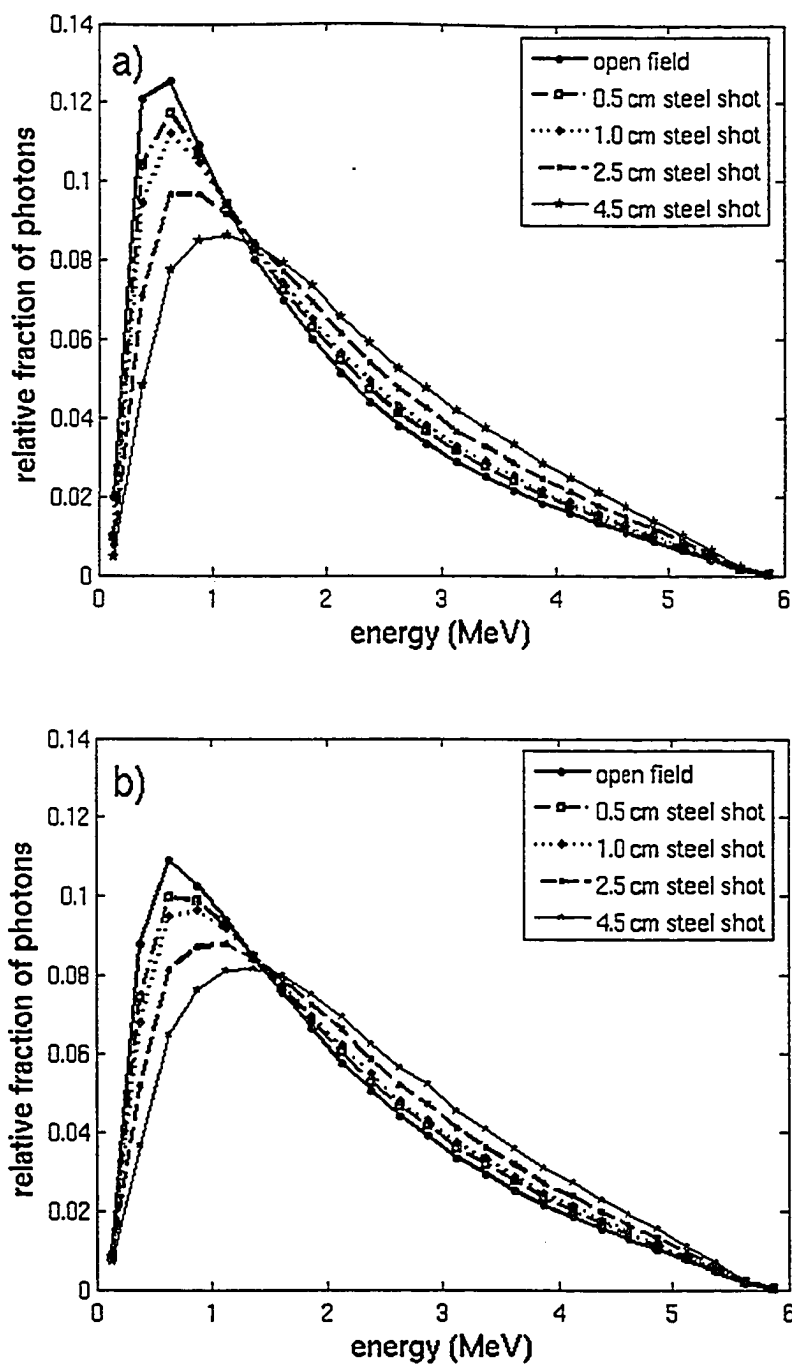


**Figure 5.1.** The relative spectral distribution of photons (normalized to unit area) detected at a plane corresponding to an EPID setup at SDD = 105 cm for increasing steel shot thickness (a). The relative changes between the distributions are reduced with 1.0 cm of Cu placed 15 cm above the detection plane (b).

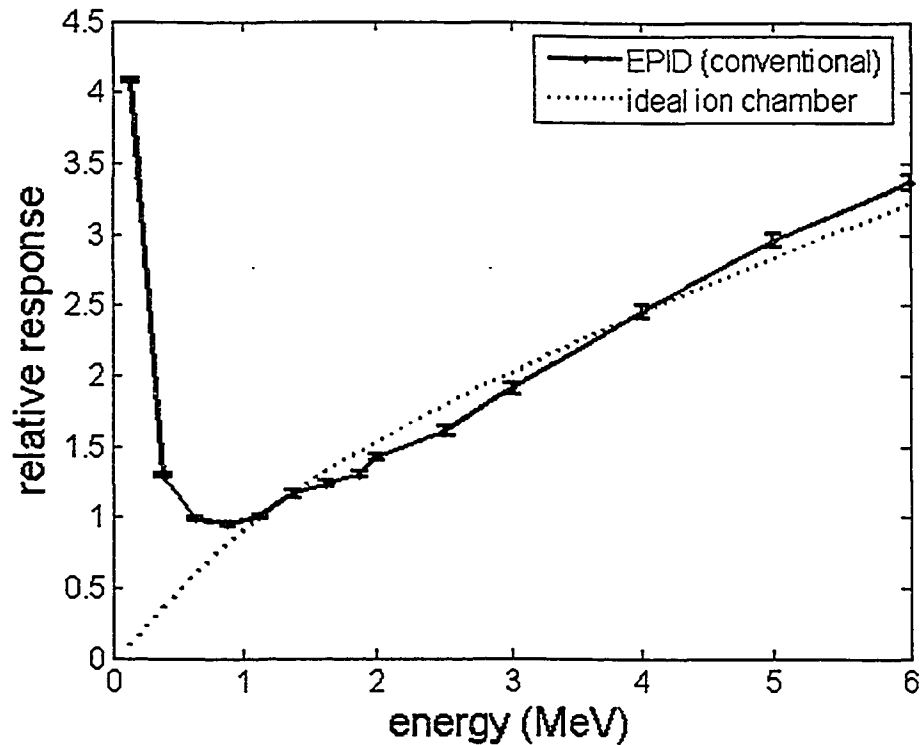


**Figure 5.2.** The relative dose to the EPID phosphor in the conventional setup with 0.5 cm of solid water on its surface, compared to the IIC response. The curves are normalized to one at 1.125 MeV. Above 1 MeV we note that the EPID response is quite similar to the IIC curve (mean difference of 9 %). Below 1 MeV there is a sharp rise in the EPID response due to a transition of dominant interaction processes in the EPID (photo-electric effect dominant), which gives rise to the discrepancy between open and attenuated beam dose calibration curves.

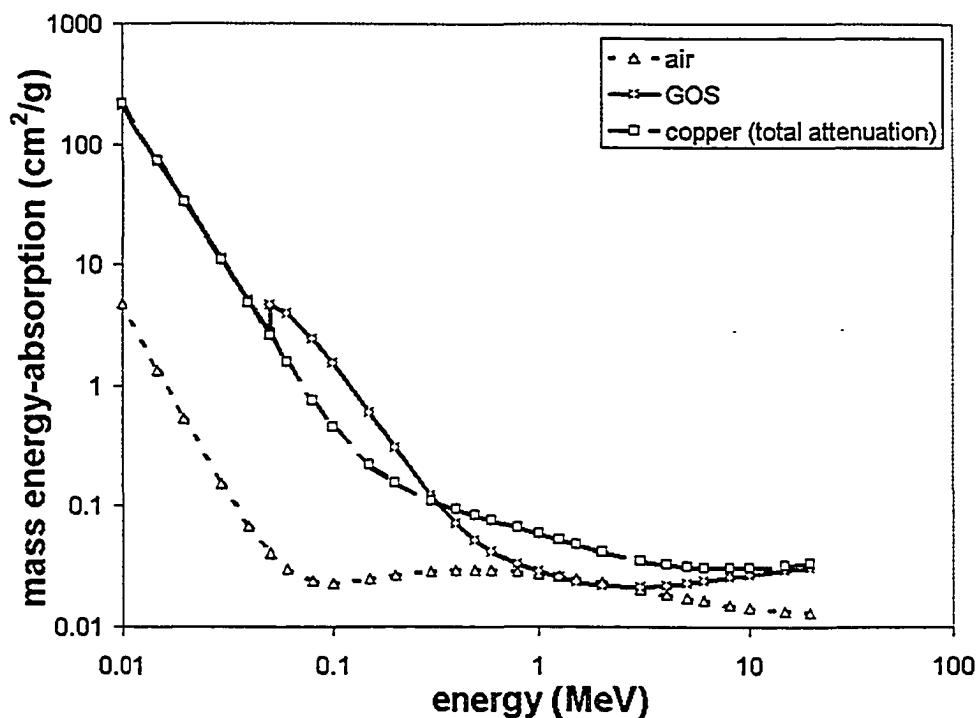
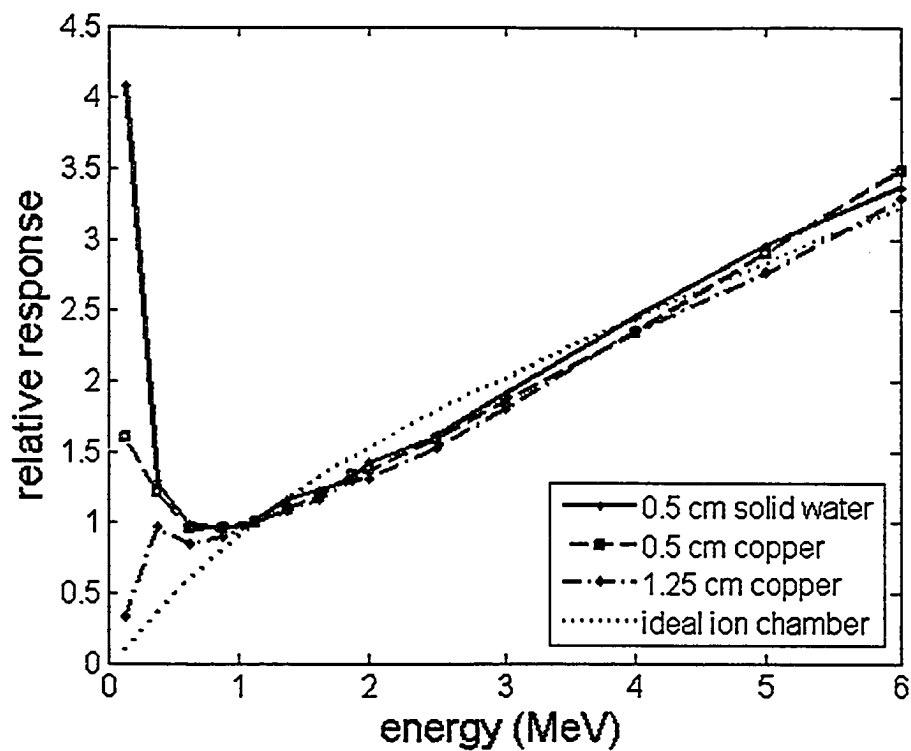
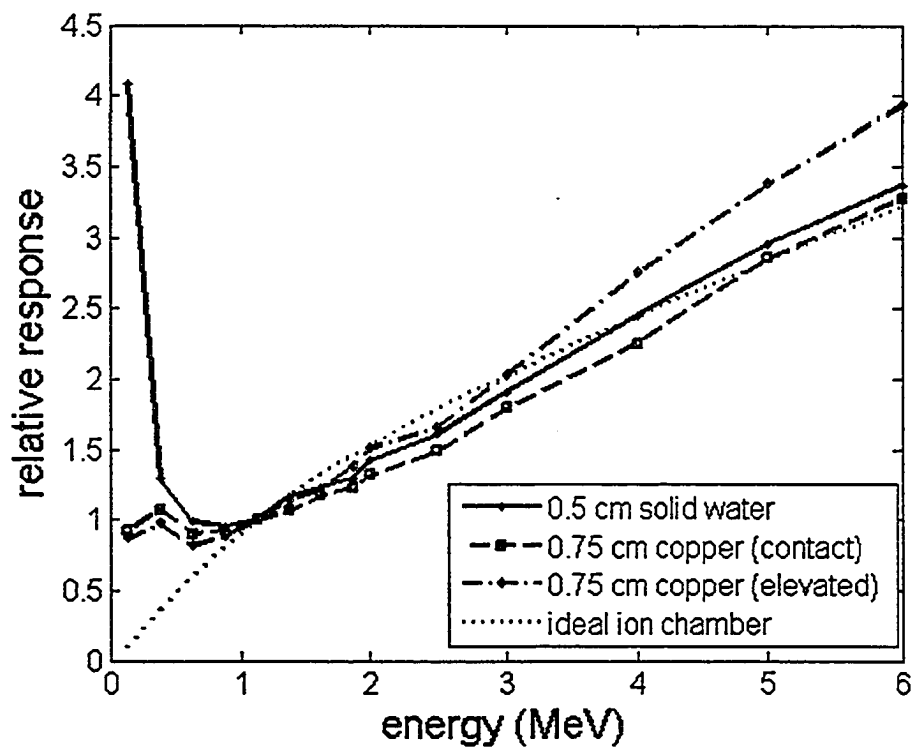


Figure 5.3. Mass energy-absorption coefficients plotted as a function of photon energy for  $\text{Gd}_2\text{O}_2\text{S}$  (GOS) and air.<sup>20</sup> Air has a reasonably uniform coefficient from 0.1 MeV to 20 MeV. GOS however, has a distinct rise below  $\sim 0.5$  MeV. The total attenuation coefficient for Cu has also been plotted to indicate the relative proportion of photons of a given energy that would interact in a Cu plate placed upstream from the phosphor.



**Figure 5.4.** The EPID dose response as a function of photon energy for different thicknesses of Cu plate placed in contact with the surface of the EPID. There is a more substantial reduction in the region below 1 MeV relative to the region above 1 MeV.



**Figure 5.5.** The EPID dose response as a function of photon energy for a 0.75 cm Cu plate in the contact and elevated configurations. Linear fits to the copper plate data above 1 MeV are shown in gray. In the region below 1 MeV, the elevated configuration comes closer to the approximately linear trend observable above 1 MeV than does the contact configuration.



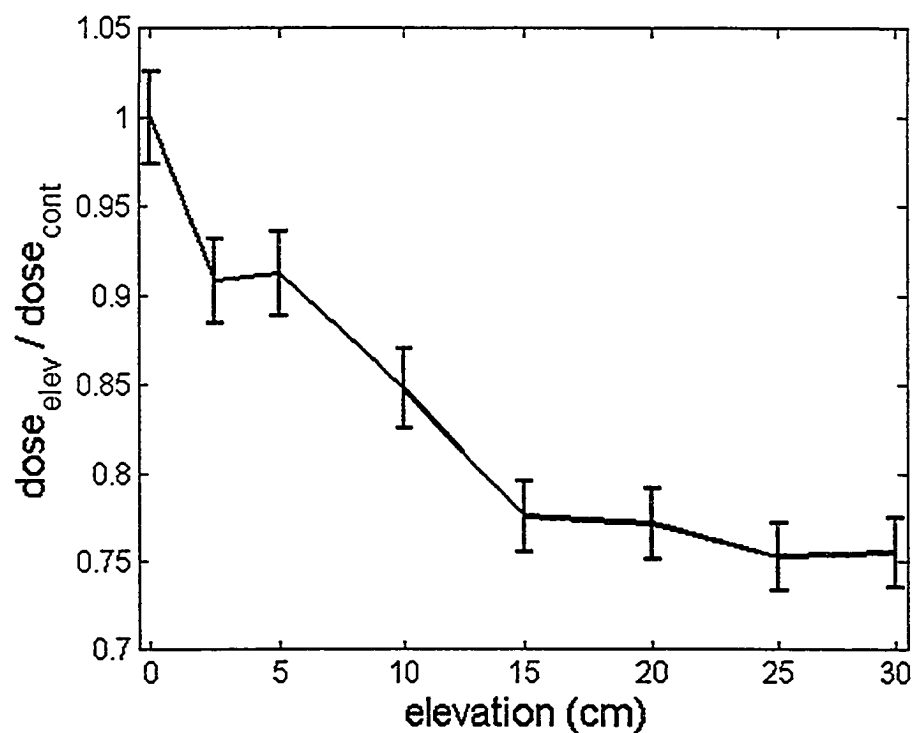


**Figure 5.6.** The ratio of the phosphor dose with the EPID in the elevated configuration to that in the contact configuration for the energy bin centered at 0.375 MeV and a Cu plate thickness of 0.5 cm. Based on this data, an elevation of 15 cm was chosen for subsequent investigations.

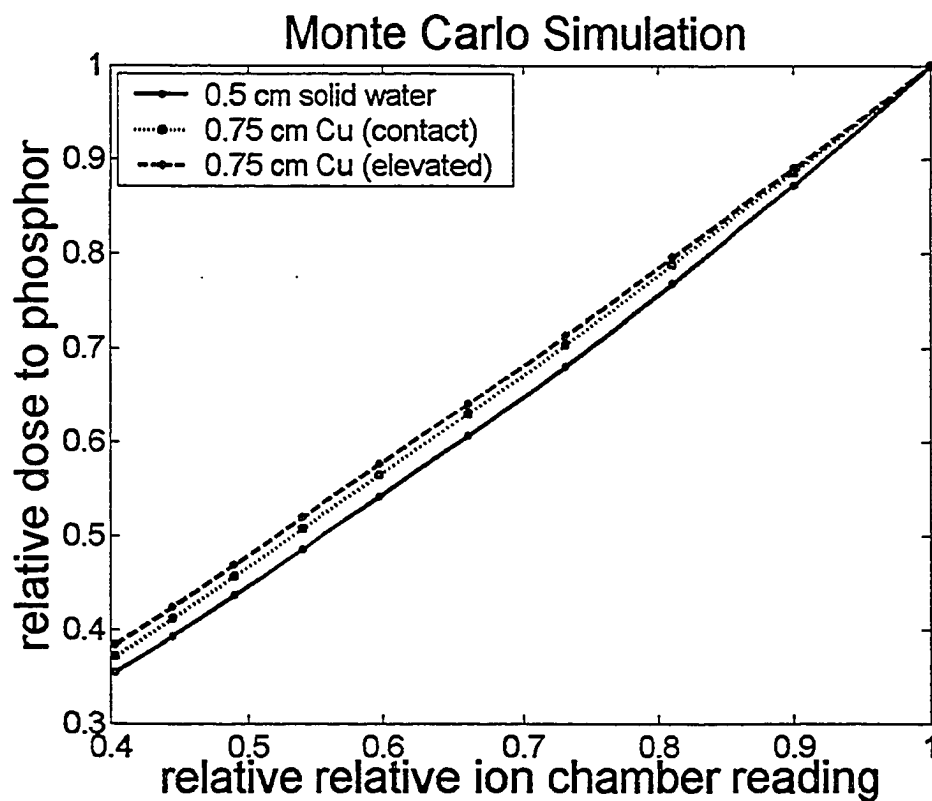


**Figure 5.7.** Monte Carlo simulated calibration curves for a 105 cm SDD attenuated beam scenario. Shown are curves for the conventional setup and for the contact and elevated configurations including a 0.75 cm Cu plate. Results have been normalized to the open field (no compensator) case. The lowest relative doses and ion chamber response correspond to the thickest compensator (4.5 cm steel shot).

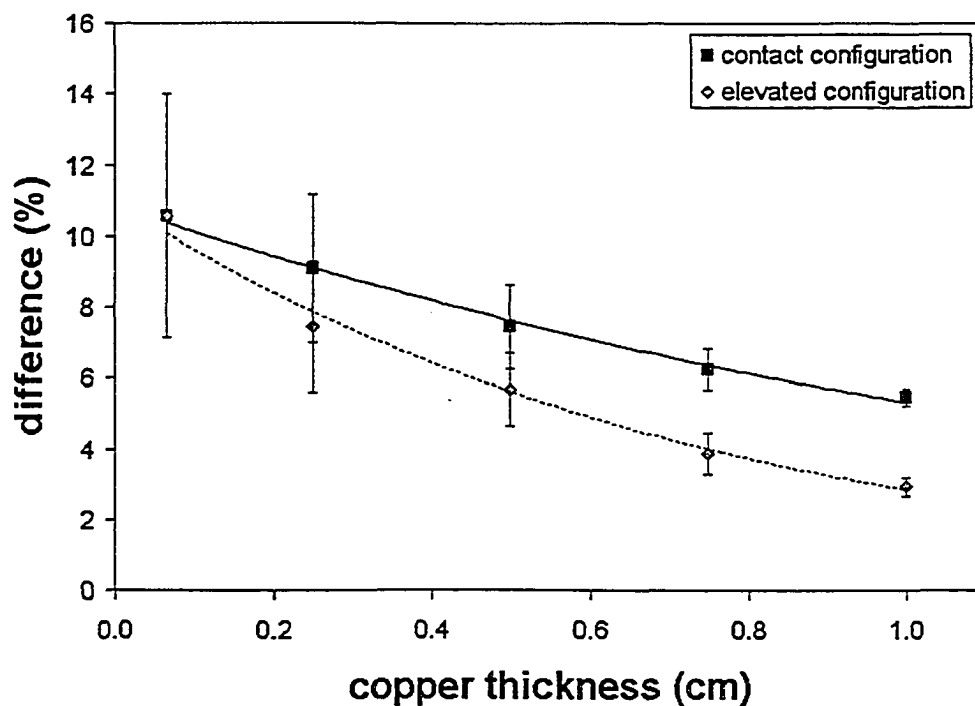


**Figure 5.8.** The maximum difference between an assumed ideal (linear) EPID calibration curve and simulated calibration curves for a beam attenuated by varying thicknesses of steel shot. The error bars derive from uncertainties in the fit coefficients obtained in the regression analysis.

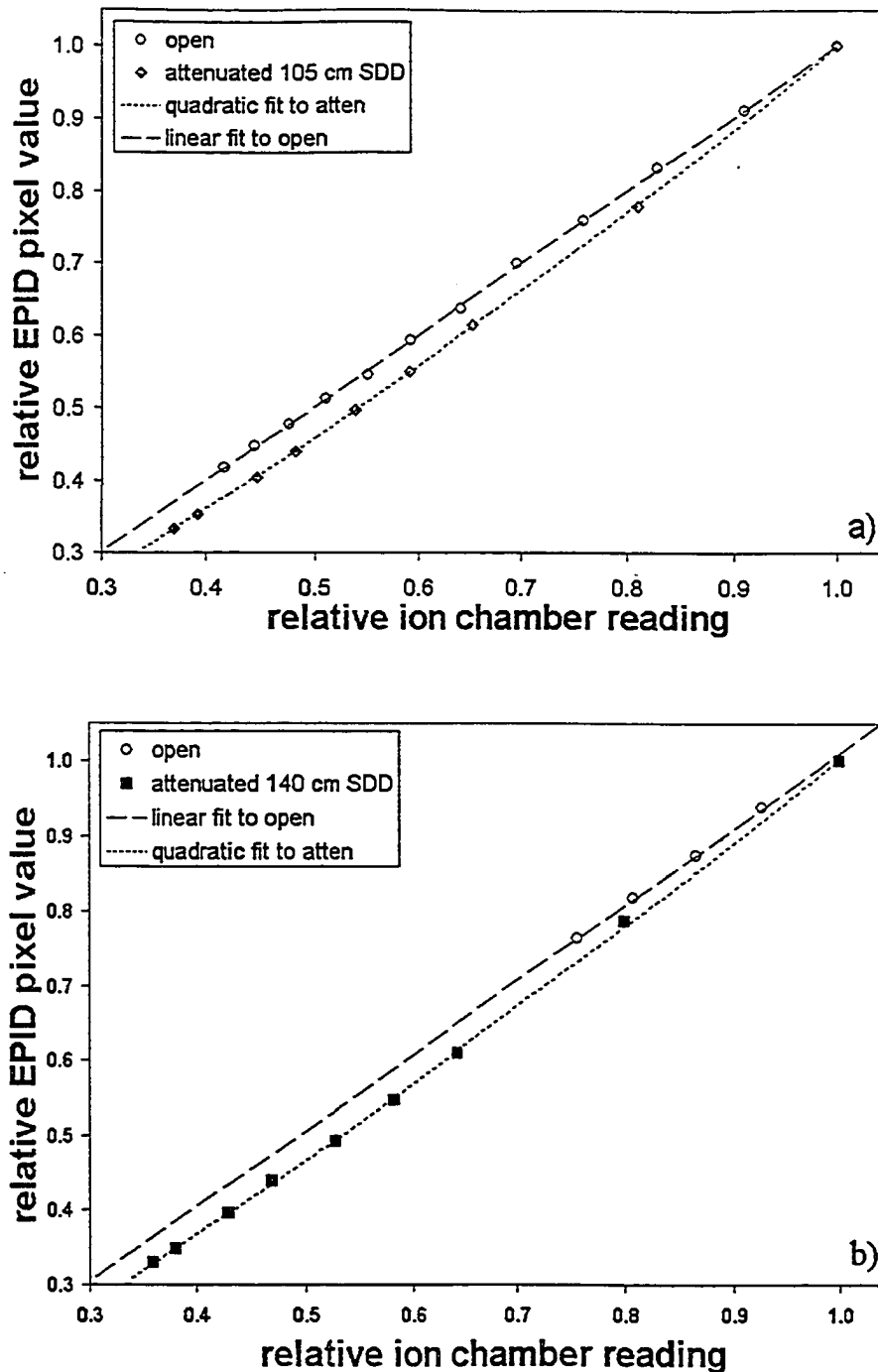


**Figure 5.9.** Experimental calibration curves where the attenuated beam measurements were made at 105 cm SDD (a) and 140 cm SDD (b) respectively. Maximum differences between the attenuated beam data and the open field trend lines (extrapolated in the 140 cm SDD case) are 8.2% and 7.7% respectively.

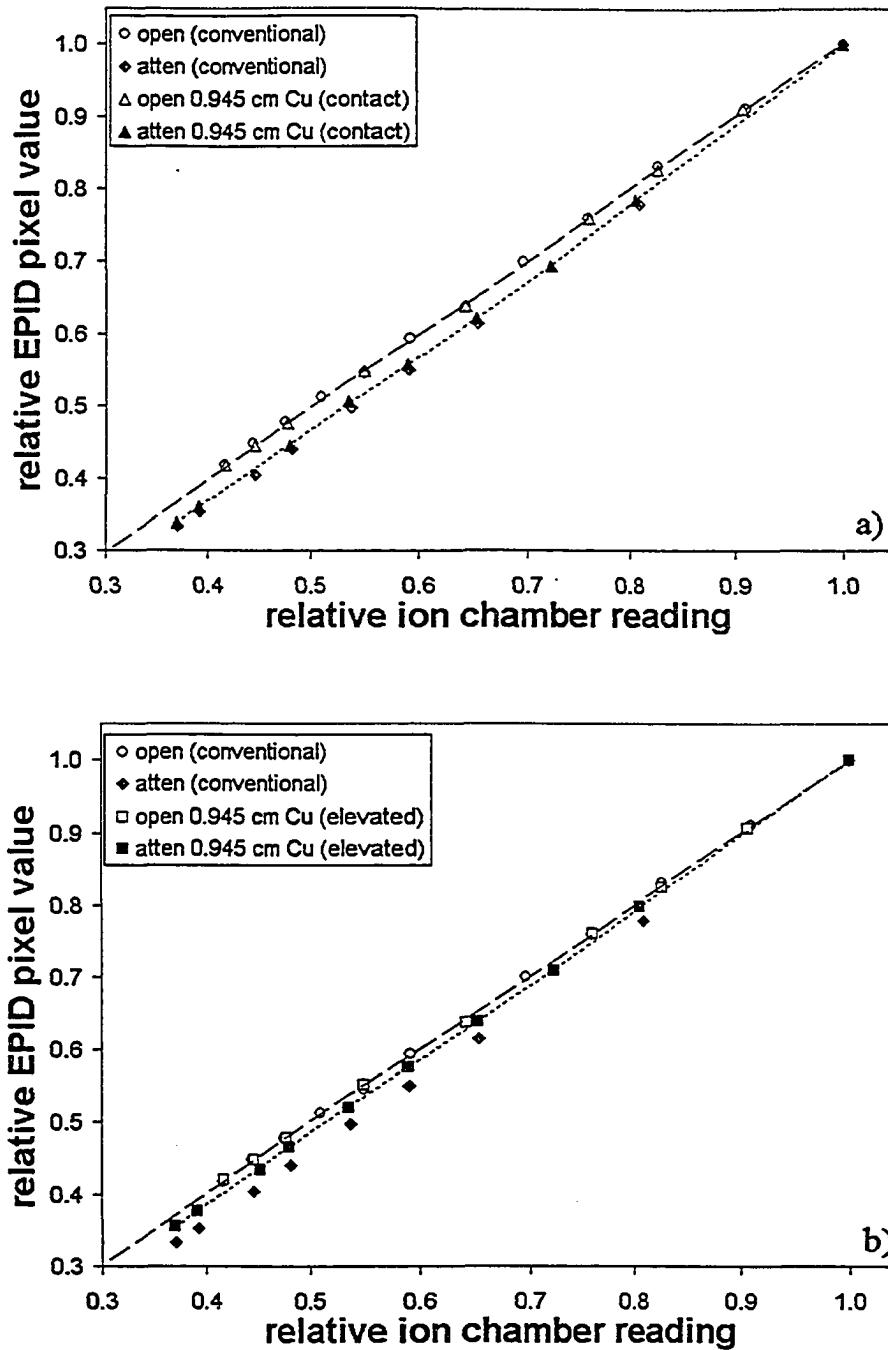


**Figure 5.10.** Calibration curves modified by the addition of 9.45 mm of Cu in the contact (a) and elevated (b) configurations. The maximum deviation was reduced from 8.2% in the conventional setup to 6.4 % in the contact and 3.2 % in the elevated configurations.

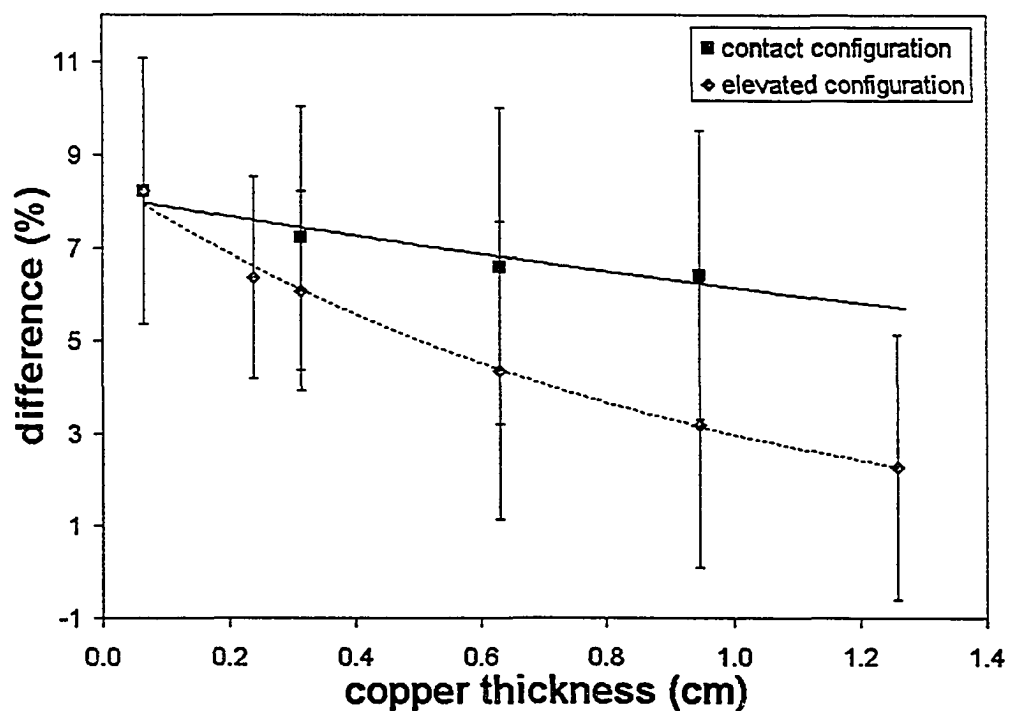


**Figure 5.11.** The maximum discrepancy between the measured EPID response for an open field and an attenuated field at 105 cm SDD as Cu thickness is increased in both the contact and elevated configurations. The error bars derive from uncertainties in the fit coefficients.

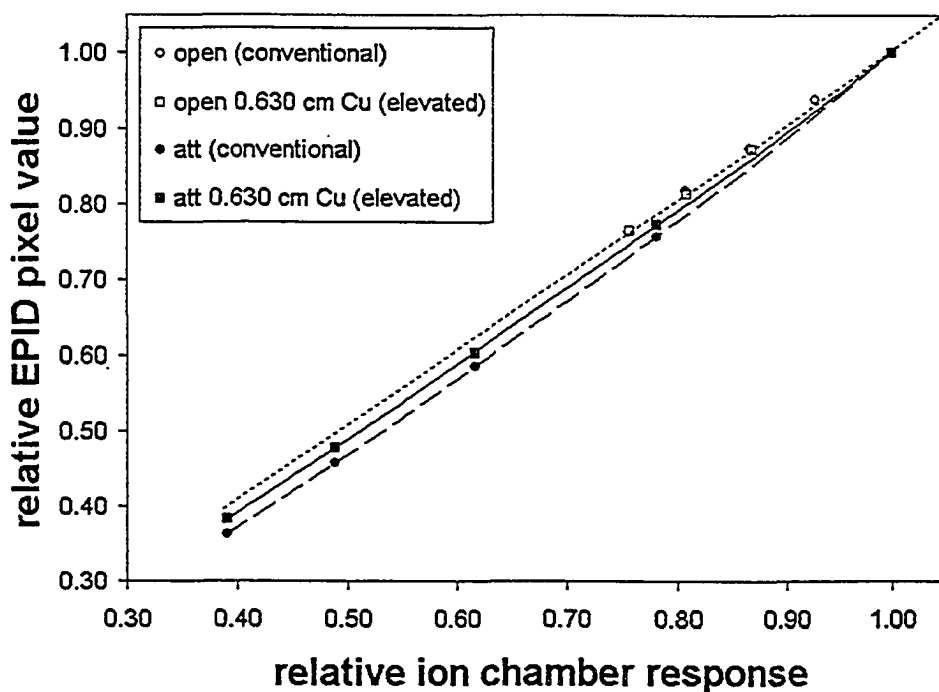


**Figure 5.12.** Calibration curves for the 6 MV beam hardened by a stack of solid water. A similar difference in the curves as for the steel shot was observed, the maximum difference here being 6.5%. Adding  $0.630 \pm 0.04$  cm of Cu in the elevated configuration reduced the maximum difference to 3.7%.

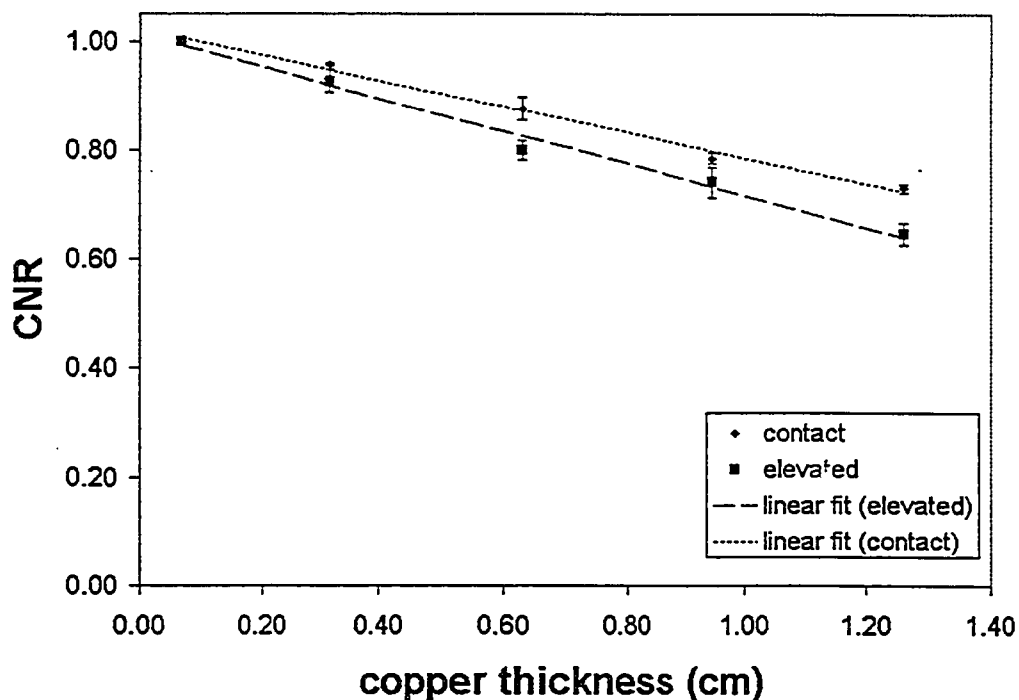


**Figure 5.13.** The relative contrast-to-noise ratio (CNR) as a function of external Cu plate thickness. CNR is reduced substantially in both configurations, but the drop is greatest for the elevated plate case. This is possibly due to a reduction in contrast otherwise present with more scattered photons from the Cu reaching the phosphor in the contact configuration.



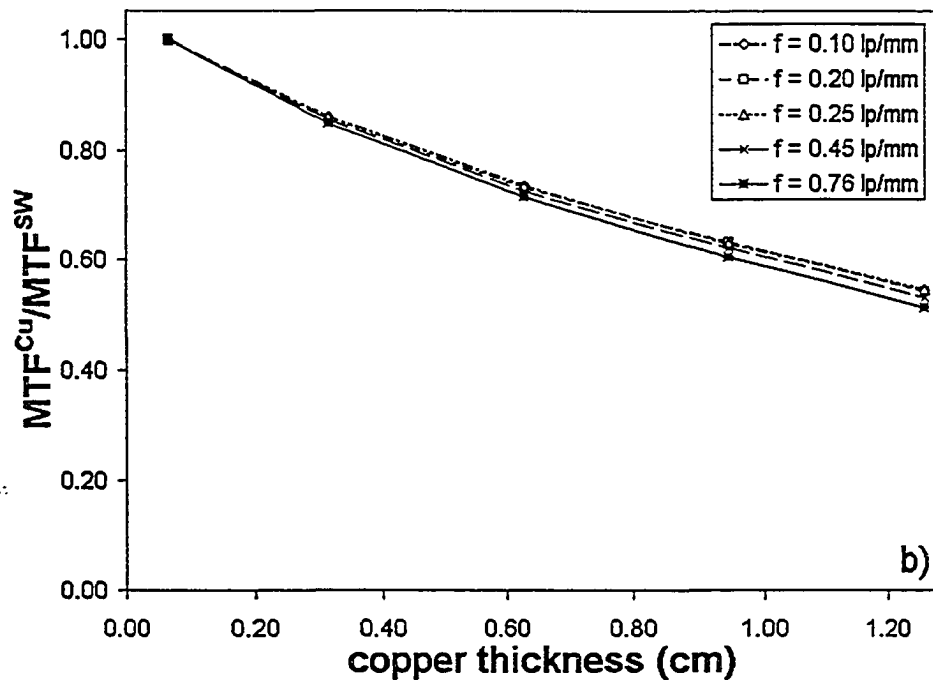
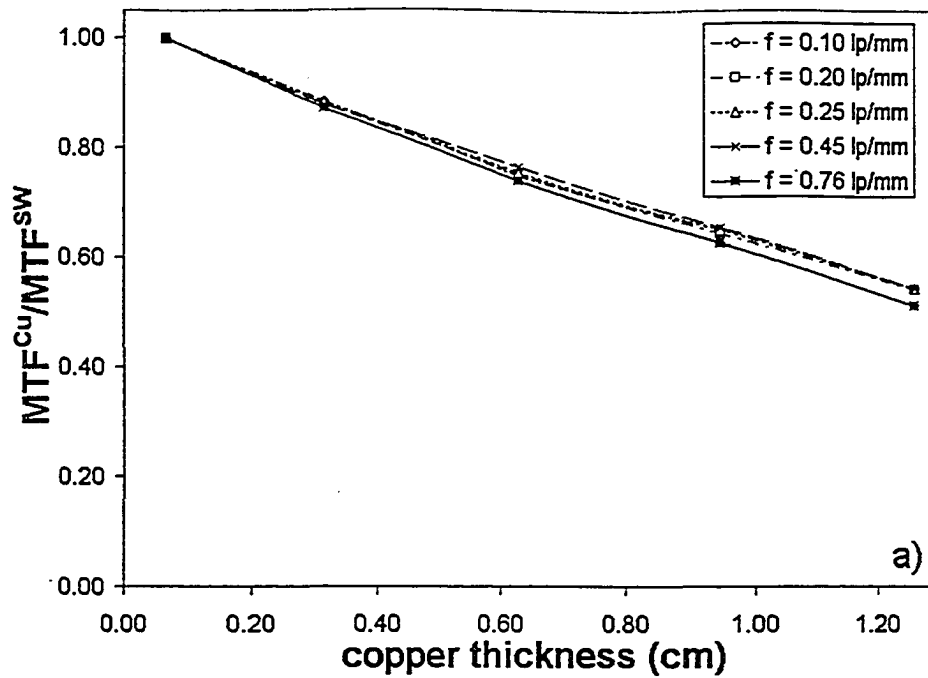


Figure 5.14. Ratio of  $MTF^{Cu}$  to  $MTF^{SW}$  for the conventional configuration vs. Cu thickness measured using the QC-3V phantom for the contact (a) and elevated (b) configurations.

## 5.6 REFERENCES

- <sup>1</sup>J. Chang and C. C. Ling, "Using the frame averaging of aS500 EPID for IMRT verification," *J Appl Clin Med Phys* 4 (4), 287-99 (2003).
- <sup>2</sup>B. M. McCurdy, K. Luchka, and S. Pistorius, "Dosimetric investigation and portal dose image prediction using an amorphous silicon electronic portal imaging device," *Med Phys* 28 (6), 911-24 (2001).
- <sup>3</sup>L. N. McDermott, R. J. Louwe, J. J. Sonke, M. B. van Herk, and B. J. Mijnheer, "Dose-response and ghosting effects of an amorphous silicon electronic portal imaging device," *Med Phys* 31 (2), 285-95 (2004).
- <sup>4</sup>G. V. Menon and R. S. Sloboda, "Compensator quality control with an amorphous silicon EPID," *Med Phys* 30 (7), 1816-24 (2003).
- <sup>5</sup>J. V. Siebers, J. O. Kim, L. Ko, P. J. Keall, and R. Mohan, "Monte Carlo computation of dosimetric amorphous silicon electronic portal images," *Med Phys* 31 (7), 2135-46 (2004).
- <sup>6</sup>B. Warkentin, S. Steciw, S. Rathee, and B. G. Fallone, "Dosimetric IMRT verification with a flat-panel EPID," *Med Phys* 30 (12), 3143-55 (2003).
- <sup>7</sup>B.A. Groh, *A study of the use of flat-panel imagers for radiotherapy verification* (Deutsches Krebsforschungszentrum, Heidelberg, 2001).
- <sup>8</sup>D. A. Jaffray, J. J. Battista, A. Fenster, and P. Munro, "Monte Carlo studies of x-ray energy absorption and quantum noise in megavoltage transmission radiography," *Med Phys* 22 (7), 1077-88 (1995).
- <sup>9</sup>M. Lachaine, E. Fourkal, and B. G. Fallone, "Investigation into the physical characteristics of active matrix flat panel imagers for radiotherapy," *Med Phys* 28 (8), 1689-95 (2001).
- <sup>10</sup>M. Partridge, B.A. Groh, L. Spies, B. M. Hesse, and T. Bortfeld, "A study of the spectral response of portal imaging detectors," presented at the Proceedings of the IEEE Nuclear Science Symposium, 2000 (unpublished).
- <sup>11</sup>C. Yeboah and S. Pistorius, "Monte Carlo studies of the exit photon spectra and dose to a metal/phosphor portal imaging screen," *Med Phys* 27 (2), 330-9 (2000).
- <sup>12</sup>I. Kawrakow, "Accurate condensed history Monte Carlo simulation of electron transport. II. Application to ion chamber response simulations," *Med Phys* 27 (3), 499-513 (2000).

- <sup>13</sup>I. Kawrakow, "Accurate condensed history Monte Carlo simulation of electron transport. I. EGSnrc, the new EGS4 version," *Med Phys* **27** (3), 485-98 (2000).
- <sup>14</sup>I. Kawrakow and D.W.O. Rogers, *The EGSnrc Code System: Monte Carlo Simulation of Electron and Photon Transport, NRCC Report PIRS-701* (NRCC, Ottawa ON, 2002).
- <sup>15</sup>D. Sheikh-Bagheri and D. W. Rogers, "Monte Carlo calculation of nine megavoltage photon beam spectra using the BEAM code," *Med Phys* **29** (3), 391-402 (2002).
- <sup>16</sup>C. Kirkby and R. S. Sloboda, "Comprehensive Monte Carlo calculation of the point spread function for a commercial a-Si EPID," *Med Phys* **32** (4), 1115-1127 (2005).
- <sup>17</sup>Varian Medical Systems, *Portal Vision aS500 Rel.6 Reference Manual* (Varian Medical Systems Inc., Palo Alto, CA, 2000).
- <sup>18</sup>R. Rajapakshe, K. Luchka, and S. Shalev, "A quality control test for electronic portal imaging devices," *Med Phys* **23** (7), 1237-44 (1996).
- <sup>19</sup>S. Shalev, *PIPSpro User's Guide Version 3.2* (Masthead Imaging Corporation, Nanaimo, BC, 1999).
- <sup>20</sup>M. J. Berger, J. H. Hubbel, S. M. Seltzer, J. S. Coursey, and D. S. Zucker, *XCOM: Photon Cross Section Database (version 1.2)*. [Online] Available: <http://physics.nist.gov/xcom> [2005, January 25]. (National Institute of Standards and Technology, Gaithersburg, MD, 2005).
- <sup>21</sup>H. E. Johns and J. R. Cunningham, *The Physics of Radiology 4th ed.* (Springfield: Charles C. Thomas, Springfield, IL, 1983).
- <sup>22</sup>Y. El-Mohri, L. E. Antonuk, J. Yorkston, K. W. Jee, M. Maolinbay, K. L. Lam, and J. H. Siewerdsen, "Relative dosimetry using active matrix flat-panel imager (AMFPI) technology," *Med Phys* **26** (8), 1530-41 (1999).

## Chapter 6: Summary and Future Directions

### 6.1 SUMMARY

The work presented herein comprises an in-depth study of the physics that underlies the operation of the Varian aS500 EPID. The intent of the present work was to identify means to improve the operational performance of the EPID for dose verification by focusing on blur kernel elucidation and dosimetric calibration. We have been able to provide new insight and to generate workable ideas on both fronts.

Previously, other authors have generated a map of transmission fluence from a raw EPID image using standard deconvolution with an approximate blur kernel.<sup>1</sup> The present work identifies and addresses several outstanding issues in blur kernel identification and fluence measurement, by making use of Monte Carlo techniques to generate a kernel for 6 and 15 MV photons based on a comprehensive model of the detector. The overall kernel incorporates two components: one describing ionising radiation transport and dose deposition, and the other describing the spreading of optical photons passing through the phosphor screen and optical filter. The latter allowed us to understand and quantify the contribution of optical spreading to the overall blurring process, and more importantly, to demonstrate its impact on fluence profile recovery. We measured the line spread function for the EPID, which provided experimental verification for the Monte Carlo results. Further, we fit analytical forms to both the overall and optical blur kernels, in order to facilitate the work of others having an interest in deconvolving EPID images. Finally, we were able to quantify

and compare the accuracy of fluence profile recovery using blur kernels obtained through a variety of means.

An accurate dose calibration curve is necessary when the EPID is used for dosimetric purposes. Other authors have shown that in open fields, where there is little change in the incident photon spectrum, the relation between pixel values and ion chamber readings obtained at a given spatial location is very linear.<sup>1,2</sup> The present work demonstrates that pixel calibration factors can vary by over 8% from their open field counterparts when a 6 MV beam spectrum is hardened by passage through steel shot compensator material. A Monte Carlo investigation of this phenomenon confirmed our suspicion that the discrepancy was due to an increase in the dose response of the integral phosphor screen to lower energy (< 1 MeV) photons. Further, the Monte Carlo simulations suggested that an external copper plate could be used to pre-filter the low energy photons and thereby reduce large shifts in the low energy components of the spectrum that result from beam hardening. This would then produce a more uniform response in measurement situations involving changes to the open field spectrum. This copper plate would be significantly larger than a standard internal copper plate (0.5-1.0 cm versus 0.1 cm). This was verified experimentally, as we were able to generate dose calibration curves with substantially reduced differences between open and attenuated field pixel calibration factors. Images of a standard QA phantom demonstrated that adding the external copper plate did however have the disadvantage of reducing the CNR and relative MTF.

Because of its availability at our centre and large installed commercial base, the aS500 was a natural choice of a-Si EPID to investigate. As discussed in Chapter 4, it was deemed important to focus on a specific EPID model rather than work with a generic detector. Nevertheless many of the findings in the present work can be logically translated to other a-Si EPID models. For example, the variation in EPID pixel calibration factors associated with beam hardening was found to be a property of the high-Z  $\text{Gd}_2\text{O}_2\text{S:Tb}$  screen, and therefore is likely to be observed to a greater or lesser extent in all a-Si EPIDs incorporating a similar screen.

The work presented herein essentially takes an existing 2D MV imaging technology, identifies and quantifies its specific limitations for dose measurement purposes, and through an in-depth study of the underlying physics suggests means by which those limitations may in large part be overcome. In doing so the present work provides demonstrated concepts and techniques to improve 2D clinical dose measurement with an a-Si EPID in radiotherapy.

## **6.2 FUTURE DIRECTIONS**

At the conclusion of the present work the field of portal dosimetry finds itself at an exciting stage. Both the technology and body of knowledge have matured to a point where applications such as 2D and 3D pre-treatment field verification are now possible.<sup>1,3-5</sup> Portal images can be accurately predicted using Monte Carlo techniques,<sup>4</sup> based on the phase space of particles exiting the treatment head of a

linac, and compared with measured images. The natural progression after verifying the energy fluence distribution for an open field is to verify the distribution after transmission through a patient.

With the onset of Monte Carlo treatment planning<sup>6-9</sup>, it will become possible to obtain a prediction of transmitted fluence for individual patients. The corresponding measurement of this fluence via EPID imaging can be used to identify discrepancies between the dose planned and the dose delivered. If a kV or MV CT dataset of the patient in treatment position is available, the primary fluence could be extracted and back-projected through the patient to estimate the 3D distribution of dose accumulated in the patient.<sup>5</sup> Furthermore, this could be done separately for each treatment fraction, which would allow archival of the dose delivered throughout the treatment. Such measurement-based dose monitoring would provide opportunities to modify the dose delivery in order to boost areas where dose is not accumulating as specified by the treatment plan, or to reduce any excessive dose that may be accumulating in organs at risk.

It should also be mentioned that a good deal of the methodology employed in the present work is applicable to other digital MV imaging technologies. For example, the computed radiography (CR) plate is another replacement for film that contains a photostimulable phosphor such as BaFBr:Eu.<sup>10,11</sup> The phosphor traps excited electrons in metastable states, which then emit optical light when the plate is scanned with a laser. A photodetector can be used to read the emissions and generate

a digital image. The advantage of these plates is that they are portable and reusable. In many ways they behave similarly to an a-Si EPID, and so can also potentially be used for dosimetric purposes. As with the present EPID work, Monte Carlo modelling will allow investigators to simulate the response of the phosphor under a variety of irradiation conditions.

It is very likely that forthcoming advances in portal dosimetry will have a significant impact on radiotherapy. Ultimately, such work will lead to improvements in the radiotherapy process by allowing a measurement-based estimate of the dose that accumulates in a patient to be obtained, thereby enabling refinements in dose delivery leading in turn to improved outcomes for cancer patients treated with radiotherapy.



### 6.3 REFERENCES

- <sup>1</sup>B. Warkentin, S. Steciw, S. Rathee, and B. G. Fallone, "Dosimetric IMRT verification with a flat-panel EPID," *Med Phys* **30** (12), 3143-55 (2003).
- <sup>2</sup>G. V. Menon and R. S. Sloboda, "Compensator quality control with an amorphous silicon EPID," *Med Phys* **30** (7), 1816-24 (2003).
- <sup>3</sup>B. Warkentin, "Development of Verification Procedures using a Flat-Panel EPID, and Application and Investigation of Radiobiological Models, for Intensity-Modulated Radiotherapy," Ph.D. Thesis, University of Alberta, 2005.
- <sup>4</sup>J. V. Siebers, J. O. Kim, L. Ko, P. J. Keall, and R. Mohan, "Monte Carlo computation of dosimetric amorphous silicon electronic portal images," *Med Phys* **31** (7), 2135-46 (2004).
- <sup>5</sup>S. Steciw, B. Warkentin, S. Rathee, and B. G. Fallone, "Three-dimensional IMRT verification with a flat-panel EPID," *Med Phys* **32** (2), 600-12 (2005).
- <sup>6</sup>B. A. Fraass, J. Smathers, and J. Deye, "Summary and recommendations of a National Cancer Institute workshop on issues limiting the clinical use of Monte Carlo dose calculation algorithms for megavoltage external beam radiation therapy," *Med Phys* **30** (12), 3206-16 (2003).
- <sup>7</sup>W. van der Zee, A. Hogenbirk, and S. C. van der Marck, "ORANGE: a Monte Carlo dose engine for radiotherapy," *Phys Med Biol* **50** (4), 625-41 (2005).
- <sup>8</sup>I. J. Chetty, J. M. Moran, D. L. McShan, B. A. Fraass, S. J. Wilderman, and A. F. Bielajew, "Benchmarking of the dose planning method (DPM) Monte Carlo code using electron beams from a racetrack microtron," *Med Phys* **29** (6), 1035-41 (2002).
- <sup>9</sup>N. Tyagi, A. Bose, and I. J. Chetty, "Implementation of the DPM Monte Carlo code on a parallel architecture for treatment planning applications," *Med Phys* **31** (9), 2721-5 (2004).
- <sup>10</sup>J. R. Zullo, C. Bloch, P. C. Chi, and R. Kudchadker, "Linearity and uniformity response as an indicator of performance for Agfa ADC-MD10 computed radiography plates," *Med Dosim* **29** (2), 118-21 (2004).
- <sup>11</sup>J. M. Boone, "X-ray Production, Interaction, and Detection in Diagnostic Imaging," in *Handbook of Medical Imaging* (SPIE Press, Bellingham WA, 2000), pp. 1-78.

## Bibliography

- E. A. Alpen, *Radiation Biophysics*, 2 ed. (Academic Press, New York, NY, 1998).  
p: 3
- L. E. Antonuk, K. W. Jee, Y. El-Mohri, M. Maolinbay, S. Nassif, X. Rong, Q. Zhao, J. H. Siewerdsen, R. A. Street, and K. S. Shah, "Strategies to improve the signal and noise performance of active matrix, flat-panel imagers for diagnostic x-ray applications," *Med Phys* 27 (2), 289-306 (2000).  
p: 26
- G. Arfken, *Mathematical Methods for Physicists*, 3 ed. (Academic Press, Orlando FL, 1985).  
p: 81
- ASTRO, *Radiation Therapy for Cancer: Facts to Help Patients Make an Informed Decision*, 2004.  
p: 2
- F H. Attix, *Introduction to Radiological Physics and Radiation Dosimetry* (John Wiley and Sons, New York NY, 1986).  
p: 48
- A. Bakai, M. Alber, and F. Nusslin, "A revision of the gamma-evaluation concept for the comparison of dose distributions," *Phys Med Biol* 48 (21), 3543-53 (2003).  
p: 89
- J. Baro, J. Sempau, J. M. Fernandez-Varea, and F. Salvat, "PENELOPE: an algorithm for Monte Carlo simulation of the penetration and energy loss of electrons and positrons in matter," *Nucl. Instrm. Methods Phys. Res B* 100, 31-46 (1995).  
p: 58
- G. Baroni, G. Ferrigno, R. Orecchia, and A. Pedotti, "Real-time three-dimensional motion analysis for patient positioning verification," *Radiother Oncol* 54 (1), 21-7 (2000).  
p: 4
- M. J. Berger, "Monte Carlo calculation of the penetration and diffusions of fast charged particles," in *Methods in Comput Phys*, edited by B. Alder, S. Fernbach, and M. Rotenberg (Academic, New York, 1963), Vol. 1, pp. 135-215.  
p: 46

M. J. Berger, J. S. Coursey, and D. S. Zucker, *ESTAR, PSTAR, and ASTAR: Computer Programs for Calculating Stopping-Power and Range Tables for Electrons, Protons, and Helium Ions (version 1.2.2)*. [Online] Available: <http://physics.nist.gov/Star> [2005, February 7] (National Institute of Standards and Technology, Gaithersburg, MD, 2005).

p: 31

M. J. Berger, J. H. Hubbel, S. M. Seltzer, J. S. Coursey, and D. S. Zucker, *XCOM: Photon Cross Section Database (version 1.2)*. [Online] Available: <http://physics.nist.gov/xcom> [2005, January 25]. (National Institute of Standards and Technology, Gaithersburg, MD, 2005).

p: 144

A. F. Bielajew, *Fundamentals of the Monte Carlo method for neutral and charged particle transport* (pre-publication manuscript, Ann Arbor MI, 2001).

p: 13

R. Boellaard, M. Essers, M. van Herk, and B. J. Mijnheer, "New method to obtain the midplane dose using portal in vivo dosimetry," *Int J Radiat Oncol Biol Phys* **41** (2), 465-74 (1998).

p: 6

R. Boellaard, M. van Herk, and B. J. Mijnheer, "A convolution model to convert transmission dose images to exit dose distributions," *Med Phys* **24** (2), 189-99 (1997).

p: 6

R. Boellaard, M. van Herk, and B. J. Mijnheer, "The dose response relationship of a liquid-filled electronic portal imaging device," *Med Phys* **23** (9), 1601-11 (1996).

p: 6

W.E. Bolch and E-H. Kim, "Calculations of electron single event distributions for use in internal beta microdosimetry," *Radiat. Prot. Dosim.* **52**, 77-80 (1994).

p: 58

J. M. Boone, "X-ray Production, Interaction, and Detection in Diagnostic Imaging," in *Handbook of Medical Imaging* (SPIE Press, Bellingham WA, 2000), pp. 1-78.

p: 177

T. Bortfeld, J. Burkelbach, R. Boesecke, and W. Schlegel, "Methods of image reconstruction from projections applied to conformation radiotherapy," *Phys Med Biol* **35** (10), 1423-34 (1990).

p: 3

D. Brabbins, A. Martinez, D. Yan, D. Lockman, M. Wallace, G. Gustafson, P. Chen, F. Vicini, and J. Wong, "A dose-escalation trial with the adaptive radiotherapy process as a delivery system in localized prostate cancer: Analysis of chronic toxicity," *Int J Radiat Oncol Biol Phys* 61 (2), 400-8 (2005).

*p: 4*

A. Brahme, "Optimization of stationary and moving beam radiation therapy techniques," *Radiother Oncol* 12 (2), 129-40 (1988).

*p: 3*

National Cancer Institute of Canada, *Canadian Cancer Statistics 2004* (National Cancer Institute of Canada, Toronto, ON, 2004).

*p: 1*

F. Cayouet, C. Moisan, N. Zhang, and C.J. Thompson, "Monte Carlo Modeling of Scintillator Crystal Performance for Stratified PET Detectors with DETECT2000," *IEEE Trans. Nucl. Sci.* 49 (3), 624-628 (2002).

*p:62*

Polymer Learning Center, "Epoxy Resins (Macrogalleria)," (University of Southern Mississippi, Dept. of Polymer Science, <http://www.pslc.ws/mactest/level2.htm>, 2002).

*p: 31*

J. Chang and C. C. Ling, "Using the frame averaging of aS500 EPID for IMRT verification," *J Appl Clin Med Phys* 4 (4), 287-99 (2003).

*p: 85*

I. J. Chetty, J. M. Moran, D. L. McShan, B. A. Fraass, S. J. Wilderman, and A. F. Bielajew, "Benchmarking of the dose planning method (DPM) Monte Carlo code using electron beams from a racetrack microtron," *Med Phys* 29 (6), 1035-41 (2002).

*p: 178*

Fels Company, "The PCB Laminate FAQ," (Fels Company, [http://www.felsweb.com/lam\\_faq.htm](http://www.felsweb.com/lam_faq.htm), 2001).

*p: 31*

C. De Angelis, S. Onori, M. Pacilio, G. A. Cirrone, G. Cuttone, L. Raffaele, M. Bucciolini, and S. Mazzocchi, "An investigation of the operating characteristics of two PTW diamond detectors in photon and electron beams," *Med Phys* 29 (2), 248-54 (2002).

*p: 88*

J. T. Dobbins III, "Image Quality Metrics for Digital Systems," in *Handbook of Medical Imaging* (SPIE Press, Bellingham WA, 2000), pp. 161-222.

p: 91

R. Eckhardt, "Stan Ulam, John von Neumann, and the Monte Carlo method," *Los Alamos Science* **15**, 131-137 (1987).

p: 42

Y. El-Mohri, L. E. Antonuk, J. Yorkston, K. W. Jee, M. Maolinbay, K. L. Lam, and J. H. Siewerdsen, "Relative dosimetry using active matrix flat-panel imager (AMFPI) technology," *Med Phys* **26** (8), 1530-41 (1999).

p: 9

Y. El-Mohri, K. W. Jee, L. E. Antonuk, M. Maolinbay, and Q. Zhao, "Determination of the detective quantum efficiency of a prototype, megavoltage indirect detection, active matrix flat-panel imager," *Med Phys* **28** (12), 2538-50 (2001).

p: 10

M. Essers, B. R. Hoogervorst, M. van Herk, H. Lanson, and B. J. Mijnheer, "Dosimetric characteristics of a liquid-filled electronic portal imaging device," *Int J Radiat Oncol Biol Phys* **33** (5), 1265-72 (1995).

p: 9

C. Fiorino, A. del Vecchio, G. M. Cattaneo, M. Fusca, B. Longobardi, P. Signorotto, and R. Calandrino, "Exit dose measurements by portal film dosimetry," *Radiother Oncol* **29** (3), 336-40 (1993).

p: 6

G.S. Fishman, *Monte Carlo Concepts, Algorithms and Applications*, 1 ed. (Springer Verlag, London, 1996).

p: 11

B. A. Fraass, J. Smathers, and J. Deye, "Summary and recommendations of a National Cancer Institute workshop on issues limiting the clinical use of Monte Carlo dose calculation algorithms for megavoltage external beam radiation therapy," *Med Phys* **30** (12), 3206-16 (2003).

p: 177

H. Fujita, K. Doi, and M. L. Giger, "Investigation of basic imaging properties in digital radiography. 6. MTFs of II-TV digital imaging systems," *Med Phys* **12** (6), 713-20 (1985).

p: 82

R. C. Gonzalez and R. E. Woods, *Digital Image Processing* (Addison-Wesley, Don Mills ON, 1992).

p: 76

P. B. Greer and C. C. Popescu, "Dosimetric properties of an amorphous silicon electronic portal imaging device for verification of dynamic intensity modulated radiation therapy," *Med Phys* **30** (7), 1618-27 (2003).

*p: 27*

B.A. Groh, *A study of the use of flat-panel imagers for radiotherapy verification* (Deutsches Krebsforschungszentrum, Heidelberg, 2001).

*p: 131*

B. H. Hasegawa, *The Physics of Medical X-Ray Imaging*, 2 ed. (Medical Physics Publishing, Madison WI, 1991).

*p: 84*

A. G. Haus and J. E. Marks, "Detection and evaluation of localization errors in patient radiation therapy," *Invest Radiol* **8** (6), 384-91 (1973).

*p: 4*

B. J. Heijmen, K. L. Pasma, M. Kroonwijk, V. G. Althof, J. C. de Boer, A. G. Visser, and H. Huizenga, "Portal dose measurement in radiotherapy using an electronic portal imaging device (EPID)," *Phys Med Biol* **40** (11), 1943-55 (1995).

*p: 8*

M. G. Herman, R. A. Abrams, and R. R. Mayer, "Clinical use of on-line portal imaging for daily patient treatment verification," *Int J Radiat Oncol Biol Phys* **28**, 1017-1023 (1994).

*p: 4*

ICRU, ICRU Report 37: Stopping Powers for Electrons and Positrons, 1984.

*p: 49*

ICRU, ICRU Report 36: Microdosimetry, 1983.

*p: 53*

ICRU, ICRU Report 24: Determination of absorbed dose in a patient irradiated by beams of X or gamma rays in radiotherapy procedures, 1976.

*p: 4*

D. A. Jaffray, J. J. Battista, A. Fenster, and P. Munro, "Monte Carlo studies of x-ray energy absorption and quantum noise in megavoltage transmission radiography," *Med Phys* **22** (7), 1077-88 (1995).

*p: 29*

F. James, "RANLUX: A Fortran implementation of the high-quality pseudorandom number generator of Luscher," *Computer Phys Commun* **79**, 111-114 (1994).

*p: 44*

H. E. Johns and J. R. Cunningham, *The Physics of Radiology 4th ed.* (Springfield: Charles C. Thomas, Springfield, IL, 1983).

*p: 5*

C. Kausch, B. Schreiber, F. Kreuder, R. Schmidt, and O. Dossel, "Monte Carlo simulations of the imaging performance of metal plate/phosphor screens used in radiotherapy," *Med Phys* **26** (10), 2113-24 (1999).

*p: 34*

I. Kawrakow, "Accurate condensed history Monte Carlo simulation of electron transport. II. Application to ion chamber response simulations," *Med Phys* **27** (3), 499-513 (2000).

*p: 78*

I. Kawrakow, "Accurate condensed history Monte Carlo simulation of electron transport. I. EGSnrc, the new EGS4 version," *Med Phys* **27** (3), 485-98 (2000).

*p: 48*

I. Kawrakow and A. F. Bielajew, "On the condensed history technique for electron transport," *Nuclear Instruments and Methods* **142B**, 253-280 (1998).

*p: 51*

I. Kawrakow and D.W.O. Rogers, *The EGSnrc Code System: Monte Carlo Simulation of Electron and Photon Transport, NRCC Report PIRS-701* (NRCC, Ottawa ON, 2002).

*p: 53*

A. M. Kellerer, "Chord-length distributions and related quantities for spheroids," *Radiat. Res.* **98**, 425-37 (1984).

*p: 56*

E-H. Kim, W.E. Bolch, W. D. Reece, and J. D. Poston, "A microdosimetric algorithm for electron point kernel data: 1. Monoenergetic electron sources," *Radiat. Prot. Dosim.* **63**, 245-52 (1996).

*p: 58*

C. Kirkby and R. S. Sloboda, "Consequences of the spectral response of an a-Si EPID and implications for dosimetric calibration," *Med Phys* **32** (8), 2649-2658 (2005).

*p: 15*

C. Kirkby and R. S. Sloboda, "Comprehensive Monte Carlo calculation of the point spread function for a commercial a-Si EPID," *Med Phys* **32** (4), 1115-1127 (2005).

*p: 15*

E. E. Klein and D. A. Low, "Interleaf leakage for 5 and 10 mm dynamic multileaf collimation systems incorporating patient motion," *Med Phys* **28** (8), 1703-10 (2001).

*p: 4*

G. F. Knoll, T. F. Knoll, and Henderson T. M., "Light Collection Scintillation Detector Composites for Neutron Detection," *IEEE Trans. Nucl. Sci.* **35** (1), 872-875 (1988).

*p: 60*

L. Ko, J. O. Kim, and J. V. Siebers, "Investigation of the optimal backscatter for an aSi electronic portal imaging device," *Phys Med Biol* **49** (9), 1723-38 (2004).

*p: 76*

M. Lachaine, E. Fourkal, and B. G. Fallone, "Investigation into the physical characteristics of active matrix flat panel imagers for radiotherapy," *Med Phys* **28** (8), 1689-95 (2001).

*p: 9*

M. Lachaine, E. Fourkal, and B. G. Fallone, "Detective quantum efficiency of a direct-detection active matrix flat panel imager at megavoltage energies," *Med Phys* **28** (7), 1364-72 (2001).

*p: 24*

H. W. Lewis, "Multiple Scattering in an Infinite Medium," *Phys. Rev.* **78**, 526-529 (1950).

*p: 51*

D. A. Low, W. B. Harms, S. Mutic, and J. A. Purdy, "A technique for the quantitative evaluation of dose distributions," *Med Phys* **25** (5), 656-61 (1998).

*p: 89*

G. Lubberts, "Random Noise Produced by X-Ray Fluorescent Screens," *J. Opt. Soc. Am.* **58**, 1475-1483 (1968).

*p: 77*

M. Luscher, "A portable high-quality random number generator for lattice field theory simulations," *Computer Phys Commun* **79**, 100-110 (1994).

*p: 44*

C. M. Ma, E. Mok, A. Kapur, T. Pawlicki, D. Findley, S. Brain, K. Forster, and A. L. Boyer, "Clinical implementation of a Monte Carlo treatment planning system," *Med Phys* **26** (10), 2133-43 (1999).

*p: 4*

T. R. Mackie, J. Balog, K. Ruchala, D. Shepard, S. Aldridge, E. Fitchard, P. Reckwerdt, G. Olivera, T. McNutt, and M. Mehta, "Tomotherapy," *Semin Radiat Oncol* **9** (1), 108-17 (1999).

*p: 4*



A. A. Martinez, D. Yan, D. Lockman, D. Brabbins, K. Kota, M. Sharpe, D. A. Jaffray, F. Vicini, and J. Wong, "Improvement in dose escalation using the process of adaptive radiotherapy combined with three-dimensional conformal or intensity-modulated beams for prostate cancer," *Int J Radiat Oncol Biol Phys* **50** (5), 1226-34 (2001).

*p: 4*

B. M. McCurdy, K. Luchka, and S. Pistorius, "Dosimetric investigation and portal dose image prediction using an amorphous silicon electronic portal imaging device," *Med Phys* **28** (6), 911-24 (2001).

*p: 29*

L. N. McDermott, R. J. Louwe, J. J. Sonke, M. B. van Herk, and B. J. Mijnheer, "Dose-response and ghosting effects of an amorphous silicon electronic portal imaging device," *Med Phys* **31** (2), 285-95 (2004).

*p: 131*

T. R. McNutt, T. R. Mackie, P. Reckwerdt, and B. R. Paliwal, "Modeling dose distributions from portal dose images using the convolution/superposition method," *Med Phys* **23** (8), 1381-92 (1996).

*p: 6*

G. V. Menon and R. S. Sloboda, "Compensator quality control with an amorphous silicon EPID," *Med Phys* **30** (7), 1816-24 (2003).

*p: 14*

C. Moisan, F. Cayouet, and G. McDonald, *DETECT2000 A Program for Modeling Optical Properties of Scintillators* (Dept. of Electrical and Computer Engineering, Laval University, Quebec City, QC, 2000).

*p: 32*

G.-Z. Moliere, "Theorie der Streuung schneller geladener Teilchen. I. Einzelstreuung am abgeschirmten Coulomb-Feld," *Z. Naturforsch* **2a**, 133-145 (1947).

*p: 54*

T. T. Monajemi, S. Steciw, B. G. Fallone, and S. Rathee, "Modeling scintillator-photodiodes as detectors for megavoltage CT," *Med Phys* **31** (5), 1225-34 (2004).

*p: 62*

P. Munro, "Portal Imaging Technology: Past, Present, and Future," *Semin Radiat Oncol* **5** (2), 115-133 (1995).

*p: 7*

P. Munro and D. C. Bouius, "X-ray quantum limited portal imaging using amorphous silicon flat-panel arrays," *Med Phys* **25** (5), 689-702 (1998).

*p: 85*

M. Partridge, B.A. Groh, L. Spies, B. M. Hesse, and T. Bortfeld, "A study of the spectral response of portal imaging detectors," presented at the Proceedings of the IEEE Nuclear Science Symposium, 2000 (unpublished).

*p: 131*

PlasticsUSA, "Specific Gravity of Major Polymers," (Eastpoint-Oltean, <http://www.plasticsusa.com/specgrav2.html>, 2003).

*p: 31*

I. Rabinowitz, J. Broomberg, M. Goitein, K. McCarthy, and J. Leong, "Accuracy of radiation field alignment in clinical practice," *Int J Radiat Oncol Biol Phys* **11** (10), 1857-67 (1985).

*p: 4*

T. Radcliffe, G. Barnea, B. Wowk, R. Rajapakshe, and S. Shalev, "Monte Carlo optimization of metal/phosphor screens at megavoltage energies," *Med Phys* **20** (4), 1161-9 (1993).

*p: 78*

R. Rajapakshe, K. Luchka, and S. Shalev, "A quality control test for electronic portal imaging devices," *Med Phys* **23** (7), 1237-44 (1996).

*p: 141*

S. Rathee, B. A. McClean, and C. Field, "An improved method for rebinning kernels from cylindrical to Cartesian coordinates," *Med Phys* **20** (5), 1343-51 (1993).

*p: 82*

D. W. O. Rogers, I. Kawrakow, J.P. Seuntjens, and B.R.B. Walters, NRC User Codes for EGSnrc Report No. PIRS-702(revA), 2002.

*p: 48*

J. A. Rowlands and J. Yorkston, "Flat Panel Detectors for Digital Radiography," in *Handbook of Medical Imaging* (SPIE Press, Bellingham WA, 2000), pp. 223 - 328.

*p: 7*

R. Y. Rubinstein, *Simulation and the Monte Carlo Method*, 1 ed. (Wiley-Interscience, Hoboken, NJ, 1981).

*p: 11*

A. E. Schach von Wittenau, C. M. Logan, M. B. Aufderheide, 3rd, and D. M. Slone, "Blurring artifacts in megavoltage radiography with a flat-panel imaging system:

comparison of Monte Carlo simulations with measurements,” *Med Phys* **29** (11), 2559-70 (2002).

*p: 29*

E. Schule and C Pychlau, *Diamond Detector Type 60003 Instruction Manual* (PTW-Freiburg, Freiburg, 1998).

*p: 88*

S. Shalev, *PIPSpro User's Guide Version 3.2* (Masthead Imaging Corporation, Nanaimo, BC, 1999).

*p: 141*

D. Sheikh-Bagheri and D. W. Rogers, “Monte Carlo calculation of nine megavoltage photon beam spectra using the BEAM code,” *Med Phys* **29** (3), 391-402 (2002).

*p: 79*

J. V. Siebers, J. O. Kim, L. Ko, P. J. Keall, and R. Mohan, “Monte Carlo computation of dosimetric amorphous silicon electronic portal images,” *Med Phys* **31** (7), 2135-46 (2004).

*p: 6*

P. Stavrev, D. Hristov, B. Warkentin, E. Sham, N. Stavreva, and B. G. Fallone, “Inverse treatment planning by physically constrained minimization of a biological objective function,” *Med Phys* **30** (11), 2948-58 (2003).

*p: 4*

S. Steciw, B. Warkentin, S. Rathee, and B. G. Fallone, “Three-dimensional IMRT verification with a flat-panel EPID,” *Med Phys* **32** (2), 600-12 (2005).

*p: 177*

D. J. Steklenski (personal communication from Health Imaging, Eastman Kodak).

*p: 32*

R. D. Stewart, W. E. Wilson, J. C. McDonald, and D. J. Strom, “Microdosimetric properties of ionizing electrons in water: a test of the PENELoPE code system,” *Phys Med Biol* **47**, 79-88 (2002).

*p: 52*

A. M. Syme, C. Kirkby, T. A. Riauka, B. G. Fallone, and S. A. McQuarrie, “Monte Carlo investigation of single cell beta dosimetry for intraperitoneal radionuclide therapy,” *Phys Med Biol* **49** (10), 1959-72 (2004).

*p: 15*

Varian Medical Systems, *Portal Vision aS500 Rel.6 Reference Manual* (Varian Medical Systems Inc., Palo Alto, CA, 2000).

*p: 23*

R. C. Taylor, V. M. Tello, C. B. Schroy, M. Vossler, and W. F. Hanson, "A generic off-axis energy correction for linac photon beam dosimetry," *Med Phys* **25** (5), 662-7 (1998).

*p: 98*

C. L. Thomason, "Implementation and clinical use of portal imaging," *Cancer Treat Res* **93**, 69-99 (1998).

*p: 5*

G. Tsang, C. Moisan, and J. G. Rogers, "A simulation to model position encoding multicrystal PET detectors," *IEEE Trans. Nucl. Sci.* **42** (6), 2236-2243 (1995).

*p: 62*

N. Tyagi, A. Bose, and I. J. Chetty, "Implementation of the DPM Monte Carlo code on a parallel architecture for treatment planning applications," *Med Phys* **31** (9), 2721-5 (2004).

*p: 177*

W. van der Zee, A. Hogenbirk, and S. C. van der Marck, "ORANGE: a Monte Carlo dose engine for radiotherapy," *Phys Med Biol* **50** (4), 625-41 (2005).

*p: 177*

J. Van Dyk, "Quality Assurance," in *Treatment Planning in Radiation Oncology*, edited by F.M. and Potish Khan, R.A. (Williams & Wilkins, Baltimore, MA, 1998), pp. 131.

*p: 4*

M. van Herk and H. Meertens, "A matrix ionisation chamber imaging device for on-line patient setup verification during radiotherapy," *Radiother Oncol* **11** (4), 369-78 (1988).

*p: 8*

B.R.B. Walters, J. Treurniet, D. W. O. Rogers, and I. Kawrakow, QA tests of the EGSnrc system and comparison with EGS4 (Draft) Report No. PIRS-703, 2003.

*p: 48*

B. Warkentin, "Development of Verification Procedures using a Flat-Panel EPID, and Application and Investigation of Radiobiological Models, for Intensity-Modulated Radiotherapy," Ph.D. Thesis, University of Alberta, 2005.

*p: 4*

B. Warkentin, S. Steciw, S. Rathee, and B. G. Fallone, "Dosimetric IMRT verification with a flat-panel EPID," *Med Phys* **30** (12), 3143-55 (2003).

*p: 4*

J. W. Wong and J. A. Purdy, "On methods of inhomogeneity corrections for photon transport," *Med Phys* 17 (5), 807-14 (1990).

*p: 4*

C. Yeboah and S. Pistorius, "Monte Carlo studies of the exit photon spectra and dose to a metal/phosphor portal imaging screen," *Med Phys* 27 (2), 330-9 (2000).

*p: 131*

T. Yu, J. M. Sabol, J. A. Seibert, and J. M. Boone, "Scintillating fiber optic screens: a comparison of MTF, light conversion efficiency, and emission angle with Gd<sub>2</sub>O<sub>2</sub>S:Tb screens," *Med Phys* 24 (2), 279-85 (1997).

*p: 80*

J. R. Zullo, C. Bloch, P. C. Chi, and R. Kudchadker, "Linearity and uniformity response as an indicator of performance for Agfa ADC-MD10 computed radiography plates," *Med Dosim* 29 (2), 118-21 (2004).

*p: 177*